

**SÃO PAULO STATE UNIVERSITY - JÚLIO DE MESQUITA FILHO - UNESP**  
**School of Science - Campus of Bauru**

**JOÃO PAULO CACHANESKI LOPES**

**ELECTRONIC STRUCTURE OF COMPOUNDS OF NATURAL ORIGIN AND  
THEIR DERIVATIVES FOR APPLICATION IN ORGANIC ELECTRONICS**



BAURU/SP - Brazil  
PAU/Nouvelle-Aquitaine - France  
2025

**JOÃO PAULO CACHANESKI LOPES**

**ELECTRONIC STRUCTURE OF COMPOUNDS OF NATURAL ORIGIN AND  
THEIR DERIVATIVES FOR APPLICATION IN ORGANIC ELECTRONICS**

Thesis presented, under cotutelle agreement to São Paulo State University (UNESP), School of Science, Bauru and to Université de Pau et des Pays de l'Adour (UPPA), in partial fulfillment of the requirements for the degree of Doctor in Materials Science and Technology (UNESP) and in Chimie Théorique (UPPA).

Concentration area: Modeling and Simulation of Materials

Advisor: Prof. Dr. Augusto Batagin Neto (UNESP)

Advisor: Prof. Dr. Didier Bégué (UPPA)

BAURU/SP - Brazil

PAU/Nouvelle-Aquitaine - France

2025

Cachaneski-Lopes, João Paulo.

Electronic structure of compounds of natural origin and their derivatives for application in organic electronics / João Paulo Cachaneski Lopes. - Bauru, 2025

132 f. : il.

Orientador: Augusto Batagin-Neto

Orientador: Didier Bégué

Tese (Doutorado) - Universidade Estadual Paulista (Unesp), Faculdade de Ciências, Bauru e Université de Pau et des Pays de l'Adour (UPPA), École de Doctorale Sciences Exactes & Leurs Applications

1. Electronic structure. 2. Melanin. 3. Chemical sensors 4. Photovoltaic energy systems. 5. Density functional theory. I. Universidade Estadual Paulista. Faculdade de Ciências. II. Université de Pau et des Pays de l'Adour. III. Título.

ATA DA DEFESA PÚBLICA DA TESE DE DOUTORADO DE JOÃO PAULO CACHANESKI LOPES, DISCENTE DO PROGRAMA DE PÓS-GRADUAÇÃO EM CIÊNCIA E TECNOLOGIA DE MATERIAIS, DA FACULDADE DE CIÊNCIAS - CÂMPUS DE BAURU.

Aos 29 de outubro de 2025, às 9h30min, por meio de Videoconferência, realizou-se a defesa de TESE DE DOUTORADO de JOÃO PAULO CACHANESKI LOPES, intitulada **ELECTRONIC STRUCTURE OF COMPOUNDS OF NATURAL ORIGIN AND THEIR DERIVATIVES FOR APPLICATION IN ORGANIC ELECTRONICS**. A Comissão Examinadora foi constituída pelos seguintes membros: Prof. Dr. AUGUSTO BATAGIN NETO (Orientador(a) - Participação Presencial) do(a) Departamento de Ciências e Tecnologia / Instituto de Ciências e Engenharia - Unesp/Câmpus de Itapeva , Profa. Dra. CHRISTINE LARTIGAU-DAGRON (Participação Virtual) do(a) Institut des Sciences Analytiques et de Physico-Chimie pour l'Environnement et les Matériaux (Institut - IPREM) / Université de Pau et des Pays de l'Adour - UPPA/França, Profa. Dra. PAULA HOMEM DE MELLO (Participação Virtual) do(a) Centro de Ciência Naturais e Humanas / Universidade Federal do ABC, Profa. Dra. CLARISSA DE ALMEIDA OLIVATI (Participação Virtual) do(a) Departamento de Física / Faculdade de Ciência e Tecnologia - Unesp/Câmpus de Presidente Prudente, Prof<sup>a</sup>. Dr<sup>a</sup>. MARYSTELA FERREIRA (Participação Virtual) do(a) Departamento de Físico-Química / Universidade Federal de São Carlos (UFSCar) - Sorocaba, Após a exposição pelo doutorando e arguição pelos membros da Comissão Examinadora que participaram do ato, de forma presencial e/ou virtual, o discente recebeu o conceito final: \_\_\_ APROVADO \_\_\_. Nada mais havendo, foi lavrada a presente ata, que após lida e aprovada, foi assinada pelo(a) Presidente(a) da Comissão Examinadora.

Prof. Dr. AUGUSTO BATAGIN NETO



## **Agradecimentos**

À Universidade Estadual Paulista (UNESP) e à Université de Pau et des Pays de l'Adour (UPPA), pela oportunidade de realização deste doutorado em cotutela. Aos meus orientadores, Prof. Dr. Augusto Batagin Neto e Prof. Dr. Didier Bégué, pelo apoio contínuo, pelas orientações criteriosas e pela confiança ao longo deste trabalho. Suas contribuições acadêmicas e humanas foram fundamentais para o desenvolvimento desta pesquisa e para a minha formação como pesquisador.

À Coordenação de Aperfeiçoamento de Pessoal de Nível Superior (CAPES) (processos nº 88887.817519/2023-00 CAPES-Proex e 88887.802762/2023-00 CAPES-PrInt) e ao Conselho Nacional de Desenvolvimento Científico e Tecnológico (CNPq), pelo suporte financeiro que viabilizou este estudo. Ao Centre de Calcul Intensif (GENCI-IDRIS) (financiamento nº 2022-102485) e ao Centro de Computação Científica da UNESP (GridUNESP), pelas estruturas computacionais essenciais para a execução deste trabalho.

Aos colegas do Grupo de Teoria e Modelagem Molecular (UNESP) e do Institut des Sciences Analytiques et de Physico-Chimie pour l'Environnement et les Matériaux (IPREM), pelo ambiente de trabalho colaborativo, pelas discussões técnicas e pela amizade construída ao longo da jornada.

À minha família, por todo o amor, apoio e incentivo incondicional, mesmo à distância. A aqueles que, de diferentes formas, contribuíram com palavras, ideias, parcerias ou simplesmente com a presença nos momentos certos, deixo aqui meu sincero agradecimento.

## Acknowledgments

I would like to express my sincere gratitude to São Paulo State University (UNESP) and Université de Pau et des Pays de l'Adour (UPPA) for the opportunity to undertake this cotutelle doctoral program. I am especially thankful to my advisors, Prof. Dr. Augusto Batagin Neto and Prof. Dr. Didier Bégué, for their continuous support, rigorous guidance, and trust throughout the development of this work. Their academic insight and human perspective have been essential to my growth as a researcher.

I gratefully acknowledge the financial support provided by the Coordination for the Improvement of Higher Education Personnel (CAPES) (grants 88887.817519/2023-00 CAPES-Proex and 88887.802762/2023-00 CAPES-PrInt) and the National Council for Scientific and Technological Development (CNPq), which made this study possible. I also thank the Centre for Scientific Computing at UNESP (GridUNESP) and the Grand Equipement National de Calcul Intensif (GENCI-IDRIS) (grant 2022-102485) for providing the computational resources necessary for this research.

I extend my thanks to my colleagues from the Molecular Theory and Modeling Group (UNESP) and from the Institut des Sciences Analytiques et de Physico-Chimie pour l'Environnement et les Matériaux (IPREM) for the collaborative working environment, valuable discussions, and friendships built along this journey.

Finally, I express my deepest appreciation to my family, for their unwavering love, support, and encouragement, even from afar. To all those who, in different ways, contributed with their words, ideas, or simply by being present at the right moments, I offer my heartfelt thanks.

## Remerciements

Je tiens à exprimer ma profonde gratitude à l'Université d'État de São Paulo (UNESP) et à l'Université de Pau et des Pays de l'Adour (UPPA) pour m'avoir offert l'opportunité de réaliser ce doctorat en cotutelle. Mes remerciements les plus sincères vont à mes directeurs de thèse, le Prof. Dr. Augusto Batagin Neto et le Prof. Dr. Didier Bégué, pour leur accompagnement constant, leurs conseils rigoureux et leur confiance tout au long de ce travail. Leurs contributions, tant scientifiques qu'humaines, ont été essentielles à ma formation en tant que chercheur.

Je remercie la Coordenação de Aperfeiçoamento de Pessoal de Nível Superior (CAPES) pour le soutien financier accordé à travers les projets CAPES-Proex (bourse n° 88887.817519/2023-00) et CAPES-PrInt (n° 88887.802762/2023-00), ainsi que le Conselho Nacional de Desenvolvimento Científico e Tecnológico (CNPq). Ma reconnaissance va également au Centre de Calcul Intensif (GENCI-IDRIS) (subvention 2022-102485) et au Centre de Calcul Scientifique de l'UNESP (GridUNESP) pour les ressources informatiques indispensables à la réalisation de cette étude.

Je souhaite remercier mes collègues du Groupe de Théorie et Modélisation Moléculaire (UNESP) et de l'Institut des Sciences Analytiques et de Physico-Chimie pour l'Environnement et les Matériaux (IPREM) pour l'environnement de travail collaboratif, les échanges scientifiques enrichissants et les liens d'amitié tissés au fil de cette aventure.

Enfin, j'adresse mes remerciements les plus chaleureux à ma famille pour leur amour inconditionnel, leur soutien et leurs encouragements constants, même à distance. À toutes celles et ceux qui, d'une manière ou d'une autre, ont contribué par leurs paroles, leurs idées ou leur simple présence au bon moment, je dis merci du fond du cœur.

*Life is like riding a bicycle.  
In order to keep your balance, you must keep moving.*  
— Albert Einstein

## RESUMO

A incorporação de compostos naturais em materiais está atraindo cada vez mais interesse na química devido aos seus benefícios práticos e econômicos. Embora estudos anteriores tenham destacado a estabilidade e as propriedades optoeletrônicas desses materiais, ainda faltam informações detalhadas sobre suas interações em nível molecular e seus mecanismos funcionais. Nesta tese, o foco foi a investigação de compostos bioinspirados à base de melanina para aplicação em sensores químicos e células solares fotovoltaicas, por meio de cálculos de estrutura eletrônica baseados na Teoria do Funcional da Densidade (DFT). Dois tópicos principais foram explorados: (i) a viabilidade de compostos à base de vanilina para detecção de nitroaromáticos (NACs) e (ii) a proposição/avaliação de desempenho de compostos inspirados na melanina como aceitadores/doadores em células solares orgânicas de heterojunção em volume. O primeiro tópico aborda a interação entre sistemas à base de melanina e NACs, examinando propriedades eletrônicas, ópticas, estruturais e de estabilidade. Os resultados revelam que derivados de melanina apresentam alta sensibilidade a esses analitos, possibilitando detecção química seletiva, reversível, de baixo custo e ambientalmente amigável. Em relação ao segundo tópico, foi proposta e investigada uma série de moléculas doadoras e aceitadoras baseadas em derivados de Y6 e inspirados na eumelanina. Nossos resultados mostram que grupos terminais baseados em melanina podem conferir propriedades ópticas e eletrônicas únicas, viabilizando materiais aceitadores de alto desempenho, enquanto oligômeros semelhantes à eumelanina surgem como promissores candidatos a doadores. Esses achados evidenciam como modificações químicas bioinspiradas podem aumentar tanto a eficiência quanto a sustentabilidade da próxima geração de eletrônicos orgânicos.

**Palavras-chave:** compostos baseados em melanina; detecção de nitroaromáticos; células solares orgânicas; teoria do funcional da densidade; materiais sustentáveis.

## ABSTRACT

The incorporation of natural compounds into materials is attracting increasing interest in chemistry due to their practical and economic benefits. Although previous studies have highlighted the stability and optoelectronic properties of these materials, detailed insights into their molecular-level interactions and functional mechanisms are still lacking. In this thesis our focus was the investigation of bioinspired melanin-based compounds for application in chemical sensors and photovoltaics via density functional theory (DFT)-based electronic structure calculations. Two main topics have been investigated: i) the feasibility of vanillin-based compounds for nitroaromatics (NACs) detection and ii) proposition/performance evaluation of melanin-inspired compounds as acceptors/donors in bulk heterojunction organic solar cells. The first topic explores the interaction between melanin-based systems and NACs by examining electronic, optical, structural, and stability properties. The results reveal that melanin derivatives exhibit high sensitivity to these analytes, enabling selective, reversible, cost-effective, and environmentally friendly chemical detection. In relation to the second topic, a series of donor and acceptor molecules based on Y6 derivatives and eumelanin-inspired motifs was proposed and investigated. Our results show that melanin-based end groups can impart unique optical and electronic properties, enabling high-performance acceptor materials, while eumelanin-like oligomers emerge as promising donor candidates. These findings highlight how bio-inspired chemical modifications can enhance both the efficiency and sustainability of next-generation organic electronics.

**Keywords:** melanin-based compounds; nitroaromatic detection; organic solar cells; density functional theory; sustainable materials.

## RÉSUMÉ

L'intégration de composés naturels dans les matériaux suscite un intérêt grandissant en chimie, en raison de leurs atouts tant pratiques qu'économiques. Bien que des études antérieures aient mis en évidence la stabilité et les propriétés optoélectroniques de ces matériaux, des informations détaillées sur leurs interactions à l'échelle moléculaire et leurs mécanismes fonctionnels font encore défaut. Dans cette thèse, l'objectif a été d'étudier des composés bio-inspirés à base de mélanine pour une application dans les capteurs chimiques et les cellules solaires organiques, à travers des calculs de structure électronique basés sur la théorie de la fonctionnelle de la densité (DFT). Deux axes principaux ont été explorés : i) la faisabilité de composés à base de vanilline pour la détection des nitroaromatiques (NAC) et ii) la proposition/évaluation des performances de composés inspirés de la mélanine en tant qu'accepteurs/donneurs dans des cellules solaires organiques à hétérojonction en volume. Le premier axe étudie l'interaction entre des systèmes à base de mélanine et des NACs, en examinant leurs propriétés électroniques, optiques, structurelles et de stabilité. Les résultats montrent que les dérivés de la mélanine présentent une sensibilité élevée à ces analytes, permettant une détection chimique sélective, réversible, peu coûteuse et respectueuse de l'environnement. Concernant le second axe, une série de molécules donneuses et accepteurs basées sur des dérivés du Y6 et des motifs inspirés de l'eumélanine a été proposée et étudiée. Nos résultats indiquent que des groupes terminaux dérivés de la mélanine peuvent conférer des propriétés optiques et électroniques uniques, permettant la conception de matériaux accepteurs performants, tandis que des oligomères de type eumélanine apparaissent comme des donneurs prometteurs. Ces résultats soulignent comment des modifications chimiques bio-inspirées peuvent améliorer à la fois l'efficacité et la durabilité de la prochaine génération d'électroniques organiques.

**Mots-clés** : composés à base de mélanine, détection de nitroaromatiques, cellules solaires organiques, théorie de la fonctionnelle de densité, matériaux durables

## TABLE OF CONTENTS

CHAPTER I – General Motivation.....	17
1.1 Introduction.....	17
CHAPTER II – Melanin-Based Compounds as Low-Cost Sensors for Nitroaromatics: Theoretical Insights on Molecular Interactions and Opto-Electronic Responses.....	19
2.1 Abstract.....	19
2.2 Introduction.....	20
2.3 Material and methods.....	23
2.3.1 Materials.....	23
2.3.2 Methodology.....	24
2.4 Results and discussion.....	27
2.4.1 Isolated structures.....	27
2.4.2 Adsorbed structures.....	32
2.4.3 Born-Oppenheimer molecular dynamics.....	41
2.5 Conclusions.....	43
APPENDIX A – Melanin-Based Compounds as Low-Cost Sensors for Nitroaromatics: Theoretical Insights on Molecular Interactions and Opto-Electronic Responses.....	45
A1. Total density of states (DOS) of compounds 9a, 9b and NACs.....	45
A2. Adsorption methodologies.....	46
A3. Additional data for adsorbed systems (clusters obtained via CAFI).....	47
A4. Results for clusters obtained via docking by aISS.....	54
CHAPTER III – DFT-Guided Design of Melanin-Inspired Materials for High-Performance Organic Solar Cells.....	61
3.1 Abstract.....	61
3.2 Introduction.....	62
3.3 Material and Methods.....	64
3.3.1 Material.....	64
3.3.2 Methods.....	65
3.4 Results and discussions.....	67
3.4.1 Evaluation of EG <sub>mel</sub> : from DHICA to EG <sub>mel</sub> -(OH) <sub>2</sub> and other intermediates.....	67
3.4.2 Comparison between EG <sub>mel</sub> -R and EG-R: influence of side groups attached on phenyl rings.....	71
3.4.3 Incorporation of EG <sub>mel</sub> -R <sub>n</sub> and EG-R <sub>n</sub> groups on Y6 <sub>core</sub> .....	73
3.4.4 Evaluation of melanin-inspired oligomeric structures: MIO <sub>9a</sub> and MIO <sub>9b</sub> .....	80
3.4.5 Estimation of performance parameters.....	81
3.5 Conclusions.....	92

APPENDIX B – DFT-Guided Design of Melanin-Inspired Materials for High-Performance Organic Solar Cells.....	94
B1. Theoretical parameters relevant to the BHJOSCs performance.....	94
B2. Opto-electronic properties of oligomeric donor systems and traditional fullerene-based acceptors.....	96
B3. Theoretical optical absorption spectra of typical donors, acceptors and Y6 clusters...	97
B4. Spatial overlap and distribution of Kohn-Sham frontier molecular orbitals.....	101
B5. Condensed to atom Fukui indexes and MEP: extended MIOs.....	108
B6. Donation-acceptance indexes.....	110
B7. Organic solar cell's efficiency parameters.....	112
B8. Reorganization energy.....	115
B9. Sun absorption yield.....	116
CHAPTER IV – General Conclusions.....	119
REFERENCES.....	120
CURRICULUM DATA.....	132

## ***Organization of the Thesis***

This thesis is structured into four main chapters, in addition to introductory and concluding sections.

### **I. General Motivation**

The first chapter presents a general motivation, providing a broad overview of the rationale for exploring melanin-inspired compounds as sustainable alternatives for organic electronics, specifically targeting applications in chemical sensors and solar cells through computational analysis.

### **II. Melanin-Based Compounds as Low-Cost Sensors for Nitroaromatics: Theoretical Insights on Molecular Interactions and Optoelectronic Responses**

This study is motivated by the environmental and health hazards posed by nitroaromatic compounds (NACs), which are prevalent in industrial pollutants and explosives. The research aims to develop a chemical sensor based on melanin-inspired compounds that may offer a low-cost and sensitive solution for identifying these toxic pollutants. Utilizing density functional theory (DFT)-based calculations, the study examines the electronic and optical properties of melanin-inspired compounds to assess their interactions with specific NACs, such as trinitrotoluene (TNT) and trinitrophenol (TNP). The methodological approach focuses on simulating and analyzing how molecular properties are modulated by the presence of NACs, aiming to identify indicators of successful detection.

### **III. DFT-Guided Design of Melanin-Inspired Materials for High-Performance Organic Solar Cells**

This chapter addresses the advancement of both environmental sustainability and efficiency in organic solar cells (OSCs), which have historically relied on fullerene-based acceptors that are often costly and limited in performance. Drawing inspiration from the multifunctional properties of melanin, the study investigates synthetic eumelanin-based Y6 derivatives as potential non-fullerene acceptors (NFAs), as well as melanin-inspired oligomers (MIOs) as donor materials. Density functional theory (DFT) calculations are employed to model these systems, with a particular focus on halogen and hydroxyl substitutions introduced in the NFAs to assess how these groups influence their electronic, optical, and structural

properties. The research further explores how the different melanin-based structures interact at the molecular level with Y6 acceptors, aiming to enhance charge transfer processes and improve stability in OSC applications.

#### **IV. General Conclusions**

This final chapter consolidates the findings, validating the potential of melanin-inspired compounds as sustainable materials for organic electronics. The results demonstrate their effectiveness in both environmental monitoring and renewable energy applications. For chemical sensing, these materials exhibit strong charge-transfer characteristics suitable for detecting toxic NACs. In solar energy, their tunable electronic properties support their use as efficient NFAs in OSCs. Altogether, the study provides a computational foundation for the development of bio-inspired materials aligned with the principles of green chemistry and technological sustainability.

## CHAPTER I – General Motivation

### 1.1 Introduction

The development of new materials for organic electronics has gained considerable attention in recent years, especially for applications that require materials with specific optoelectronic properties, environmental compatibility, and ease of synthesis <sup>1,2</sup>. In this context, compounds of natural origin, particularly those inspired by melanin, offer promising alternatives to traditional organic semiconductors <sup>3</sup>.

Melanin and its synthetic analogs are widely studied due to their robust chemical structure, chemical stability, and unique ability to facilitate ionic and electronic transport. Such properties establish melanin-based compounds as potential candidates for eco-friendly applications in chemical sensors and organic photovoltaic cells <sup>4</sup>. Such applications are specifically explored in this thesis via electronic structure calculations. Specifically two main topics were addressed: i) the feasibility of melanin inspired systems for nitroaromatic (NAC) detection, and ii) design and evaluation of melanin-inspired acceptors and donors in bulk heterojunction organic solar cells.

Melanins exhibit a remarkable potential for sensor applications <sup>3,5,6</sup> owing to their adsorption centers, intrinsic charge-transport properties, and high sensitivity to variations in the chemical environment. Despite these features, the use of melanin derivatives in chemical sensing remains limited, largely due to the intrinsic structural complexity of natural compounds, which hinders experimental reproducibility. These challenges, however, have also stimulated the development of diverse synthetic melanin-like compounds tailored for a wide range of applications, leading to new compounds with varied properties.

In this context, in 2015 Selvaraju and collaborators have proposed a set of synthetic eumelanin-inspired oligomers for optoelectronic applications <sup>7</sup>. These molecules, derived from renewable vanillin through efficient synthetic routes, combine structural features that are highly advantageous for organic electronic applications. It includes  $\pi$ -conjugated alkynyl units that promote planarity, enhance charge-carrier mobility, and facilitate frontier orbital delocalization. The presence of electron-donating methoxy groups further tunes their optoelectronic response by increasing electron density and preserving molecular geometry. Such a combination of attributes not only supports efficient charge separation and transport but also suggests a strong potential for interaction with analytes in sensing applications.

Nevertheless, despite these favorable characteristics, the exploration of such materials as chemical sensors remains virtually absent from the literature, representing a significant and promising avenue for investigation.

Within this framework, here we propose and assess the potential of melanin-based structures for nitroaromatics detection. Nitroaromatic compounds (NACs) are commonly employed in industrial processes but present environmental and health risks due to their persistence and toxicity<sup>8-10</sup>. Existing NAC sensors are effective but often costly and complex to produce, evidencing the need for the development and search for new simpler and sustainable devices, which motivated the present theoretical study. The obtained results show that melanin-inspired compounds can act as NAC detectors with good sensitivity and stability, opening avenues for using sustainable and bio-inspired materials in organic electronics.

Regarding the second topic, this thesis focuses on the design and performance evaluation of chemically modified non-fullerene acceptors (NFAs) for OSC applications. Historically, the spherical geometry of fullerenes limited donor/acceptor interfacial contact, constraining charge transfer efficiency. In contrast, non-fullerene acceptors such as Y6 exhibit more planarized structures, improving interfacial area and optical absorption. While NFAs have significantly enhanced power conversion efficiency, they remain limited by restricted light absorption and incomplete exciton dissociation<sup>11,12</sup>.

Previous studies conducted in our group have shown that the electron-transfer properties of Y6 are strongly influenced by its end groups (EGs)<sup>13</sup>. In particular, chemical modifications involving the substitution of fluorine atoms in conventional EGs with other halogens have been explored as strategies to optimize Y6 performance<sup>14</sup>. Beyond their bio-friendly appeal, melanin-inspired motifs offer additional advantages, including ionic transport capabilities and the presence of anchoring sites, while their structural similarity to Y6 EGs suggests a natural chemical compatibility. In this work, we therefore propose and evaluate new Y6 derivatives incorporating melanin-based end groups (EG<sub>mel</sub>). These melanin-inspired NFAs demonstrate promising structural and electronic properties for OSC applications, although further research remains necessary to fully maximize their performance. Beyond their specific applicability, the exploration of such bio-inspired systems also reflects a broader trend in materials science: the pursuit of organic semiconductors that combine efficiency with environmental sustainability. The growing demand for environmentally sustainable materials has driven much of the recent research on organic systems for technological applications<sup>15,16</sup>. Within this context, the search for compounds that combine favorable optoelectronic properties, chemical stability, biocompatibility, and a

reduced environmental footprint has emerged as a key priority. Many of these attributes are naturally found in bio-derived or bio-inspired compounds<sup>17</sup>.

In this scenario, theoretical approaches can play a decisive role, providing predictive insights that help identify promising structures prior to experimental validation. By describing, rationalizing, and even forecasting the optoelectronic behavior of candidate materials, computational studies offer guidance for experimental efforts and facilitate the interpretation of empirical results. In this sense, the present thesis not only addresses fundamental questions regarding the interaction of melanin-inspired systems with hazardous analytes and their potential in energy conversion, but also contributes to the broader pursuit of sustainable materials for next-generation organic electronics.

## CHAPTER II – Melanin-Based Compounds as Low-Cost Sensors for Nitroaromatics: Theoretical Insights on Molecular Interactions and Opto-Electronic Responses<sup>1</sup>

### 2.1 Abstract

Nitroaromatic compounds (NACs) are used in various industrial applications, including dyes, inks, herbicides, pharmaceuticals, and explosives. Due to their toxicity and environmental persistence, reliable detection and monitoring methods are required. Hybrid organic–inorganic structures have shown potential for NAC sensing; however, their complex synthesis, high processing costs, and limited reproducibility hinder practical implementation, highlighting the need for simpler and more accessible materials. In this study, we employed density functional theory (DFT)-based calculations to evaluate the electronic, optical, and reactive properties of two melanin-based polymeric systems aiming to assess their potential use as NAC detectors. Our results indicate the potential of these materials to detect a series of nitroaromatic compounds such as 2,4-DNP, 2,4-DNT, 2,6-DNT, TNP and TNT by electrical and infrared optical measurements. Born-Oppenheimer molecular dynamics (BOMD) simulations reveal the thermal stability of the adsorption process, confirming the effective substrate/analyte interaction under different temperature conditions. To the best of our knowledge, this compound has not been proposed for sensing applications. Its low cost and facile synthesis make it a promising candidate for developing environmentally friendly organic NAC sensors.

**Keywords:** Nitroaromatic sensor, melanin-based compound, density functional theory.

---

<sup>1</sup> Note: Parts of this chapter were previously published as:

Cachaneski-Lopes, J. P.; Hawthorne, F.; Woellner, C. F.; Nelson, T. L.; Hiorns, R. C.; Graeff, C. F. O.; Bégué, D.; Batagin-Neto, A. Melanin-based compound as low-cost sensors for nitroaromatics: Theoretical insights on molecular interactions and optoelectronic responses. *ACS Omega*, Special Issue “Chemistry in Brazil: Advancing through Open Science”, 10, 31908-31920 (2025).

The text has been reorganized and adapted to meet the formatting requirements of this thesis.

## 2.2 Introduction

Nitroaromatic compounds (NACs) are aromatic structures with one or more nitro groups (-NO<sub>2</sub>). The presence of the -NO<sub>2</sub> group make NACs useful as raw materials in the chemical syntheses of a variety of compounds such as corrosion inhibitors, antioxidants, preservatives, fuel additives, dyes, paints, cosmetics, fungicides, herbicides, pesticides, drugs and other industrial chemicals<sup>8,9,18</sup>. NACs are of primary concern as they are mutagenic and carcinogenic<sup>10</sup>, as well as toxic to living organisms<sup>8,9</sup>. Nitro groups make NACs recalcitrant, therefore their degradation is not sustainable and effective, leading to their accumulation in the environment and making NACs a serious threat to the ecological environment and human health<sup>9</sup>.

NACs, such as nitrobenzenes (NB) can cause diseases such as anemia, skin irritation and cancer<sup>19</sup>. NB poisoning in humans causes methemoglobin formation, cyanosis, neurotoxic effects, unconsciousness, gastric irritation, nausea, vomiting, drowsiness, convulsions, coma, respiratory failure and may result in death<sup>20-22</sup>. In addition, NB can be metabolized to *p*-aminophenol and *p*-nitrophenol, being very slowly eliminated by the organism<sup>23</sup>.

The development of materials and devices for detecting NAC is therefore essential. It has seen a resurgence since the 2000s in particular because NACs were used as explosives in some terrorist attacks<sup>24,25</sup> giving rise to several detectors<sup>26-28</sup>. In particular pyridine, diazine and triazine have been studied in detail due to their properties and their use as chemical sensors for chemical analyses<sup>2,29,30</sup>. In recent years other types of sensors have been proposed such as the Mach-Zehnder interferometer waveguide sensor using porous polycarbonate, with fast responses and high sensitivity. Optical sensors have also been proposed via Förster resonance energy transfer (FRET) mechanism<sup>31</sup>, PbS quantum dots<sup>32-34</sup> and hybrid perovskites<sup>35</sup>. Metal-organic complexes, such as MOFs (metal-organic frameworks) and rare-earth metal-based luminescent coordination polymers (LCPs), have also been considered for NACs detection, mainly due to their tunable porosity, optical properties, and analyte affinity<sup>29,36-38</sup>. Although these compounds show promising sensing performance, their practical application is hindered by synthetic complexity and processing challenges. In particular, complex crystal engineering, multistep routes, and occasional reliance on unexpected transformations have been reported for Basudeb et al<sup>103</sup>. While some energetic MOFs require costly components<sup>40</sup>, presenting low hydrothermal and chemical stabilities. Difficulties in relation to regeneration and recycling have also been reported, which further

complicates their practical use<sup>37,41</sup> Although some specific MOFs present scalable and low-cost production, their crystals are inherently brittle in nature and arduous to process for practical applications<sup>40</sup>

Some of the disadvantages identified above could potentially be mitigated by using organic-based materials as sensors. Specifically, melanins have shown promise in various applications, including pH sensors<sup>5,42</sup>, relative humidity sensors<sup>6</sup> solar cells<sup>43,44</sup> and organic light-emitting diodes (OLEDs)<sup>45</sup>. However, the use of such materials for NACs detection remains largely unexplored. The difficulties associated with the structural characteristics of natural melanins and the resulting lack of reproducibility of the experiments have led to the use of synthetic melanin derivatives for the active layer of these devices. Understanding the complex physical and chemical properties of such melanin-based materials has broadened the prospect of their application in devices<sup>46,47</sup>, prompting us to investigate the possibility of their use in sensors.

In particular, Selvaraju *et al.* have proposed a series of molecules with melanin-inspired cores for optoelectronic applications<sup>7,48</sup>. These compounds are synthetically accessible in good yields from renewable precursors (e.g., vanillin), and they exhibit compatibility with standard cross-coupling methodologies. They exhibit high solubility and display photophysical and electrochemical properties suitable for stable integration into optoelectronic devices<sup>44</sup>. In addition to melanin-based core, these derivatives possess electron-rich C≡C bonds that facilitate conjugation and delocalization, while reinforcing molecular rigidity and planarity, that are essential for efficient charge transport in organic materials<sup>49-51</sup>, as well as charge transfer and molecular recognition in sensing platforms<sup>49</sup>. Moreover, these structures are functionalized with electron-donating methoxy (-OCH<sub>3</sub>) groups, which acts as a strong electron donor<sup>52</sup>, increasing the electron density of the aromatic ring and favoring interactions with electron-deficient analytes (such as NACs). Compared to other electron-donating groups (e.g., -OC<sub>2</sub>H<sub>5</sub>), methoxy offers a favorable combination of electronic enhancement and low steric hindrance, helping preserve the planarity and  $\pi$ -conjugation of the backbone, relevant for charge transfer and sensitivity<sup>52</sup>. Previous studies have shown that methoxy substitution can modulate electronic properties (reducing the HOMO-LUMO gap), and enhance optoelectronic performance of conjugated systems<sup>53</sup>, supporting its role in the design of functional sensing materials.

These insights motivate the use of computational modeling to further investigate the sensing potential of such melanin derivatives to guide future experimental efforts toward the development of new compounds with improved performance. Given the limitations of many

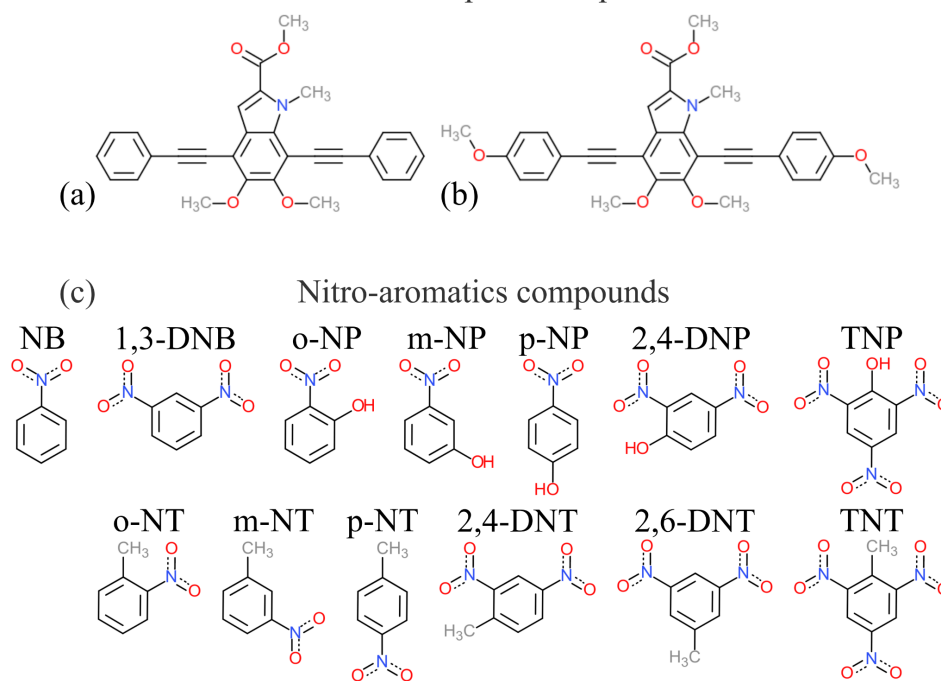
experimental approaches in resolving molecular-level interactions, computational modeling has become a powerful and cost-effective strategy for predicting sensor performance, estimating binding affinities<sup>54</sup>, and guiding the rational design of sensing materials<sup>55</sup>. In this context, theoretical investigations were employed to evaluate the potential of melanin-inspired compounds 9a and 9b, reported by Selvaraju *et al.*<sup>7</sup>, as NAC detectors. Electronic structure calculations and molecular dynamics were performed for such monomeric structures, and the effects of a variety of nitroaromatics were evaluated using density functional theory (DFT)-based calculations. The results indicate that melanin-inspired compounds 9a and 9b exhibit strong and thermally stable interactions with nitroaromatics (notably TNT and TNP), inducing measurable electronic and vibrational shifts. These findings position melanin-inspired compounds as promising low-cost materials for NACs sensing.

## 2.3 Material and methods

### 2.3.1 Materials

Figure 2.1 shows the structures that were considered in this study. For simplicity the compound denomination used in ref<sup>7</sup> was kept (9a and 9b, see Figure 2.1a and b). Figure 2.1c shows the NACs that were considered as analytes: nitrobenzene (NB), *o*-nitrophenol (*o*-NP), *m*-nitrophenol (*m*-NP), *p*-nitrophenol (*p*-NP), *o*-nitrotoluene (*o*-NT), *m*-nitrotoluene (*m*-NT), *p*-nitrotoluene (*p*-NT), 1,3-dinitrobenzene (1,3-DNB), 2,4-dinitrophenol (2,4-DNP), 2,4-dinitrotoluene (2,4-DNT), 2,6-dinitrotoluene (2,6-DNT), trinitrophenol (TNP), and trinitrotoluene (TNT).

**Figure 2.1** - Chemical structures of melanin-inspired compounds 9a (a) and 9b (b) (substrates). Chemical structures of NACs (c) (analytes).  
Eumelanin-inspired compounds



Source: Author.

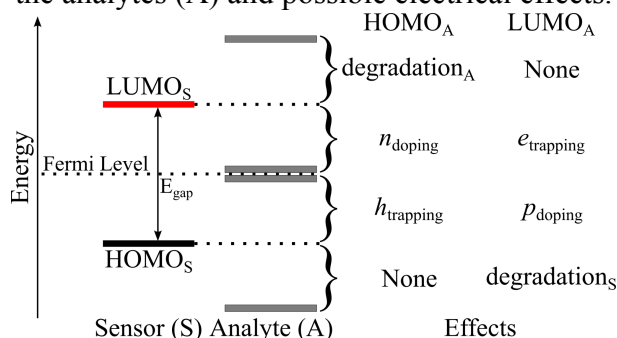
### 2.3.2 Methodology

The structures were designed with the aid of the Gaussview computational package<sup>56</sup>. Conformational searches were conducted via molecular dynamics (MD) simulations at high temperatures (Amber Potential at 1000 K of temperature with the aid of Gabedit software<sup>57</sup>) the lowest energy conformer (coming from MD) was fully optimized in the framework of the density functional theory (DFT) using B3LYP<sup>58,59</sup> exchange-correlation (XC) functional and 6-311G(d,p) basis set on all the atoms.

The local reactivities were evaluated via the condensed-to-atoms Fukui indexes (CAFIs)<sup>60,61</sup>, molecular electrostatic potentials (MEPs)<sup>62</sup> and the spatial distribution of the frontier molecular orbitals (FMOs, i.e. the highest occupied and the lowest unoccupied molecular orbitals, HOMO and LUMO, respectively).

The relative alignments between the FMOs energy of the melanin-based oligomers and the NACs were evaluated to assess the applicability of these systems as chemical sensors, taking into account the possible effects of the analytes on the substrate. Figure 2.2 illustrates some possible effects of analytes (A) on the sensor (S) electrical response expected for distinct FMOs relative alignments. Red and black lines represent the FMOs of the sensor, and gray ones are those of the analyte (S and A subtitles are used for simplicity, respectively). The diagram shows the possible effects according to  $\text{HOMO}_A$  and  $\text{LUMO}_A$  relative positions: (i) material degradation due to charge transfer processes for  $\text{HOMO}_A > \text{LUMO}_S$  and  $\text{LUMO}_A < \text{HOMO}_S$  (analyte and sensor degradation, respectively); (ii) Non-appreciable electric responses are expected for the configurations where  $\text{LUMO}_A > \text{LUMO}_S$  and  $\text{HOMO}_A < \text{HOMO}_S$ , once occupied and unoccupied levels of the A are inserted, respectively, in the valence and conduction bands of S; (iii) electrochemical doping and charge trapping are expected when the FMOs of A are inserted into the band gap of S, depending on their relative positions in relation to the Fermi level of S ( $\text{FL}_S$ ), e.g., n-doping is expected when  $\text{FL} < \text{HOMO}_A < \text{LUMO}_S$  while hole trapping ( $h_{\text{trapping}}$ ) effects are expected when  $\text{HOMO}_S < \text{HOMO}_A < \text{FL}_S$ ; similarly, we have p-doping for  $\text{HOMO}_S < \text{LUMO}_A < \text{FL}_S$  and electron trapping ( $e_{\text{trapping}}$ ) for  $\text{FL}_S < \text{LUMO}_A < \text{LUMO}_S$ <sup>55,63</sup>.

**Figure 2.2** - Relative alignments between the FMO energies of the sensor active layer (S) and the analytes (A) and possible electrical effects.



Source: Author.

The HOMO and LUMO energies ( $E_{\text{HOMO}}$  and  $E_{\text{LUMO}}$ ) of all systems were estimated via Kohn-Sham eigenvalues (KS) and compared with those reported elsewhere<sup>64–66</sup>. The electronic gaps were estimated by  $E_{\text{gap}} = E_{\text{LUMO}} - E_{\text{HOMO}}$ . The optical properties of 9a and 9b (in particular the optical gap,  $E_{\text{opt}}$ ) were estimated via time-dependent (TD) DFT calculations, by using the same functional and basis set (i.e. TD-DFT/B3LYP/6-311G(d,p) approach).

The donation and acceptance indexes ( $R_D/R_A$ ) were estimated from the analysis of the relative electron accepting ( $\omega^+$ ) and electron donating ( $\omega^-$ ) powers of the compounds, estimated by<sup>67,68</sup>:

$$\omega^- = \frac{(3IP+EA)^2}{16(IP-EA)} \quad (2.1)$$

$$\omega^+ = \frac{(IP+3EA)^2}{16(IP-EA)} \quad (2.2)$$

where  $IP = E(N - 1) - E(N)$  and  $EA = E(N) - E(N + 1)$  represent, respectively, the ionization potential and electron affinity of the molecules. The  $R_D$  and  $R_A$  indexes are obtained by comparing  $\omega^+$  and  $\omega^-$  powers with those of sodium ( $\omega_{\text{Na}}^- = 3.46$ ) and fluorine ( $\omega_{\text{F}}^+ = 3.40$ ), respectively<sup>67,68</sup>:

$$R_D = \frac{\omega^-}{\omega_{\text{Na}}^-} \quad (2.3)$$

$$R_A = \frac{\omega^+}{\omega_{\text{F}}^+} \quad (2.4)$$

which are associated with charge transfer capacity of the compounds. All the calculations were conducted with the aid of Gaussian 16 computational package<sup>69</sup>.

The analytes that exhibited greater potential for detection by melanin-based compounds were considered in the adsorption studies. For this purpose, two distinct procedures were considered to generate substrate+analyte clusters:

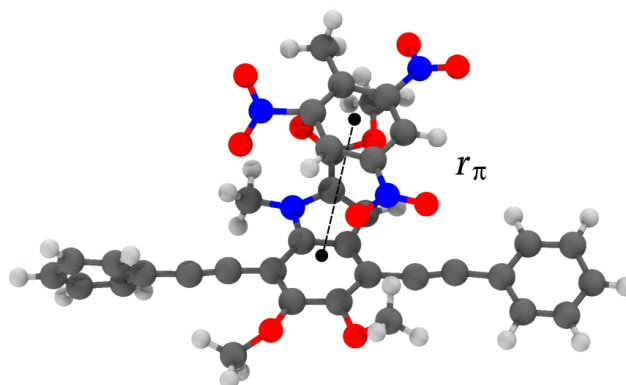
- i. *Adsorption guided by CAFIs*: the analytes were manually placed over the substrate structures considering the alignment of high CAFI values (e.g. the analytes were positioned so that their most reactive sites were close to the triple bonds of the melanin compound with a distance of 1.5 Å) and subjected to geometry optimization in a DFT/B3LYP/6-311G(d,p)/GD3 approach;
- ii. *Adsorption via docking submodule by automated interaction site screening (aISS)*<sup>70</sup>: done via aISS package and subjected to a tight binding geometry optimization (GFN2-xTB) to select more stable structures which were further optimized in a DFT/B3LYP/6-311G(d,p)/GD3 approach.

These systems were subjected to full geometry optimization and interaction calculations. All the calculations for the adsorbed systems were conducted considering the D3 version of Grimme's dispersion correction (GD3)<sup>71</sup>. The complexation energies were estimated using the counterpoise method, to correct the basis set superposition error (BSSE)<sup>72,73</sup>. The evaluation of partial density of states (PDOS) and weak interactions<sup>74,75</sup> were conducted with the aid of the MultiWFN computational package<sup>76</sup>.

Adsorbed structures stabilities were evaluated via NVT Born-Oppenheimer molecular dynamics (BOMD) simulations for selected systems (isolated compounds and those adsorbed with TNT and TNP) with the aid of DFTB+ software within the DFTB3 formalism<sup>77,78</sup>. Distinct temperatures were considered in the simulations (300, 400, 500 and 650 K), using a Nosé-Hoover thermostat. The Slater-Koster parameters were selected from the "3ob-1-1" set due to their excellent agreement with simulations conducted using the B3LYP functional<sup>79</sup>, ensuring consistency with the DFT approach methodology. DFT-D3 dispersion corrections were also incorporated<sup>80</sup>. A self-consistent charge (SCC) tolerance of  $10^{-6}$  over a total simulation time of 100 ps was considered with timestep of 0.97 fs (~10 times the period associated with the highest vibrational frequency of each configuration).

The stability of each adsorbed system was evaluated from the time-averaged density distribution,  $\rho(r_\pi)$  of the distance between the centers of mass of the analyte and the substrate,  $r_\pi$ , as illustrated in Figure 2.3.

**Figure 2.3** - Illustration of  $r_\pi$ , the distance between the centers of mass (depicted as black dots), for the 9a compound with the TNT analyte. This distance is tracked throughout each BOMD trajectory to obtain  $\rho(r_\pi)$ .



Source: Author.

Furthermore, to gain insight into the vibrational analysis, the autocorrelation approach for atomic velocities<sup>81-83</sup> and dipole moments was employed<sup>84,85</sup>. Given an intensive property, such as an atom's velocity,  $\vec{v}_i(t)$ , or the system's dipole moment,  $\vec{\mu}(t)$ , the normalized autocorrelation function can be computed, as expressed in Equation 2.5.

$$C_v(t) = \langle \vec{v}_i(0) \cdot \vec{v}_i(t) \rangle \quad (2.5)$$

where  $\vec{v}_i(t)$  and  $\vec{\mu}(t)$  represents the intensive property of interest at time  $t$ . These trajectories were sampled within 1 ps windows and averaged over the total trajectory time of 100 ps. As established in the literature, the Fourier transform of velocity and dipole moment autocorrelations provides insight into the Vibrational Density of States (VDOS) and Infrared (IR) spectra<sup>86</sup>. The peaks obtained can reveal infrared absorptions properties, displaying vibrational signatures typically usually observed in First-order Raman and IR experimental spectra.

## 2.4 Results and discussion

### 2.4.1 Isolated structures

Table 2.1 summarizes opto-electronic properties of compounds 9a and 9b, as well as experimental values reported in ref.<sup>7</sup>, estimated from the onset of the first oxidation and reduction potentials (in parentheses). As can be seen the theoretical results present a

reasonable agreement with the experimental values, mainly regarding the optical band-gaps. The theoretical evaluation of the oligomers' optical properties makes a correlatable, self-consistent estimation of the optical behavior of the 9a and 9b systems. Table 2.2 summarizes the electronic properties of NACs, which are in agreement with the values reported in the literature, measured by cyclic voltammetry, XPS and estimated by density functional theory <sup>31,64–66</sup>.

**Table 2.1** - Summary of opto-electronic properties of 9a and 9b eumelanin-based compounds.

Compound	Method	$E_{\text{HOMO}}$ (eV)	$E_{\text{LUMO}}$ (eV)	$E_{\text{gap}}$ (eV)	$E_{\text{opt}}$ (eV)
<b>9a</b>	Theory (Exp.)	-5.36 (-5.55)	-2.16 (-2.70)	3.19 (2.85)	2.94 (2.94)
<b>9b</b>	Theory (Exp.)	-5.08 (-5.45)	-1.92 (-2.65)	3.17 (2.80)	2.90 (2.87)

Source: Author.

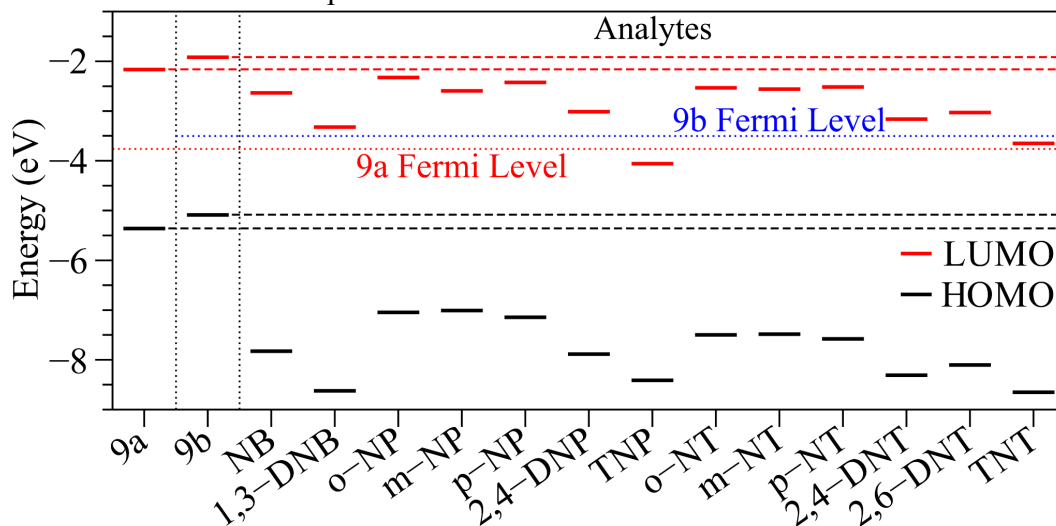
**Table 2.2** - Summary of theoretical electronic properties of the NACs.

Compound	Abbreviation	$E_{\text{HOMO}}$ (eV)	$E_{\text{LUMO}}$ (eV)
		this study (literature)	this study (literature)
nitrobenzene	<b>NB</b>	-7.82 (-7.59)	-2.63 (-2.43)
1,3-dinitrobenzene	<b>1,3-DNB</b>	-8.62 (-8.41)	-3.32 (-3.14)
<i>ortho</i> -nitrophenol	<b><i>o</i>-NP</b>	-7.04 (-7.21)	-2.32 (-2.23)
<i>meta</i> -nitrophenol	<b><i>m</i>-NP</b>	-7.01 (-7.18)	-2.59 (-2.88)
<i>para</i> -nitrophenol	<b><i>p</i>-NP</b>	-7.14 (-7.35)	-2.42 (-2.98)
2,4-dinitrophenol	<b>2,4-DNP</b>	-7.88 (-7.63)	-3.01 (-3.32)
trinitrophenol	<b>TNP</b>	-8.41 (-8.24)	-4.05 (-3.90)
<i>ortho</i> -nitrotoluene	<b><i>o</i>-NT</b>	-7.50 (-7.28)	-2.53 (-2.31)
<i>meta</i> -nitrotoluene	<b><i>m</i>-NT</b>	-7.48 (-7.27)	-2.56 (-2.36)
<i>para</i> -nitrotoluene	<b><i>p</i>-NT</b>	-7.57 (-7.57)	-2.51 (-2.50)
2,4-dinitrotoluene	<b>2,4-DNT</b>	-8.31 (-8.11)	-3.16 (-2.98)
2,6-dinitrotoluene	<b>2,6-DNT</b>	-8.10 (-7.27)	-3.03 (-2.36)
trinitrotoluene	<b>TNT</b>	-8.65 (-8.46)	-3.65 (-3.50)

Source: Author.

To first estimate the applicability of melanin-inspired 9a and 9b compounds as NAC sensors, comparative analyses of the relative alignments between their FMOs and the distinct analytes were conducted (Figure 2.4). The dashed lines in Figure 2.4 indicate the position of the FMOs and the dotted line Fermi Level of the non-doped systems ( $E_F = E_{\text{gap}}/2$ ).

**Figure 2.4** - Comparative analyses of the FMOs relative alignments of melanin-inspired compounds in relation to nitro-aromatics.



Source: Author.

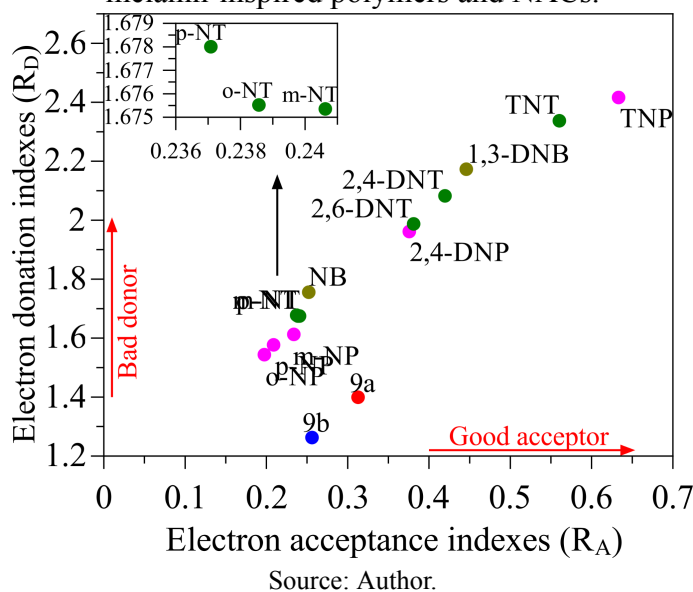
As a matter of fact, several factors can influence the efficiency of organic sensor devices. An important aspect is the relative position of the FMOs of the analytes in relation to the electronic gap of the active compounds<sup>63</sup>. From Figure 2.4 it is noticed that 9a and 9b monomers appear to be promising structures for NAC detections, mainly in relation to di- and tri-nitro aromatics. Note that, TNT can act as a *p*-type dopant for compound 9b, while TNP can act as a *p*-type dopant for both structures 9a and 9b. In general, the relative position of the FMOs allow us to suppose that NACs should act as electron traps in 9a or 9b, and then influence the optoelectronic properties of these materials.

In particular, the results presented in Figure 2.4 suggest that the presence of NACs can induce significant changes in electron transport mechanisms (and also in charge recombination) that could be monitored in electron-only devices (or ambipolar devices) via electrical (or optical) characterization (e.g. example, changes in current densities, electrical impedance, absorbance, etc).

To better interpret possible charge transfer effects between the structures, the donor-acceptor electron map (DAM) is presented in Figure 2.5. This map allows us to classify the systems as electron-donating ( $R_D$ ) and electron-accepting ( $R_A$ ) compounds. In general, low

$R_D$  values indicate a good donor, while high  $R_A$  defines good acceptors (as indicated by the red arrows).

**Figure 2.5** - Comparative analyses of the electron donation/acceptance indexes of melanin-inspired polymers and NACs.



It can be seen that 9a and 9b monomeric structures are better donors than NACs (differences between 9a and 9b are due to terminal methoxy groups). Tri-nitroaromatics in particular are good electron acceptors and poor donors, followed by di- and mono-nitroaromatics. In particular, the higher electron affinity of TNT and TNP indicates an effective interaction of these analytes with the monomers 9a and 9b.

From Figures 2.4, 2.5 and A1, a stronger interaction of the monomers with the NACs 1,3-DNB, 2,4-DNP, 2,4-DNT, 2,6-DNT, TNP and TNT can be deduced, considering their ability to insert unoccupied states into the 9a and 9b band gaps and their corresponding electron acceptor/donation indices. For this reason, only these analytes were selected for the adsorption studies.

To interpret the interaction between compound 9 and NACs, the local reactivity of the compounds was investigated. Figures 2.6 and 2.7 summarize the CAFIs and MEPs of NACs and the structures of the compounds. Red and blue sites presented in CAFI (MEP) maps represent, respectively, reactive (negatively charged) and non-reactive (positively charged) sites. In general, sites with higher values of  $f^+$ ,  $f^-$  and  $f^0$  (red sites) represent regions that are prone to interact with nucleophiles (being prone to receive electrons), electrophiles (losing electrons) and free radicals (with no changes in the total number of electrons), respectively.

**Figure 2.6** - CAFIs and MEPs estimated for NACs.

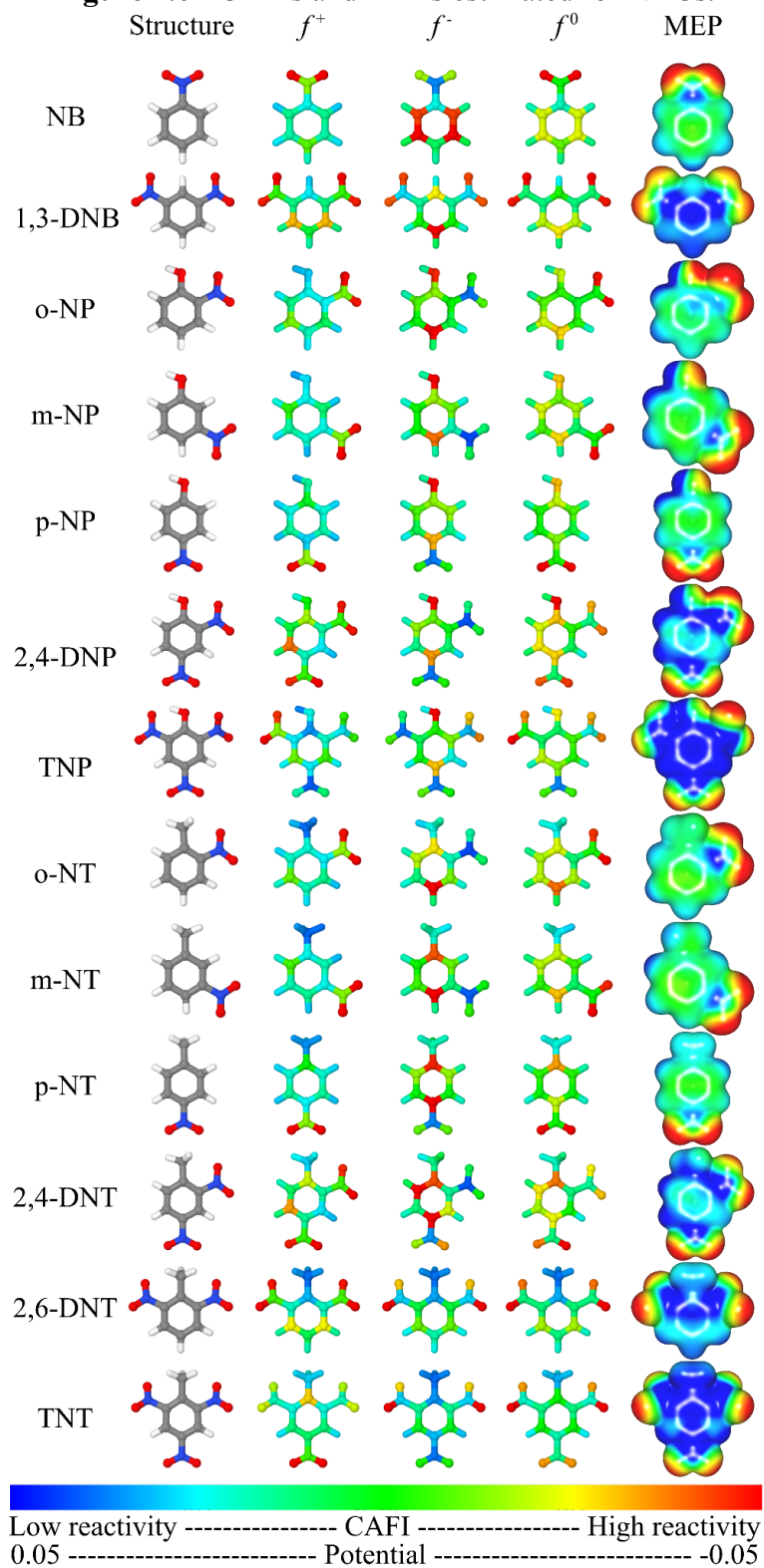
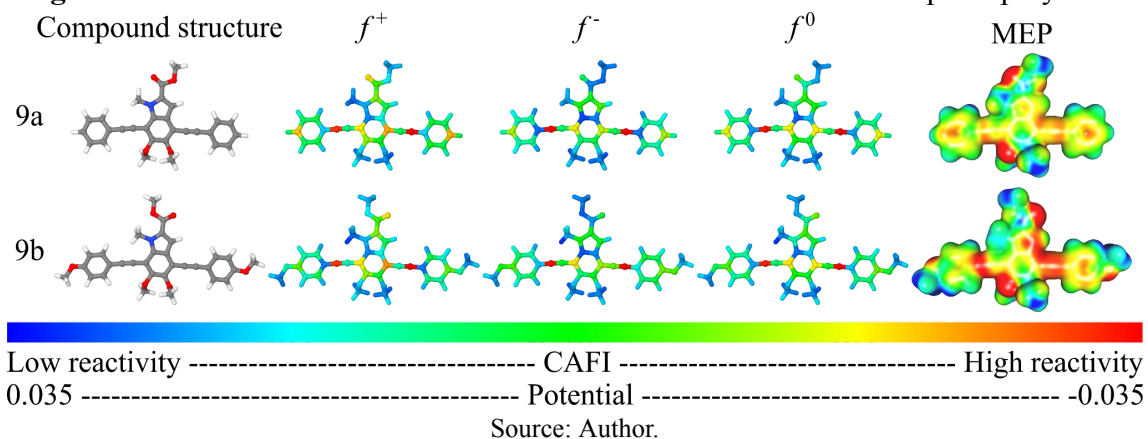


**Figure 2.7** - CAFIs and MEPs of monomeric structures of melanin-inspired polymers.



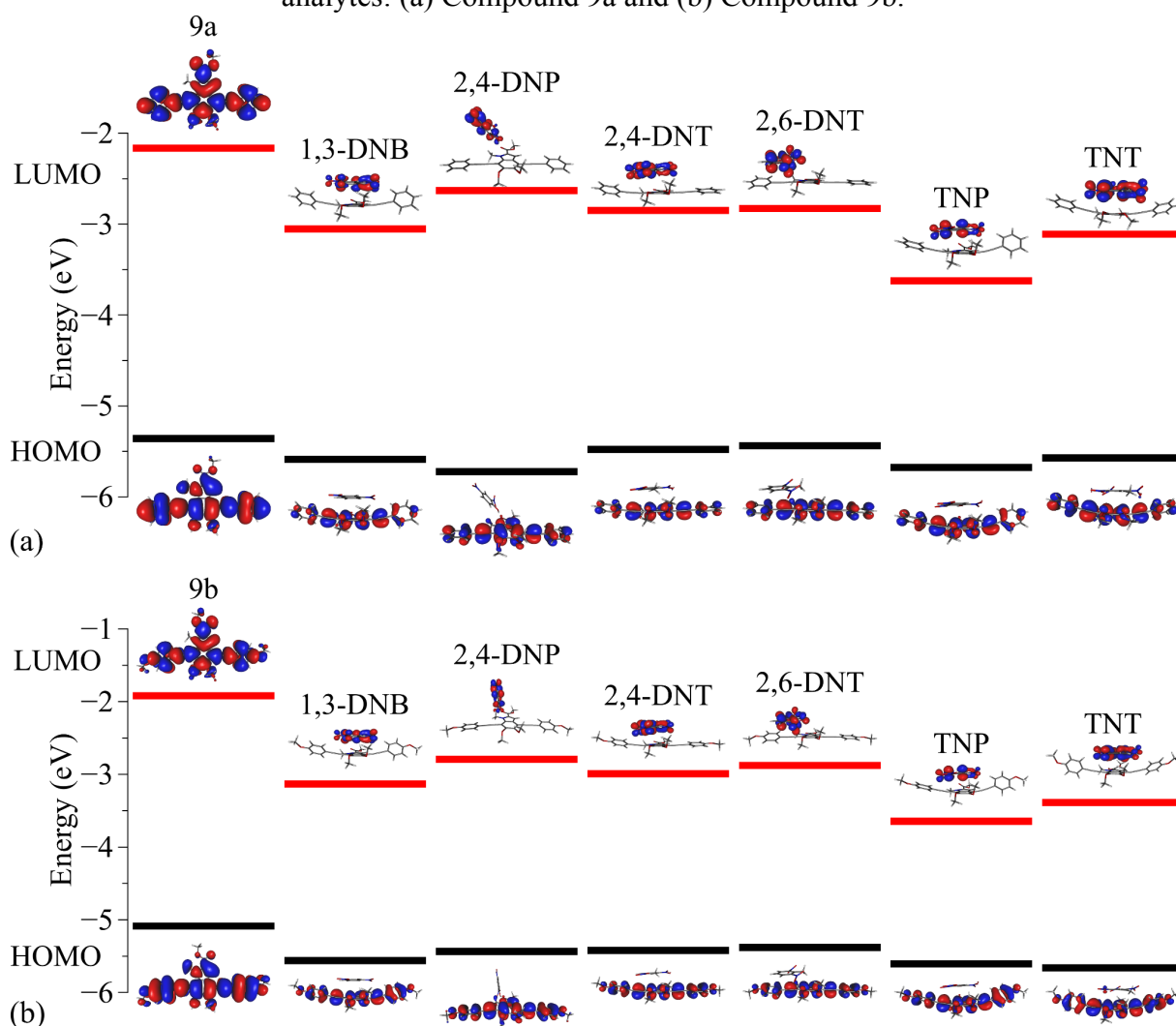
Note that electron acceptance of nitro-aromatic compounds is concentrated on the nitro groups (i.e., high  $f^+$  values), while electron donation is centered on the ring atoms for compounds with one nitro group and on  $-\text{NO}_2$  for compounds with two or three nitro groups (i.e., high  $f^-$  values). Hydroxyl groups also play an important role in relation to  $f^-$ . The most reactive regions of compounds 9a and 9b are centered on the  $\text{C}\equiv\text{C}$  groups in both structures, suggesting that these regions are the most important sites for charge transfer processes.

#### 2.4.2 Adsorbed structures

All the adsorbed structures obtained by the docking submodule (aSSI) exhibited higher energy values compared to the structures from CAFI's guided adsorption method after the geometry optimization, even those structures that showed hydrogen bonds are less energetic (see Figure A2). Such result evidences the relevance of considering CAFIs as effective adsorption center predictors, as already proposed elsewhere<sup>55,86,87</sup>. In this sense, for simplicity, only the results coming from CAFI-based methods are presented (results coming from aSSI are shown in the Appendix A).

Figure 2.8 shows the spatial and energy distribution and Kohn-Sham frontier molecular orbitals of the adsorbed systems.

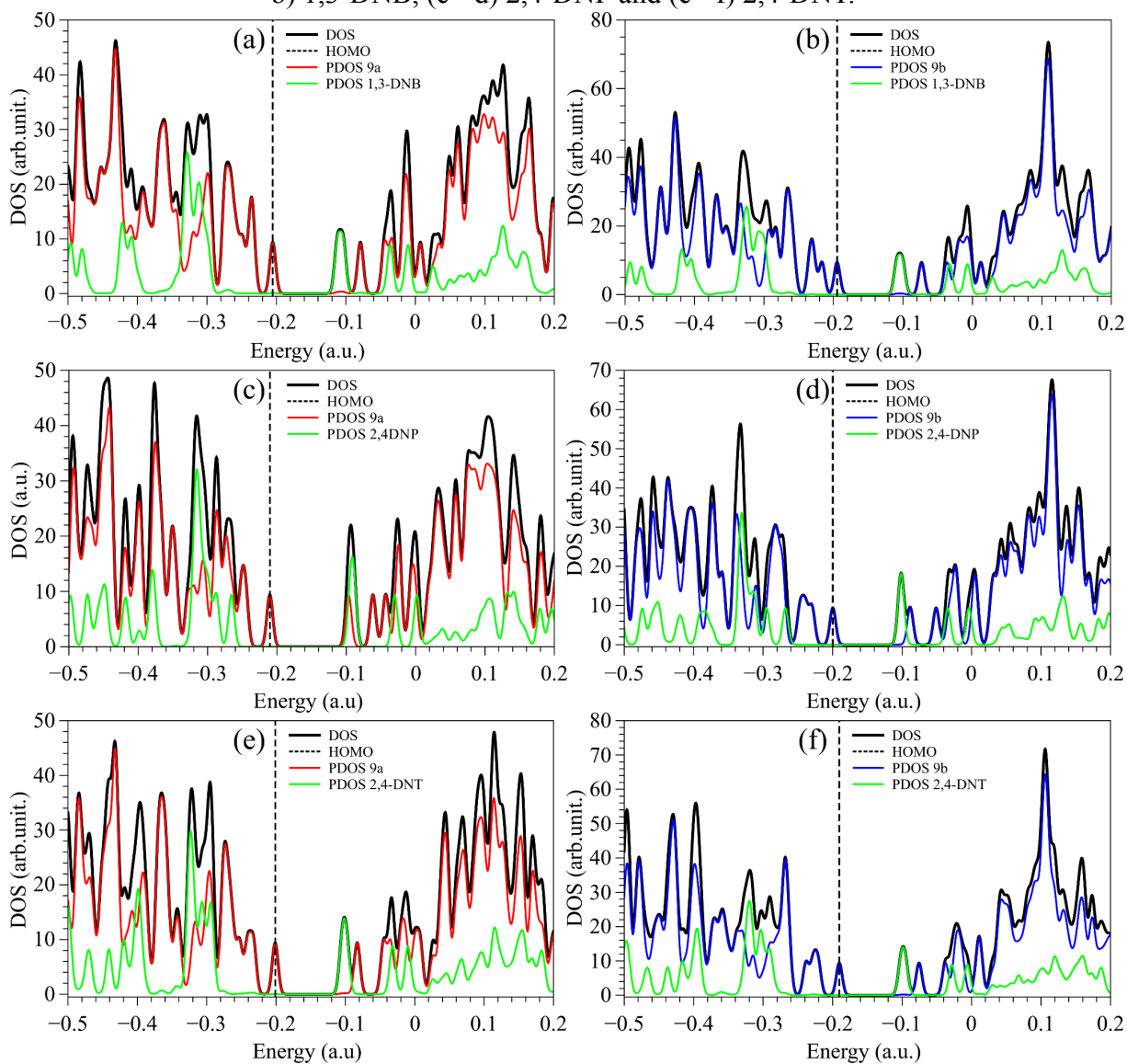
**Figure 2.8** - Spatial distribution and energy levels of the FMOs over the monomer and analytes: (a) Compound 9a and (b) Compound 9b.



Note that, in both cases, the HOMO is localized on the melanin-based compound, while the LUMO is mainly located on the analytes. As preliminarily predicted in Figure 2.5 and confirmed by CAFI (Figures A3 and A4 in the Appendix A), the LUMO energy level of the adsorbed structure is primarily influenced by the analytes, resulting in a smaller band gap compared to the isolated compound.

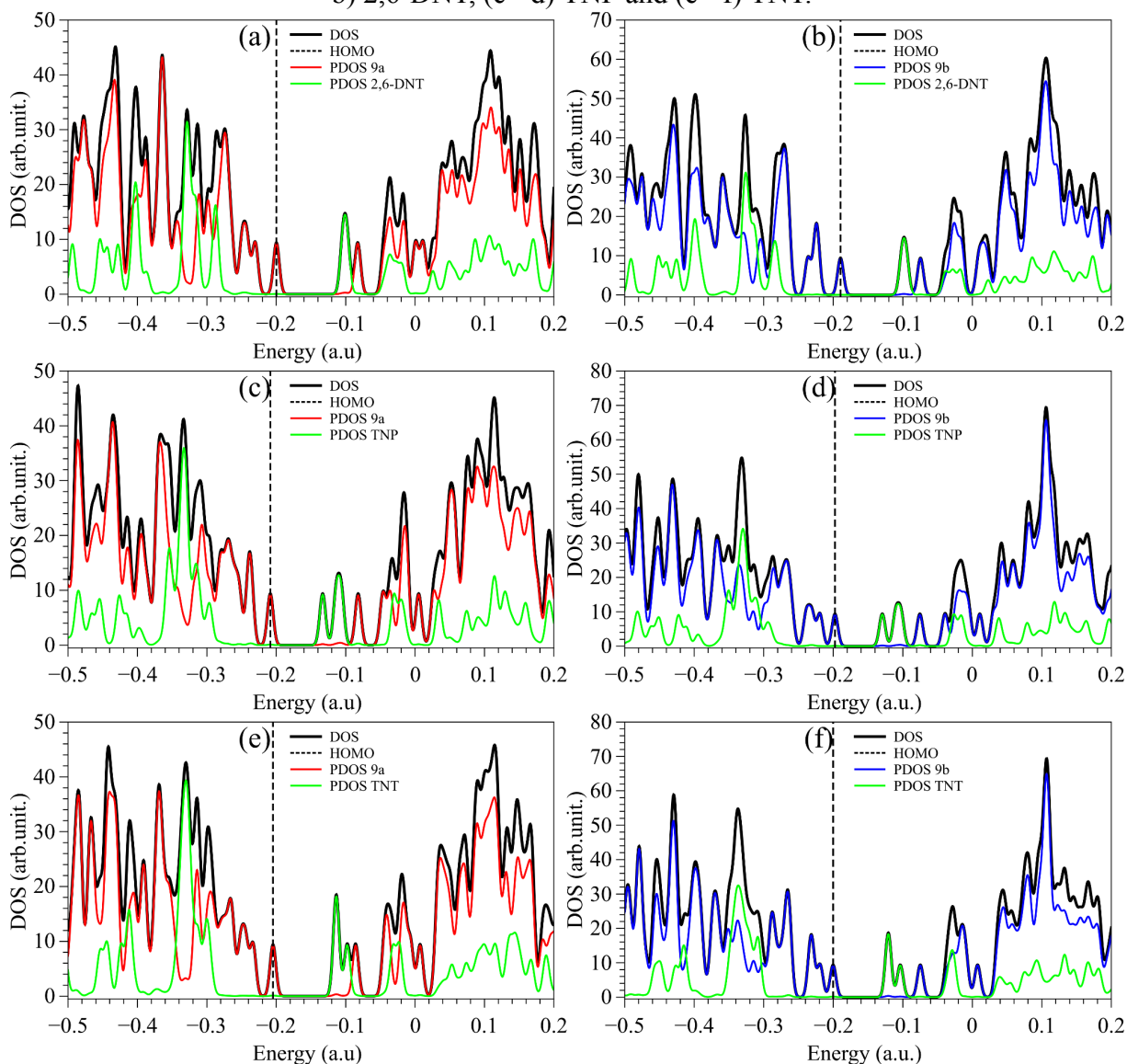
Figures 2.9 and 2.10 illustrate the partial and total density of states (PDOS and DOS) representation of the adsorbed structures that evidence the dominance of the melanin-based substrates and analytes on the HOMO and LUMO, respectively. Red, blue and green curves define the PDOS of compound 9a, compound 9b, and the analytes, respectively. The position of HOMO is indicated by the vertical dashed line.

**Figure 2.9** - DOS and PDOS of melanin-inspired compounds 9a (left) and 9b (right) with: (a - b) 1,3-DNB, (c - d) 2,4-DNP and (e - f) 2,4-DNT.



Source: Author.

**Figure 2.10** - DOS and PDOS of melanin-inspired compounds 9a (left) and 9b (right) with: (a - b) 2,6-DNT, (c - d) TNP and (e - f) TNT.



Source: Author.

Similarly to Figure 2.8, all the HOMOs (dashed lines) are dominated by the melanin-based compound, while the LUMO is predominantly associated with the analytes (similar results are shown in Figures A8 and A9). Note that FMO alignments evidence an effective electron trapping behavior of the analytes, with potential implications in photoluminescence and exciton dynamics, by photoinduced electron transfer. Indeed, a number of studies have reported the effective fluorescence quenching induced by nitroaromatics (specially TNT)<sup>31,88</sup>. A similar effect should take place for 9a and 9b, once they present high photoluminescence quantum yields<sup>7</sup>. In particular, higher spatial overlap matrix elements  $\langle \phi_{\text{HOMO}} ||| \phi_{\text{LUMO}} \rangle$  (which play a key role in fluorescence quenching) are

observed for 1,3-DNB, TNP, and TNT, suggesting enhanced sensitivity to these compounds (see Appendix A).

To better evaluate the compound+analyte interaction, the complexation energies (Figure 2.11) and weak interaction areas (Figure 2.12) were investigated. Complexation energies are widely used as essential descriptors of sensor performance. In general, absolute values lower than 0.5 eV indicate weak physisorption, while those in the range of 0.6 to 1.2 eV are considered optimal, offering a balance between binding strength and desorption efficiency. Absolute values exceeding 1.2 eV typically reflect strong chemisorption, which may hinder analyte desorption and sensor reusability<sup>89-93</sup>.

**Figure 2.11** - Complexation Energy of analytes on melanin-inspired compounds.

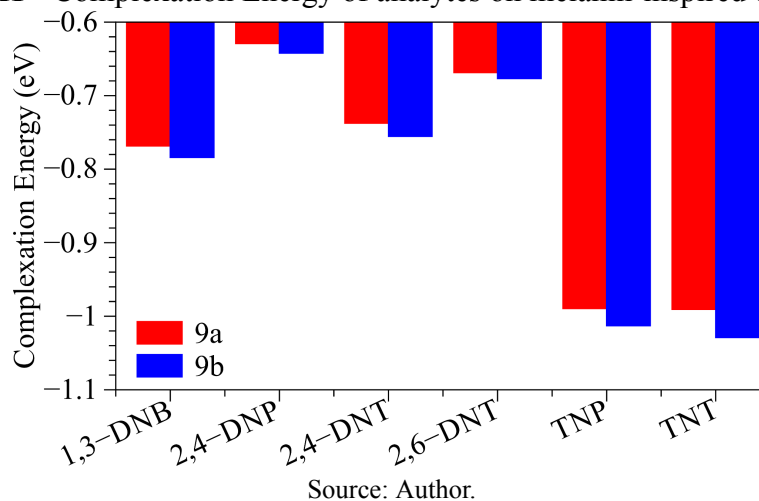


**Figure 2.12** - Analyte-melanin-based compound interactions: strength and interaction areas.

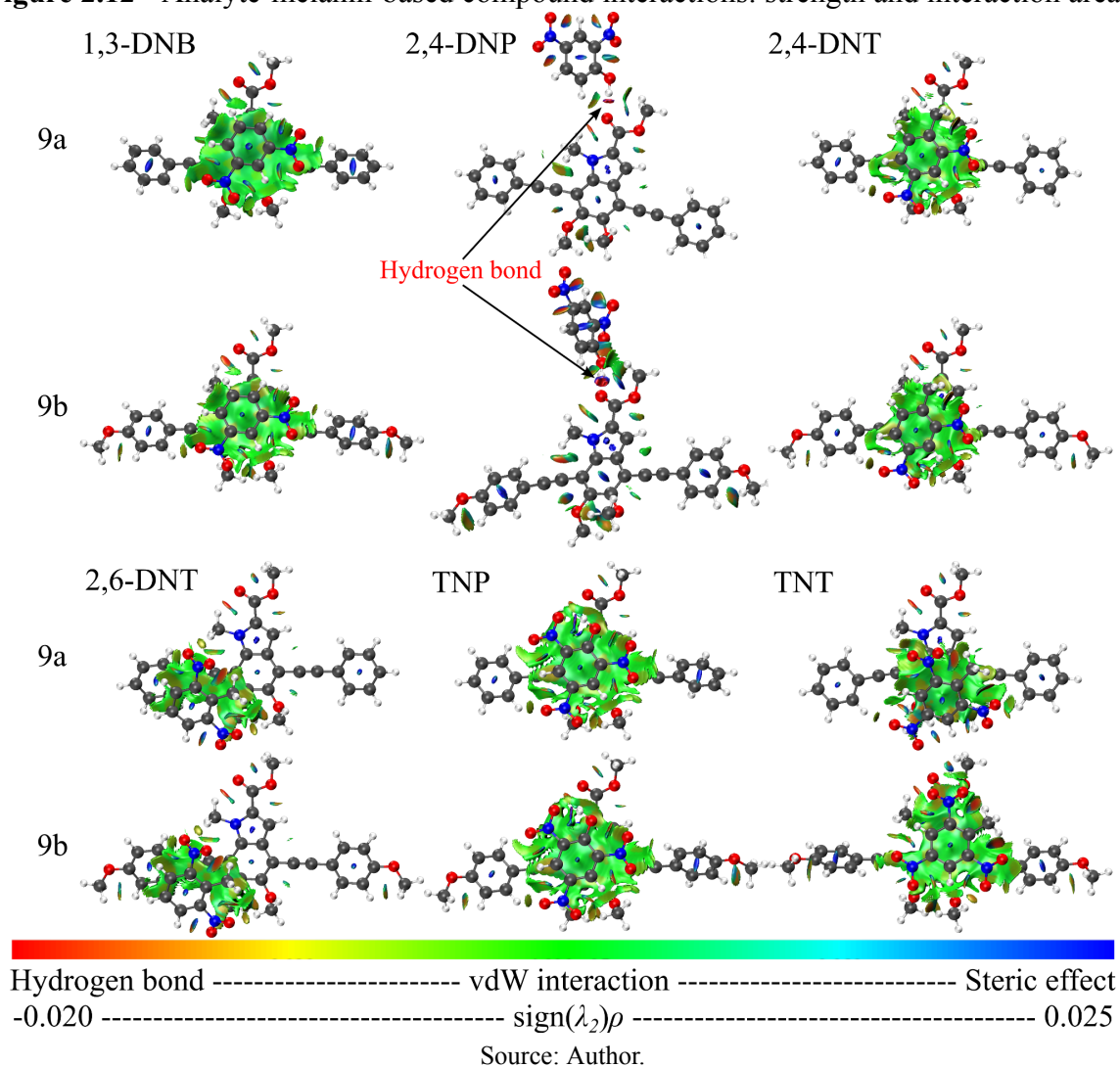


Figure 2.11 reveals lower complexation energy in both systems (9a and 9b) when interacting with 2,4-DNP and 2,6-DNT, which is consistent with the smaller interaction area presented in Figure 2.12. On the other hand, higher complexation energies and interaction areas are observed with TNP and TNT. Note that absolute values around 0.6-1.0 eV are obtained for all the systems, combining adequate binding with reversible analyte release. In particular, our melanin-inspired systems exhibit interaction strengths comparable to those of established materials, including  $\text{C}_5\text{N}_2$  (-1.37 to -1.49 eV for TNT and PA)<sup>94</sup> and Pd-decorated  $\text{MoSi}_2\text{N}_4$  (-1.21 eV for nitrobenzene)<sup>95</sup>.

It is worth noting that most systems exhibit significant van der Waals (vdW) interactions (highlighted in green and yellow), with only the 2,4-DNP complex displaying a hydrogen bond. This specific interaction arises from the particular geometry adopted during optimization and influences the nature of the electronic transitions: in the 9a+2,4-DNP

complex, both the HOMO and LUMO are localized on the substrate (compound 9a), whereas in the 9b+2,4-DNP complex, the HOMO is localized on the substrate and the LUMO on the analyte (see Figure 2.8 and 2.9). Interestingly, systems obtained via the automated docking method (aISS) adopted similar configurations to those guided by CAFI (see Figure A10, Appendix A), displaying dominant  $\pi$ - $\pi$  stacking interactions. These structures consistently showed HOMO localization on the substrate and LUMO on the analyte, along with higher complexation energies, highlighting a preferred orientation for charge transfer processes.

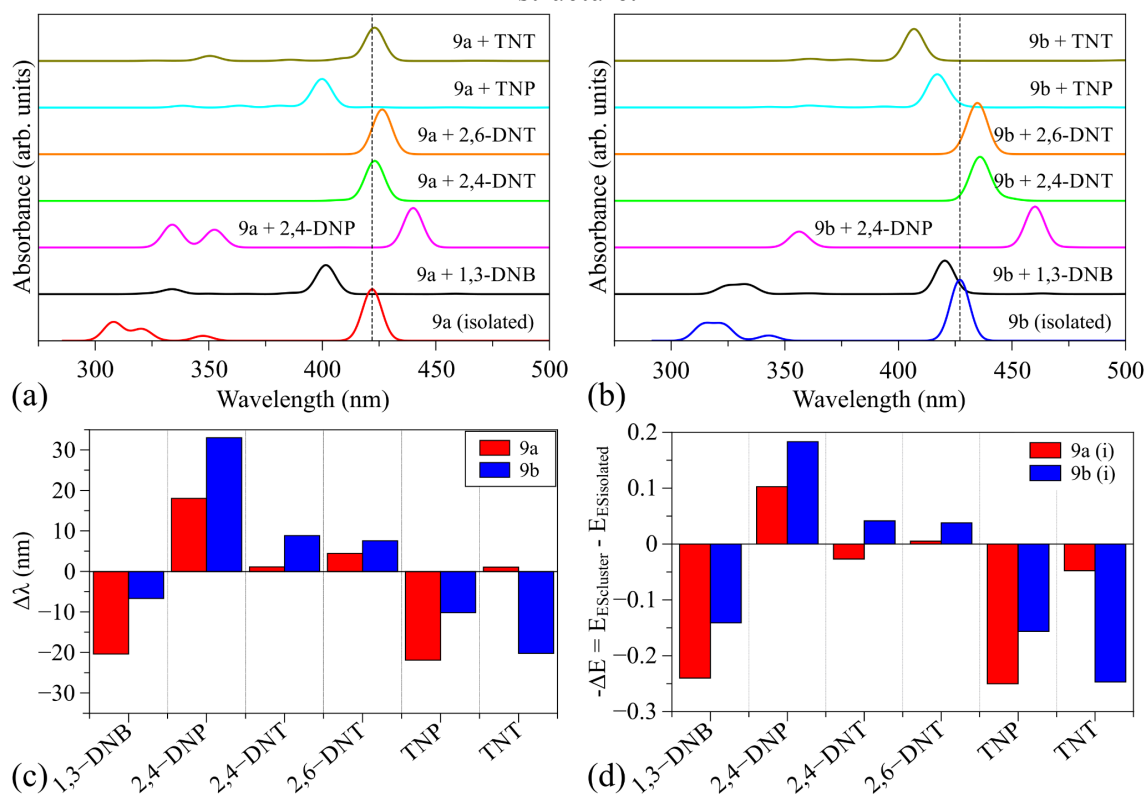
Regardless of the adsorption method employed, both approaches indicated strong and favorable interactions between the melanin-based compounds and analytes such as TNT and TNP, reinforcing the robustness of the interaction pattern across computational protocols.

To investigate the selectivity of the compounds, additional adsorption studies were carried out with common atmospheric compounds,  $N_2$  and  $O_2$  (at triplet state) using the same theoretical approach used for the NACs. Both analytes exhibited low adsorption: the interaction energies for  $N_2$  ( $O_2$ ) was around 8x (10x) lower than those calculated for TNP and TNT. These results suggest non-effective interactions, evidencing the selectivity of our systems towards NACs. All corresponding energy values are detailed in Table A3 of the Appendix A.

Additional information regarding 9a/b+NACs system stability was assessed by recovery time ( $\tau$ ) estimation (time required to analyte desorption from the substrate<sup>95</sup>), which shows  $\tau$  ranging from few hours for  $T = 300$  K up to microseconds for  $T = 650$  K under visible light irradiation (see Table A2 in Appendix A).

To estimate the possible optical response of such melanin-based substrate to the analytes, additional calculations were conducted for the absorbed systems in the framework of the TD-DFT/B3LYP/6-311G(d,p). Figure 2.13a and b depicts the absorption spectra of compounds 9a and 9b isolated and adsorbed with distinct NACs, as well as the main peak shift noticed for each substrate/analyte system, Figure 2.13c presents the numerical shift observed in Figure 2.13a and b. Figure 2.13d shows the negative variation of the excited state energy for the most representative transition in the vertical transition.

**Figure 2.13** - Theoretical optical absorption spectra of (a) compounds 9a and (b) 9b: isolated and adsorbed with NACs (gaussian curves with half width of 5 nm). The variations in (c) wavelength absorption and (d) excited state energy of the cluster compared to the isolated structure.



Source: Author.

Note that, in general, the NACs adsorption leads to significant changes on the main peak optical absorption of the substrates, which depends on the compound 9a or 9b. Some interesting trends can be observed, dividing the compounds in hypsochromic (blue shifted: 1,3-DNB; and TNP), bathochromic (red shifted: 2,4-DNP; 2,4-DNT; and 2,6-DNT) and anomalous (with no pattern: TNT) analytes.

Significant deviations are noticed for 1,3-DNB ( $\Delta\lambda = -20.4$  nm), 2,4-DNP ( $\Delta\lambda = +18.1$  nm) and TNP ( $\Delta\lambda = -21.9$  nm) in relation to compound 9a, with very small changes for the others (i.e.  $\Delta\lambda < 5$  nm). For compound 9b the most relevant optical responses were observed for 2,4-DNP ( $\Delta\lambda = 33.0$  nm) and TNT ( $\Delta\lambda = -20.2$  nm); with intermediate responses for the other analytes: 1,3-DNB ( $\Delta\lambda = -6.6$  nm); 2,4-DNT ( $\Delta\lambda = 8.9$  nm); 2,6-DNT ( $\Delta\lambda = 7.6$  nm); and TNP ( $\Delta\lambda = -10.2$  nm).

These changes can be rationalized in terms of inductive effects and/or the introduction of new electronic states within the substrate band gaps<sup>87</sup>. In fact, the insertion of empty levels (analytes' LUMOs) inside the 9a and 9b gaps should lead to systems with reduced band gaps, as indeed observed in Figure 2.8, 2.9 and 2.10. Such changes were supposed to result in

bathochromic optical effects for all the systems with a relative amplitude of  $96 \pm 49$  nm (for 9a) and  $135 \pm 57$  nm (for 9b) (compatible with  $\Delta E_{\text{gap}} -0.6 \pm 0.2$  and  $-0.8 \pm 0.2$  eV, respectively), which is indeed observed with very small amplitude ( $< 1.4 \times 10^{-2}$ ) for systems 9a+1,3-DNB and 9b+1,3-DNB respectively.

The distinct dominant optical responses obtained for the systems are associated with the low superposition of the resulting FMOs, as evidenced in Figure 2.8, indicating a low probability of a HOMO (old - 9a/9b centered) to LUMO (new - analyte centered) transitions and showing mainly H-L<sub>2</sub> or H-L<sub>3</sub> (9a/9b centered) transitions (see Figures 2.9 and 2.10, as well as Table A1 in the Appendix A). Figure 2.13c shows the variation of E<sub>ES</sub> (excited state energy) of the cluster in relation to the isolated compounds. It is important to note that greater variations in the energies of excited states lead to larger shifts in the optical absorption spectrum. With the exception of 9a with 2,4-DNT and TNT clusters, a decrease in energy results in a red shift, while an increase in energy results in a blue shift.

The resulting spectra are governed by inductive effects and small perturbations of the electronic structures by the presence of intermediate levels. In particular it is noticed that effective interactions between reactive oxygen atoms of the nitro groups (with high  $f^+$  values) of NACs with substrate triple bonds (with high  $f^-$  values) lead to significant hypsochromic effects noticed for 1,3-DNB, TNP (for compounds 9a and 9b), and TNT (for compound 9b). This configuration indicates an effective substrate-to-analyte electron transfer process, which weakens the  $\pi$ -systems of the substrates, reducing their effective conjugation lengths and promoting the hypsochromic responses. The absence of significant changes on the 9a+TNT system in relation to 9b+TNT is due to the absence of NO<sub>2</sub>-triple bond interaction noticed for 9b (replaced by CH<sub>3</sub>-triple bond interaction). The redshift associated with 2,4-DNP is linked to the formation of O-H bonds, which improves the aromaticity on central rings of the substrates. The observed variability in optical absorption shifts may be attributed to the diversity of interaction types ( $\pi$ - $\pi$  stacking, NO<sub>2</sub>-C $\equiv$ C interactions, and hydrogen bonding) and the specific adsorption geometries adopted by each analyte. While such orientation differences influence local electronic transitions and complexation energies, they do not significantly alter the overall HOMO-LUMO gap closure, which remains consistently reduced across systems. The combined analysis of adsorption energies and frontier molecular orbitals (including relative alignments and spatial overlaps) provides a useful metric for evaluating the sensor's relative sensitivity to each analyte. In particular, the higher spatial overlap matrix elements and stronger adsorption energies observed for TNP and TNT support their selection for further stability assessment via BOMD simulations.

These theoretical findings can be meaningfully compared with experimental data from similar eumelanin-inspired molecules<sup>48</sup>. Notably, Selvaraju et al. reported that indole-based conjugated systems with phenylene ethynylene linkers exhibit modulated HOMO-LUMO energy levels and bandgaps depending on terminal substituents behavior that parallels the analyte-induced bandgap shifts observed in our work. Importantly, their study shows that nitroaromatics effectively quench photoluminescence, attributed to LUMO localization on the NO<sub>2</sub>-containing analyte and HOMO retention on the substrate, thus facilitating photoinduced electron transfer (PET). This agrees with the orbital alignments and spatial overlaps observed in our adsorbed systems, particularly for TNP and TNT. The consistent HOMO-LUMO separation and electronic coupling strongly support fluorescence quenching as a more robust sensing mechanism. These insights highlight the importance of future experimental studies on photoluminescent responses for validating and expanding the detection capabilities of melanin-inspired platforms.

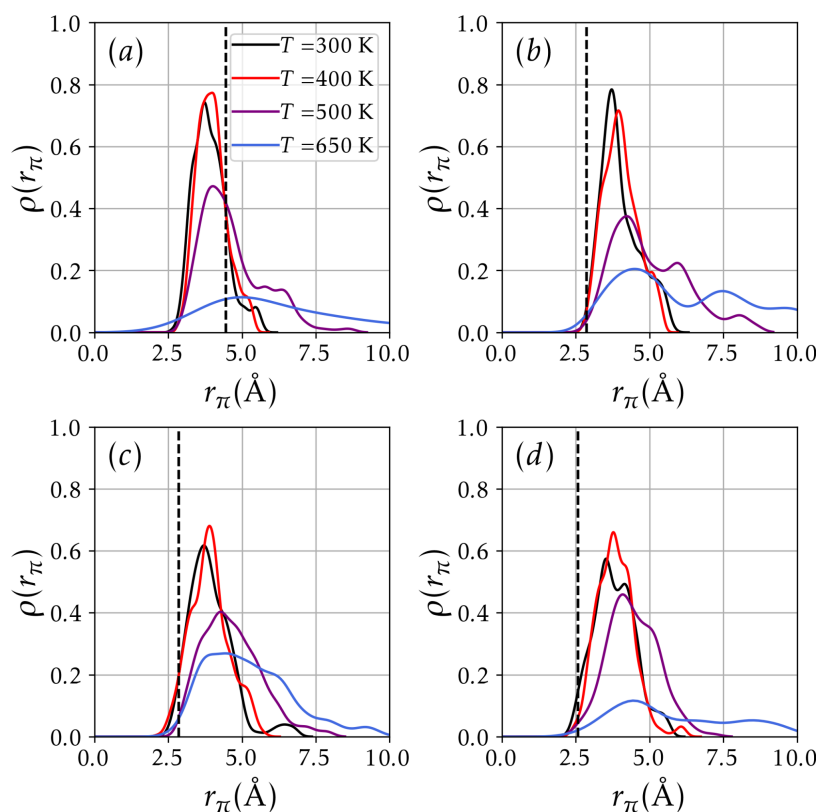
### 2.4.3 Born-Oppenheimer molecular dynamics

Figures 2.14 and 2.15 summarize key results derived from the Born-Oppenheimer molecular dynamics (BOMD) simulations, providing dynamic insights into the structural stability and vibrational behavior of the analyte–substrate complexes under thermal stress.

Figure 2.14 shows the time-averaged density distribution of the distance between the analyte/substrate centers of mass, coming from BOMD simulations. Note that across all systems, increasing the temperature (and consequently the kinetic energy) leads to greater average displacement of the analyte from its initial position, reflected in broader  $\rho(r_\pi)$  distributions and decreased peak intensity. This behavior is consistent with reduced interaction strength and higher desorption probabilities at elevated temperatures.

Notably, although the timescales explored in the simulations are shorter than those expected for analyte dissociation at ambient temperature and 400 K, the broadening of  $\rho(r_\pi)$  suggests that, as temperature increases, the analyte moves further from its initial position, increasing the probability of dissociation.

**Figure 2.14** - Distribution of  $\rho(r_\pi)$  over the 100 ps trajectories for the (a) 9a+TNT, (b) 9a+TNP, (c) 9b+TNT, and (d) 9b+TNP systems. In all panels, the vertical black dashed line represents the initial value of  $r_\pi$ .

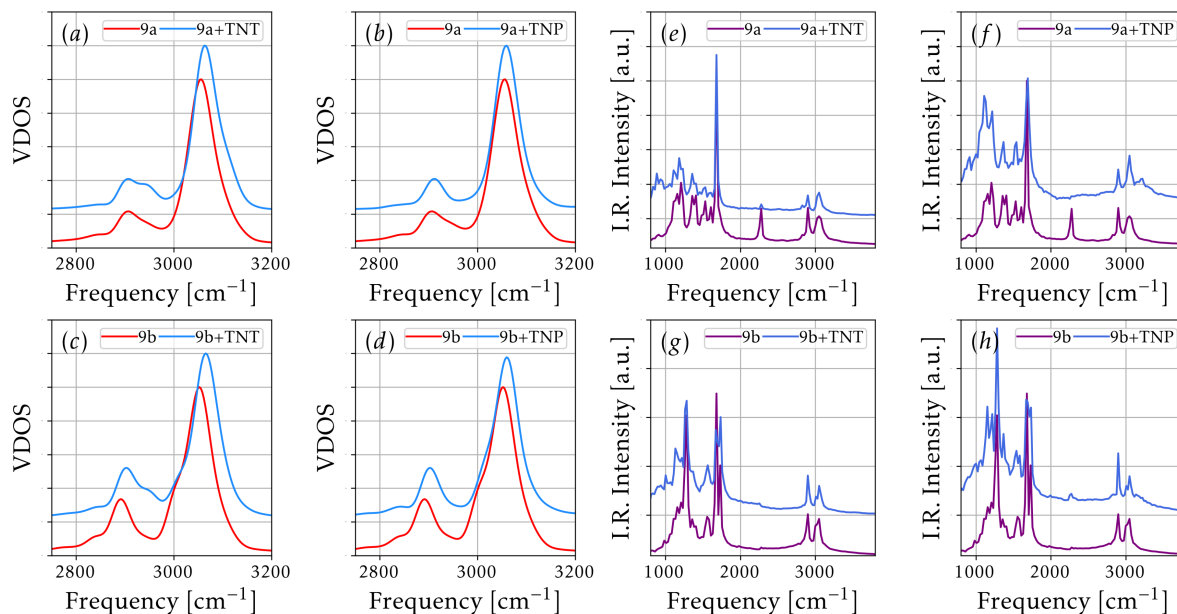


Source: Author.

Furthermore, it's possible to note the dissociation of the 9a+TNT and 9b+TNP systems at  $T = 650$  K. The full trajectory videos are included in the [Google Drive folder](#), reinforcing the argument that the adsorption dissociation time is greatly reduced as temperature increases.

Figure 2.15 shows the velocity and dipole autocorrelation functions estimated for adsorbed and isolated compounds for  $T = 300$  K.

**Figure 2.15** - Vibrational Density of States obtained from the Fourier transform of the velocity autocorrelation function for: (a) 9a+TNT, (b) 9a+TNP, (c) 9b+TNT, and (d) 9b+TNP systems. In all panels, a shift toward higher frequencies is observed upon analyte adsorption. The resulting Infrared spectrum obtained from the dipole autocorrelation function, are shown in panels: (e) for 9a+TNT, (f) for 9a+TNP, (g) for 9b+TNT, and (h) for 9b+TNP.



Source: Author.

These results demonstrate that both 9a and 9b compounds exhibit a noticeable shift towards higher frequencies upon adsorption of TNT and TNP nitroaromatic compounds (NACs). While the peak positions in the VDOS and IR spectra remain largely consistent between the pristine substrates and the adsorbed complexes-reflecting the intrinsic vibrational modes of the organic framework<sup>96</sup>, the overall spectral shift suggests that compounds 9a and 9b are promising candidates for NAC sensing involving Raman and IR spectra.

In summary, our results suggest that changes in electronic and vibrational properties upon NAC adsorption could be probed via electrical (I-V, impedance, conductivity), optical (fluorescence quenching) and vibrational (IR, Raman) measurements, supporting the use of these low-cost materials as promising NAC sensors.

## 2.5 Conclusions

In this study, the sensing capabilities of melanin-inspired compounds toward nitroaromatic compounds (NACs) were systematically investigated using density functional theory (DFT) and Born-Oppenheimer molecular dynamics (BOMD) simulations.

The results reveal that di-nitro and tri-nitro NACs (particularly TNT and TNP) modulate the electronic, optical and vibrational properties of the modeled systems. In general, the responses are robust across multiple adsorption relative positions.

Strong analyte-substrate interactions are noticed for these compounds, which also present moderate estimated recovery time under mild conditions. BOMD indicate that complexes are stable even under ambient and moderately elevated temperatures.

Our results highlight the potential of melanin-inspired derivatives as suitable materials for chemiresistive and electrochemical sensors. Although the adsorbed systems exhibited notable modulation in electronic and vibrational properties, no consistent trend was observed in the optical absorption shifts across all analytes. This underscores the limitation of using optical absorption alone as the sensing mechanism. Nevertheless, the bandgap reduction induced by analyte adsorption suggests a potential for luminescence-based detection strategies. In this sense, the investigation of photoluminescence and exciton dynamics represents a promising direction for the development of eumelanin-based nitroaromatic sensing platforms.

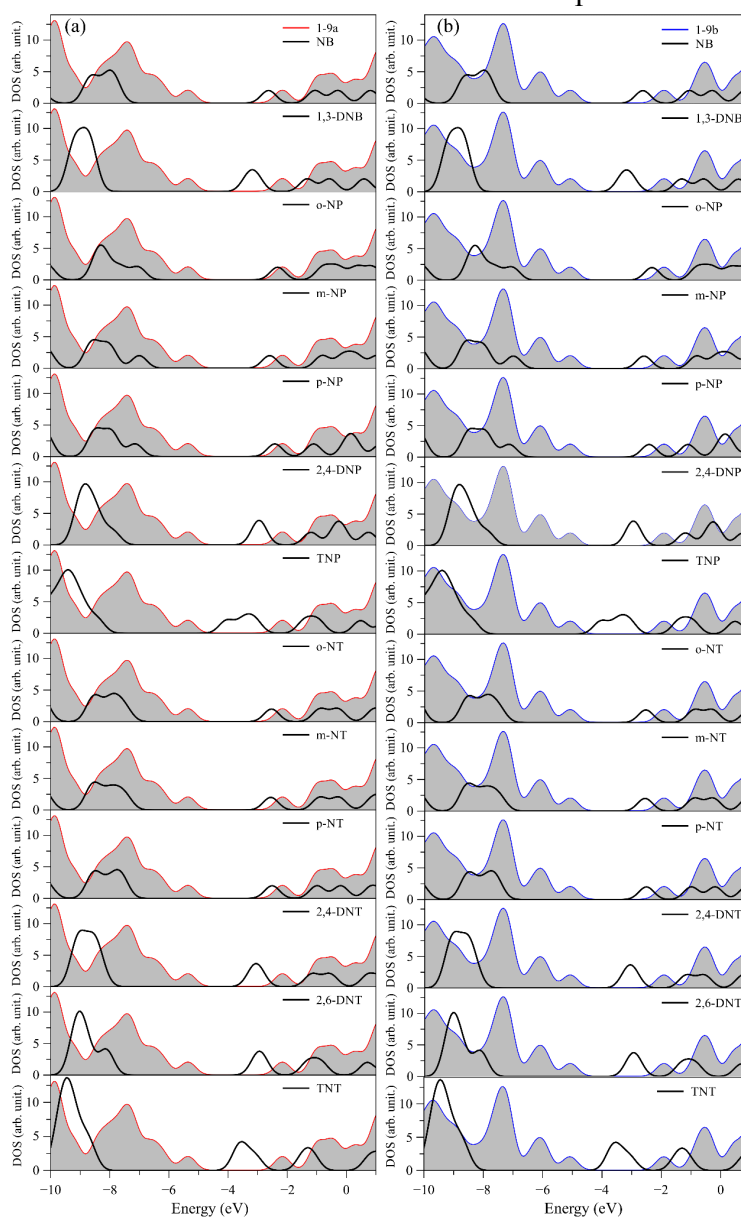
Their favorable optoelectronic and vibrational properties, combined with appropriate adsorption energies, support their use in the selective and reversible detection of nitroaromatic compounds. Consistent with experimental findings from related systems, these results position compounds 9a and 9b as promising candidates for the development of low-cost, sustainable sensor platforms, while also guiding the rational design of new bioinspired sensing materials.

## APPENDIX A – Melanin-Based Compounds as Low-Cost Sensors for Nitroaromatics: Theoretical Insights on Molecular Interactions and Opto-Electronic Responses

### A1. Total density of states (DOS) of compounds 9a, 9b and NACs

Figure A1 shows the DOS of compounds 9a and 9b superimposed to the NACs. Note that the LUMO of the analytes 1,3-DNB, 2,4-DNP, 2,4-DNT, 2,6-DNT, TNP and TNT are located into the band gap of the melanin-inspired compounds.

**Figure A1** - Comparative analyses of the DOS melanin-inspired polymers (a) 9a and (b) 9b in relation to all the Nitro-aromatics compounds.

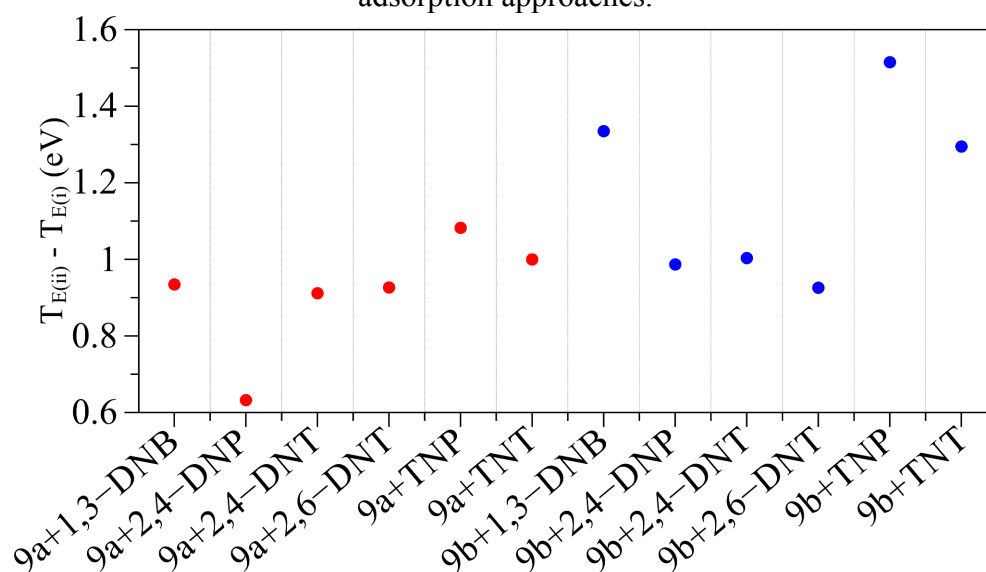


Source: Author.

## A2. Adsorption methodologies

Two distinct adsorption processes were employed to generate substrate+analyte clusters: (i) adsorption guided by CAFI and (ii) Adsorption via docking submodule by automated interaction site screening (aISS). Figure A2 presents the total energy variation between each approach. Note that all variations result in positive values showing that the approach  $i$  leads to clusters with lower total energies.

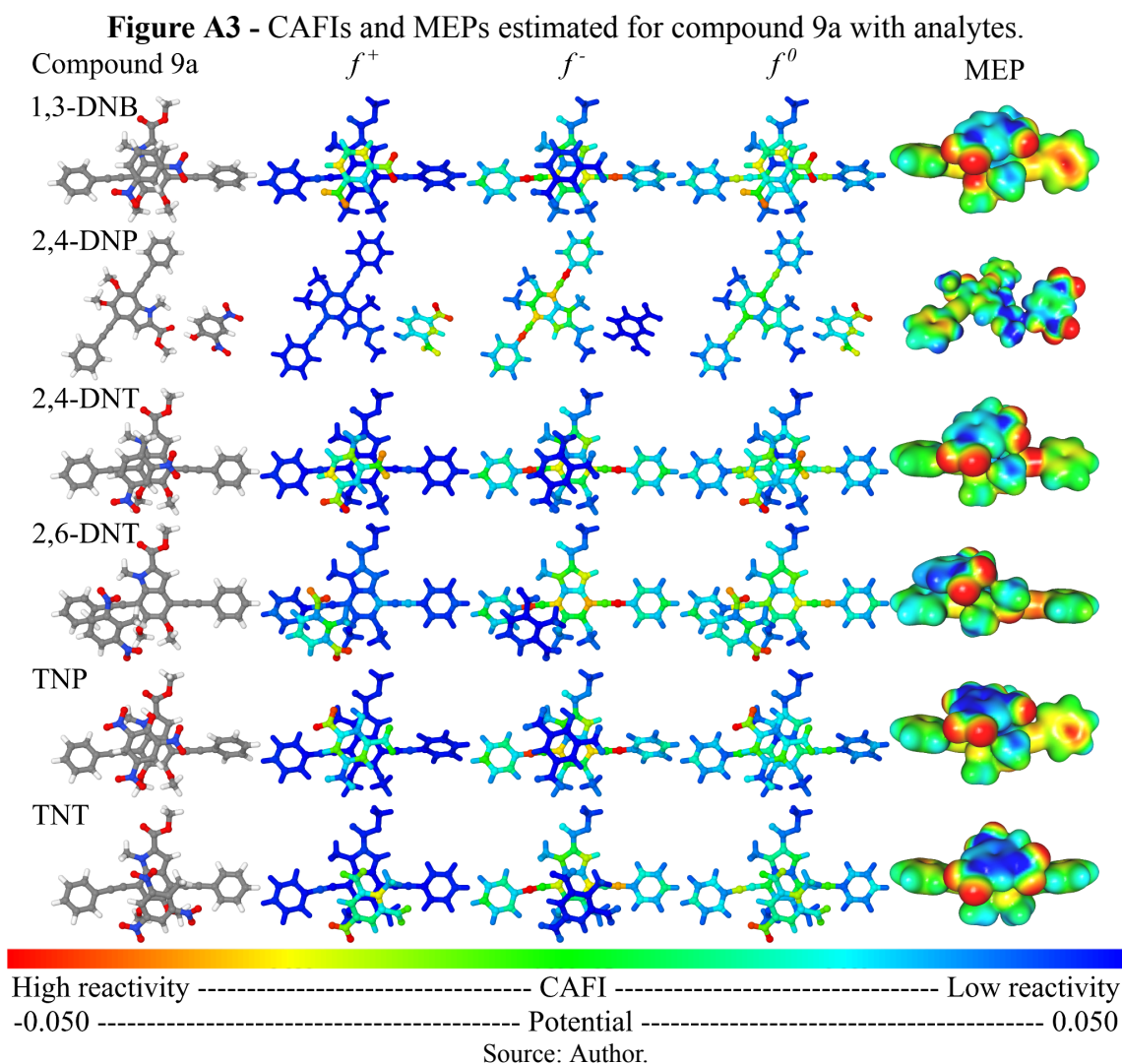
**Figure A2** - Comparison of total system energy of the systems obtained by the distinct adsorption approaches.



Source: Author.

### A3. Additional data for adsorbed systems (clusters obtained via CAFI)

Figures A3 and A4 show the CAFIs and MEPs of melanin-based compounds complexed with NACs.



Sites with higher CAFI values (red sites) represent regions that tend to interact with nucleophiles (electron acceptor sites) for  $f^+$ , electrophiles (electron donor sites) for  $f^-$  or free radicals (with no change in total number of electrons) for  $f^0$ . It is expected that the analytes will have higher  $f^+$  indices as the LUMO of the system tends to accept electrons and that the highest  $f^-$  indices will be found in the melanin compounds as the HOMO tends to donate electrons, supporting the data shown in Figure 2.4. The CAFI of adsorbed systems show which atoms should be involved in the charge transfer processes. In this sense, special attention must be paid to the triple bonds of melanin-based compounds and the oxygen atoms of nitro groups in NACs.

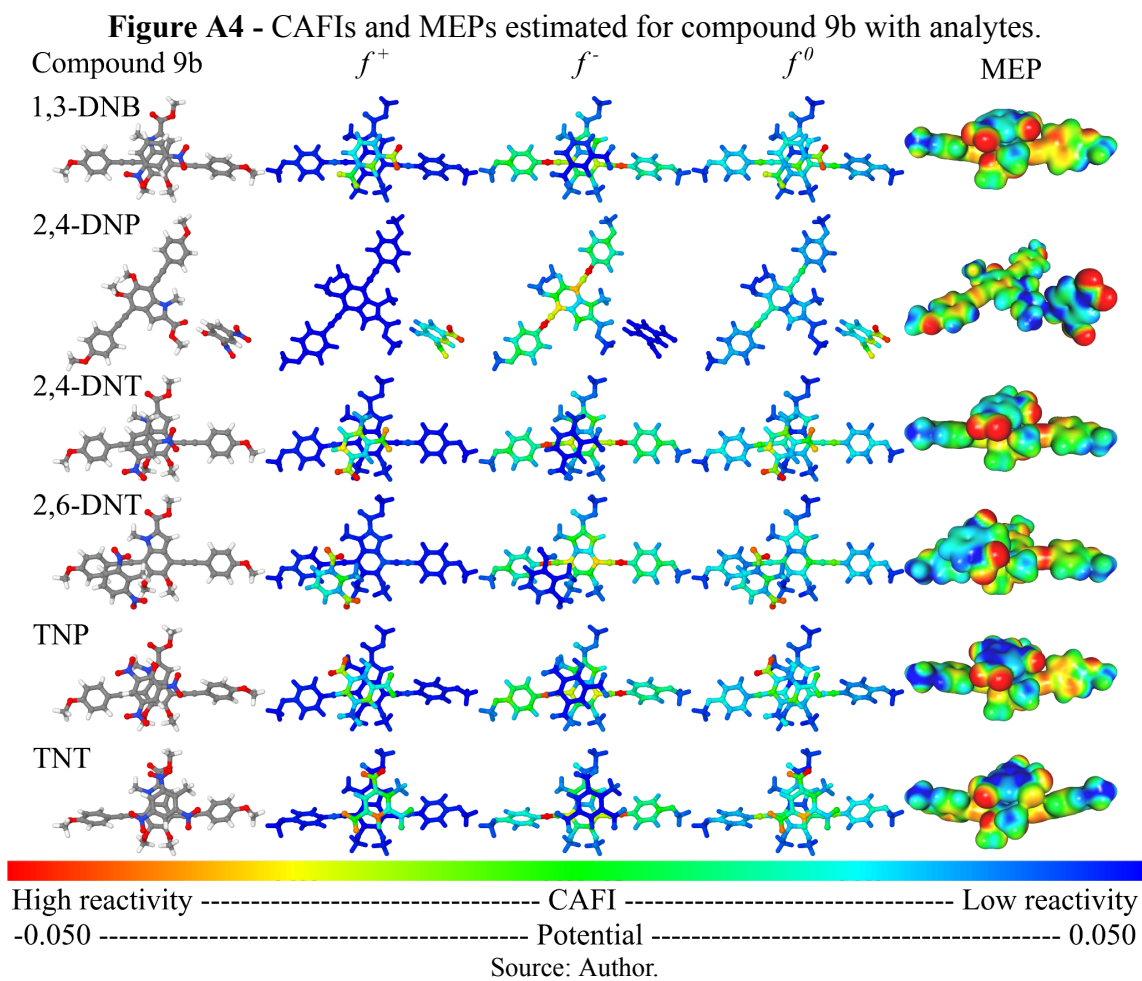
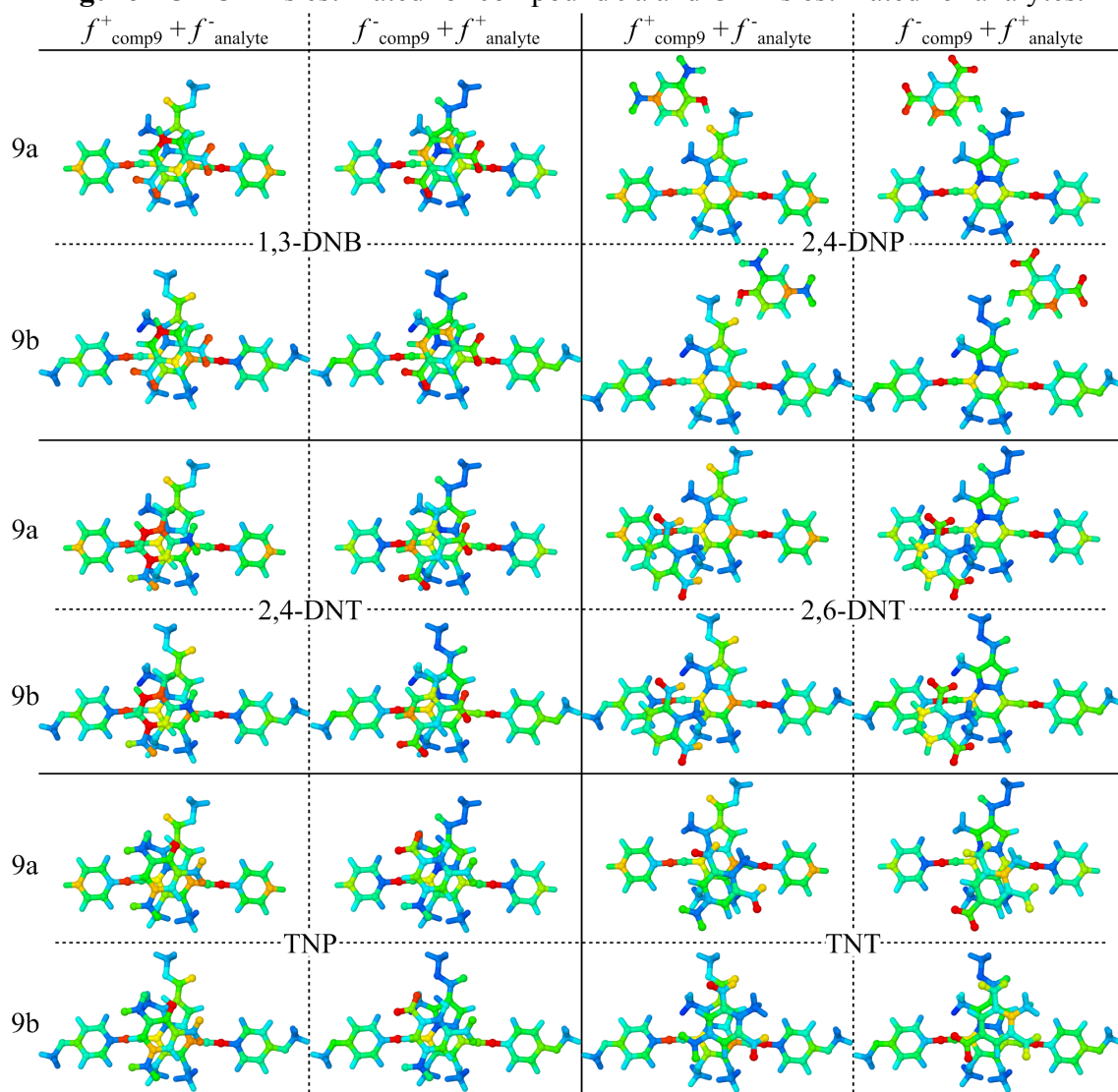


Figure A5 shows the CAFIs  $f^+$  and  $f^-$  of the melanin-based and NACs superimposed on the lowest clusters aiming to represent the proximity between the atoms with the highest reactivity indexes.

**Figure A5** - CAFIs estimated for compound 9a and CAFIs estimated for analytes.

Source: Author.

Note that effective interaction between oxygen atoms of NACs' nitro groups and triple bonds of the melanin-based compounds is observed for 1,3-DNB, TNP (for compounds 9a and 9b), and TNT (for compound 9b).

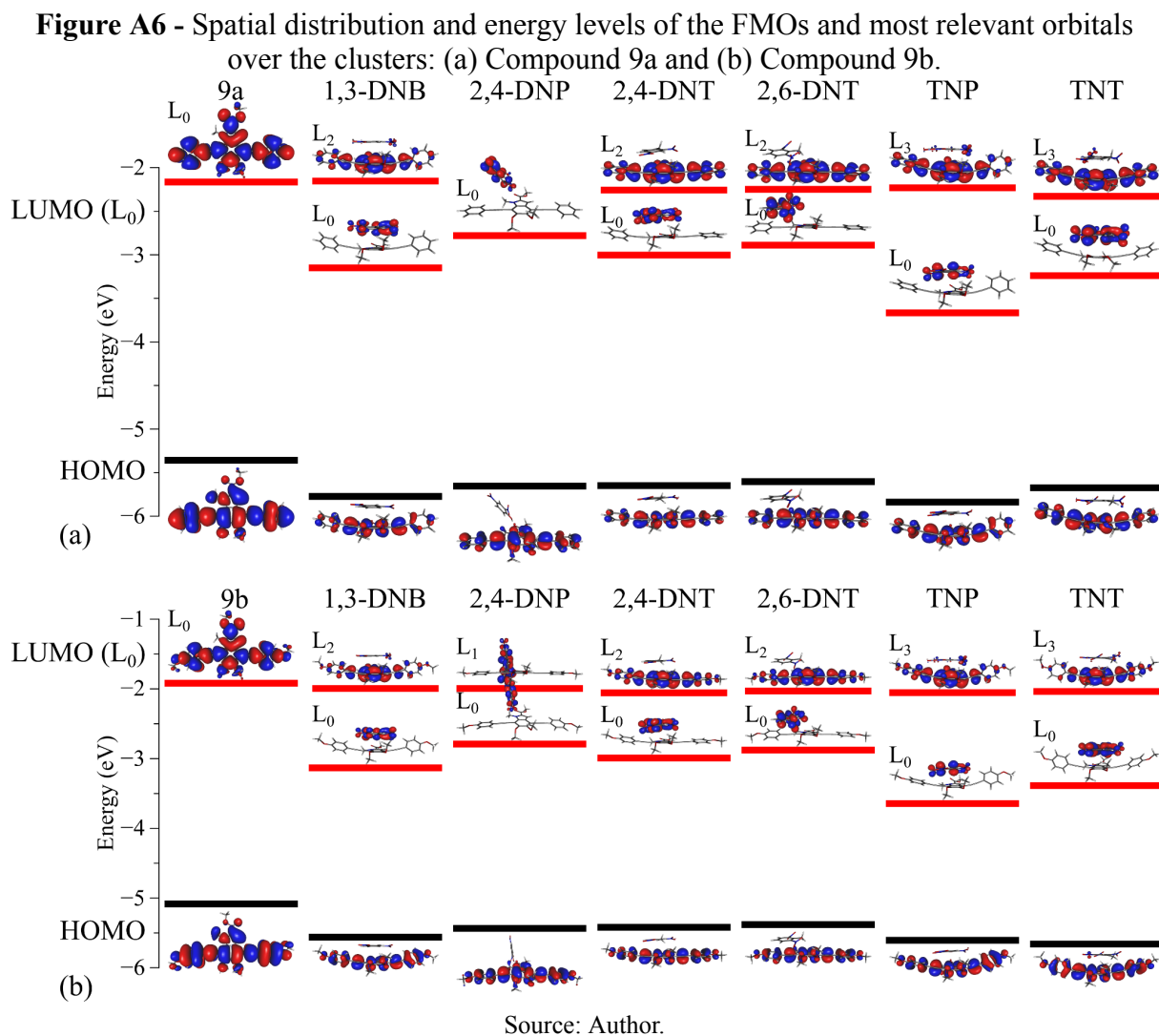
Table A1 presents the theoretical optical absorption spectra of compounds 9a and 9b, both in their isolated forms and after adsorption, (clusters obtained through the CAFI approach).

**Table A1.** Theoretical optical absorption spectra of compounds 9a and 9b isolated and adsorbed, clusters obtained via CAFI approach.

Compound	Analyte	$E_{\text{vert}}$ (eV)	$\lambda_{\text{max}}$ (nm)	$f_{\text{osc}}$	Main transit.	$\Delta E$ (eV)	$c_i^2 \times 100$
9a	isolated	2.9385	421.93	1.1064	<b>H</b> → <b>L</b>	3.19	49.2846
	1,3-DNB	3.0832	402.12	0.3962	H <sub>3</sub> → <b>L</b>	3.71	7.9180
					H <sub>4</sub> →L <sub>1</sub>	4.19	5.9952
					<b>H</b> →L <sub>2</sub>	3.43	33.3853
	2,4-DNP	2.8179	439.99	0.8466	<b>H</b> → <b>L</b>	2.87	48.8405
	2,4-DNT	2.9306	423.07	0.8587	<b>H</b> →L <sub>2</sub>	3.22	48.2039
	2,6-DNT	2.9077	426.4	0.9469	<b>H</b> →L <sub>2</sub>	3.19	48.2275
	TNP	3.0994	400.03	0.5881	H <sub>5</sub> → <b>L</b>	3.65	1.9822
					H <sub>2</sub> →L <sub>1</sub>	3.45	1.4156
					<b>H</b> →L <sub>3</sub>	3.44	43.0074
TNT	2.931	423.01	0.7137	H <sub>2</sub> → <b>L</b>	3.53	1.5982	
				<b>H</b> →L <sub>3</sub>	3.24	47.0102	
9b	isolated	2.9032	427.06	1.3066	<b>H</b> → <b>L</b>	3.17	49.3717
	1,3-DNB	2.9492	420.4	0.7161	<b>H</b> →L <sub>2</sub>	3.31	46.8609
	2,4-DNP	2.6948	460.09	0.8758	<b>H</b> →L <sub>1</sub>	2.98	48.5907
	2,4-DNT	2.8473	435.45	0.8179	H <sub>2</sub> → <b>L</b>	3.44	5.0127
					H <sub>1</sub> → <b>L</b>	3.25	8.3943
					<b>H</b> →L <sub>2</sub>	3.13	34.7204
	2,6-DNT	2.8469	435.5	0.8667	H <sub>1</sub> → <b>L</b>	3.31	9.6336
					<b>H</b> →L <sub>2</sub>	3.13	38.0430
	TNP	2.9776	416.39	0.6067	H <sub>3</sub> →L <sub>1</sub>	3.50	13.4557
					<b>H</b> →L <sub>3</sub>	3.32	33.2629
TNT	3.0475	406.84	0.6824	H <sub>3</sub> →L <sub>2</sub>	3.52	1.6672	
				H <sub>1</sub> →L <sub>2</sub>	3.14	1.0341	
				<b>H</b> →L <sub>3</sub>	3.41	45.0711	

Source: Author.

Figure A6 shows the spatial distribution of the frontier molecular orbitals and the most relevant orbitals (largest  $c_i^2 \times 100$ ) presented in Table A1, resulting from the optical absorption calculations made using TD-DFT.



Similar to Figures 2.8 and 2.9, Figure A6 demonstrates that  $LUMO_n$  (for  $n > 1$ ) are centered on the melanin-based structures instead of the analytes.

The recovery time,  $\tau$ , indicates the time required to completely desorb an analyte from the substrate surface. Ideally, it should range from a few milliseconds to minutes, indicating an effective anchoring property combined with a reasonable recovery capability. It can be estimated by Eq. A1:

$$\tau = \nu^{-1} \times e^{-\frac{E_{ads}}{k_b T}} \quad (A1)$$

$E_{ads}$  refers to the adsorption energy (as presented in Fig. 2.11),  $\nu$  denotes the attempt frequency ( $\sim 10^{12}$  s for visible light exposition),  $k_B$  represents the Boltzmann constant, and T represents the temperature. Table A2 shows the  $\tau$  (in seconds) estimated for TNP and TNT systems for different temperatures.

**Table A2** - Recovery time of compounds 9a and 9b for TNP and TNT.

Systems	$\tau$ (s)			
	300 K	400 K	500 K	650 K
9a+TNP	$4.20 \times 10^4$	2.93	$9.41 \times 10^{-3}$	$4.70 \times 10^{-5}$
9a+TNT	$4.41 \times 10^4$	3.04	$9.70 \times 10^{-3}$	$4.81 \times 10^{-5}$
9b+TNP	$1.04 \times 10^5$	5.78	$1.62 \times 10^{-2}$	$7.14 \times 10^{-5}$
9b+TNT	$1.93 \times 10^5$	9.21	$2.35 \times 10^{-2}$	$9.51 \times 10^{-5}$

Source: Author.

To investigate the selectivity of the compounds, additional adsorption studies were carried out for  $N_2$  and  $O_2$  (triplet state) using the same theoretical approach as NACs presented in Table A3.

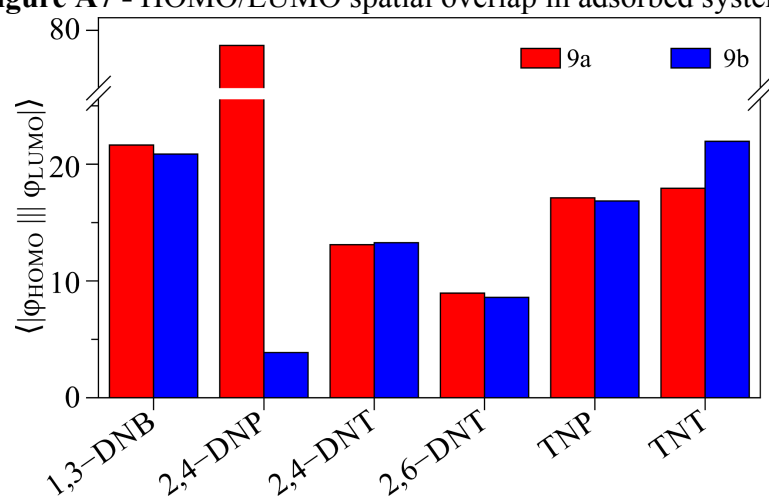
**Table A3.** Complexation energy of compounds 9a and 9b.

Compound	Adsorption energy (eV)							
	1,3-DNB	2,4-DNP	2,4-DNT	2,6-DNT	TNP	TNT	$N_2$	$O_2$
9a	-0.768	-0.629	-0.738	-0.669	-0.990	-0.991	-0.118	-0.102
9b	-0.784	-0.642	-0.755	-0.667	-1.013	-1.029	-0.119	-0.103

Source: Author.

The results revealed adsorption energies of -0.118 eV (-0.119 eV) and -0.102 (-0.103 eV) for  $N_2$  and  $O_2$  respectively, regarding compound 9a (9b), suggesting weak interactions for both the analytes. Note that the adsorption energy obtained for  $N_2$  ( $O_2$ ) was around 8x (10x) lower than for TNP and TNT.

Figure A7 presents a quantitative description of the compounds HOMO/LUMO overlap, estimated via the spatial overlap matrix elements  $\langle |\phi_{HOMO}| | | \phi_{LUMO}| \rangle$ <sup>97</sup>. Note that the frontier orbitals overlap are improved for 1,3-DNB, TNP, and TNT.

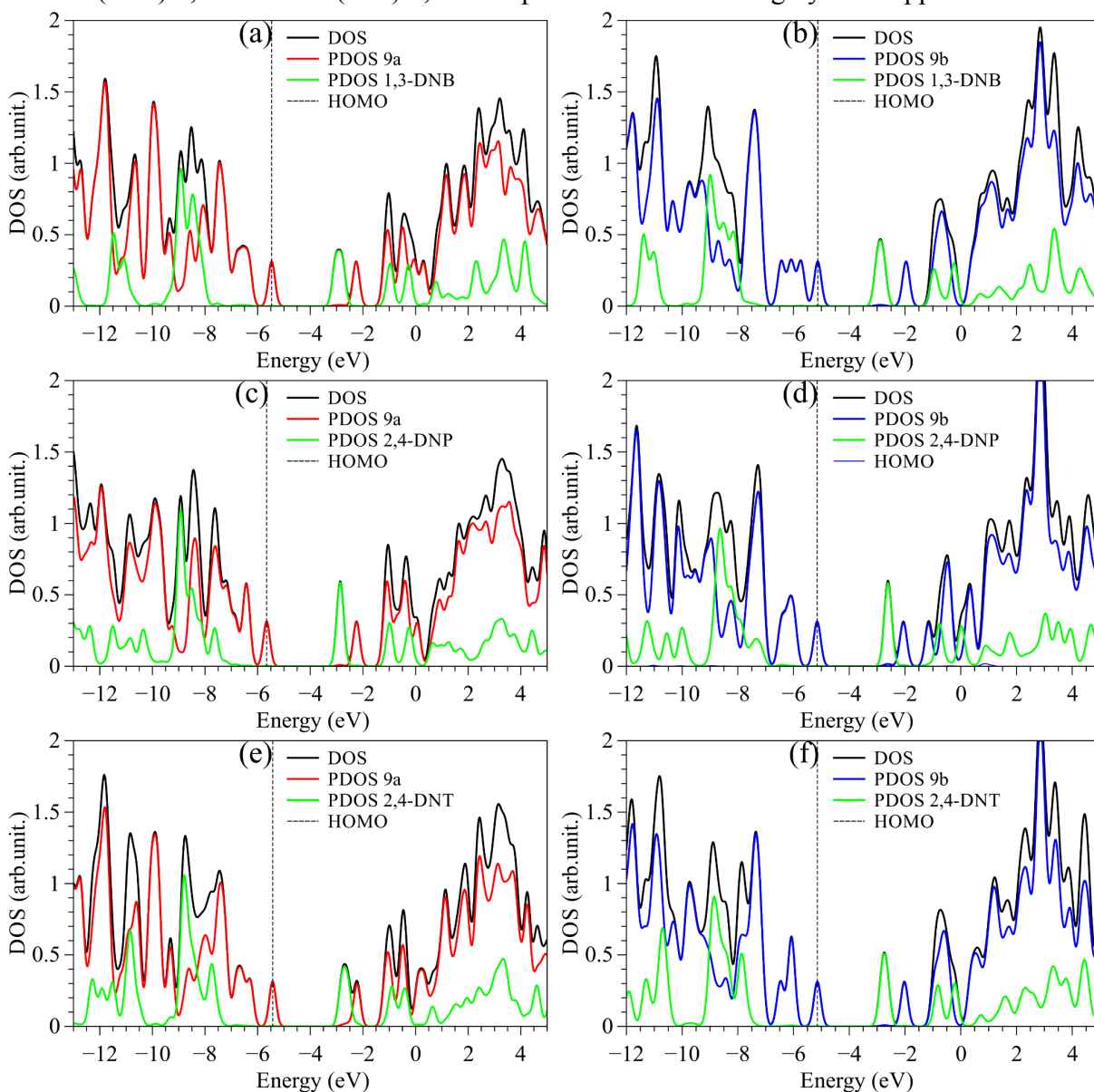
**Figure A7 - HOMO/LUMO spatial overlap in adsorbed systems.**

Source: Author.

#### A4. Results for clusters obtained via docking by aISS

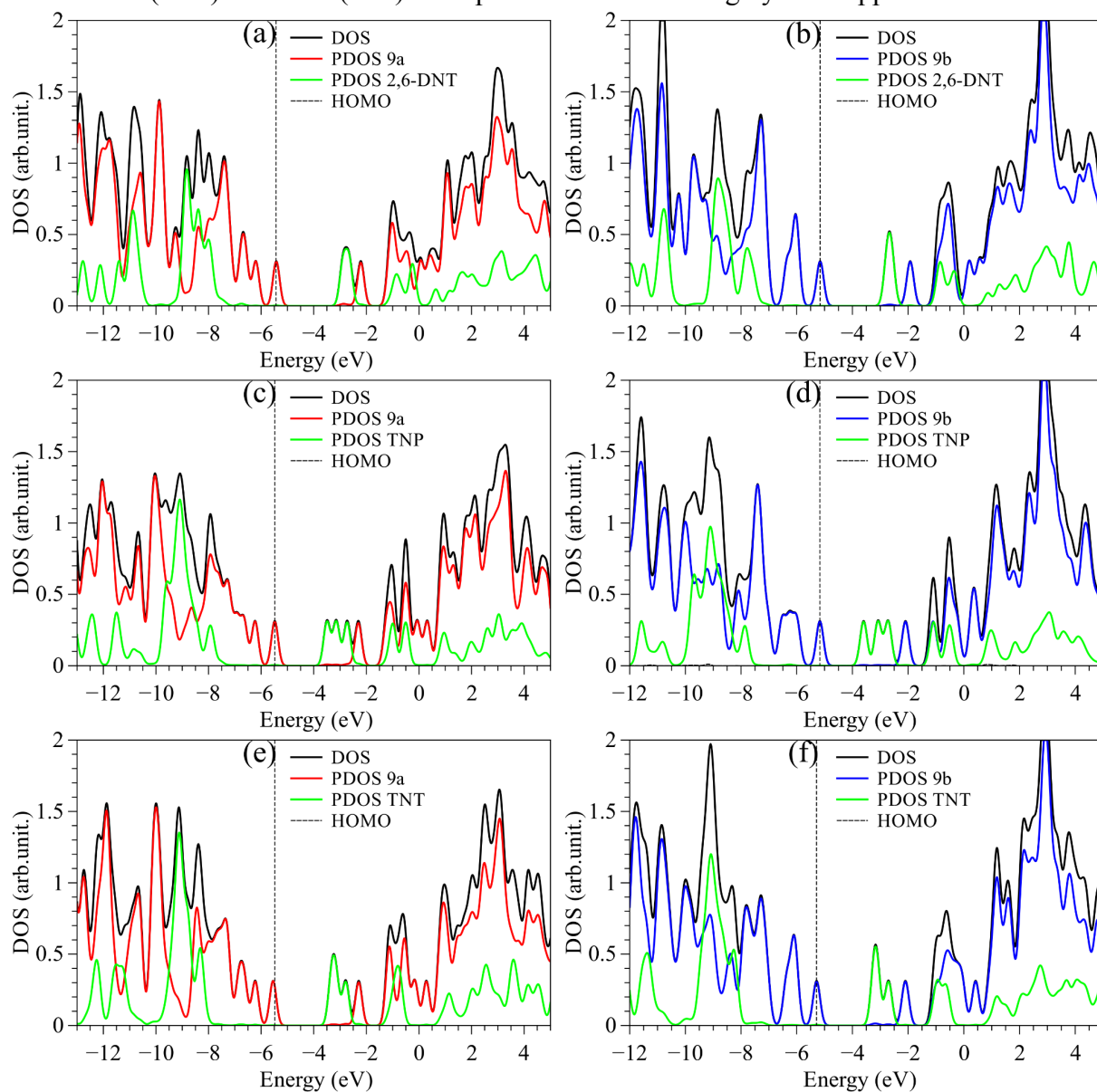
Figures A7 and A8 illustrate the partial and total density of states (PDOS and DOS) obtained for clusters coming from docking by aISS (see Fig. 2.7 and 2.8 of the main text for clusters obtained by CAFI).

**Figure A8** - DOS and PDOS of melanin-inspired compound (9a - 9b) with: (a - b) 1,3-DNB, (c - d) 2,4-DNP and (e - f) 2,4-DNT positioned via docking by aISS approach.



Source: Author.

**Figure A9** - DOS and PDOS of melanin-inspired compound (9a - 9b) with: (a - b) 2,6-DNT, (c - d) TNP and (e - f) TNT positioned via docking by aISS approach.



Source: Author.

It is possible to note that the HOMO of the systems is dominated by the melanin-based compounds while the LUMO is dominated by the NACs, leading to clusters with reduced electronic band gaps.

Figures A10 and A11 represent the (BSSE corrected) complexation energies between melanin substrates and analytes, and the interaction area of clusters obtained via docking by aISS approach.

**Figure A10** - Complexation energies between melanin-inspired compounds and NACs for clusters obtained via docking by aISS approach.

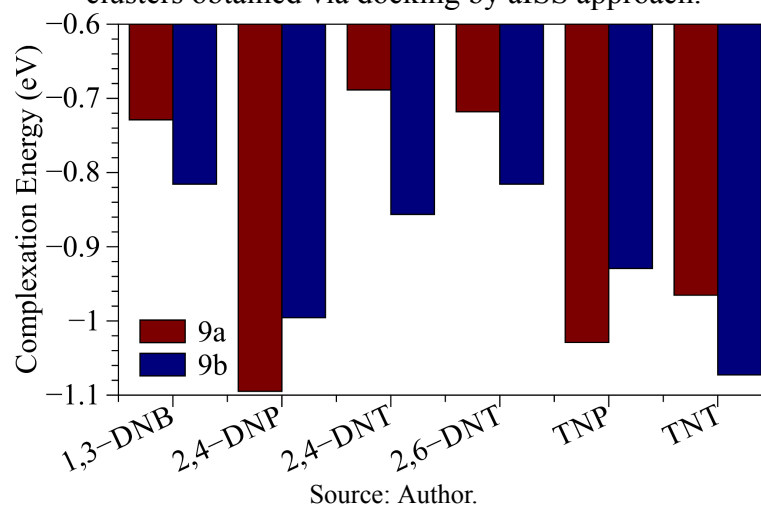
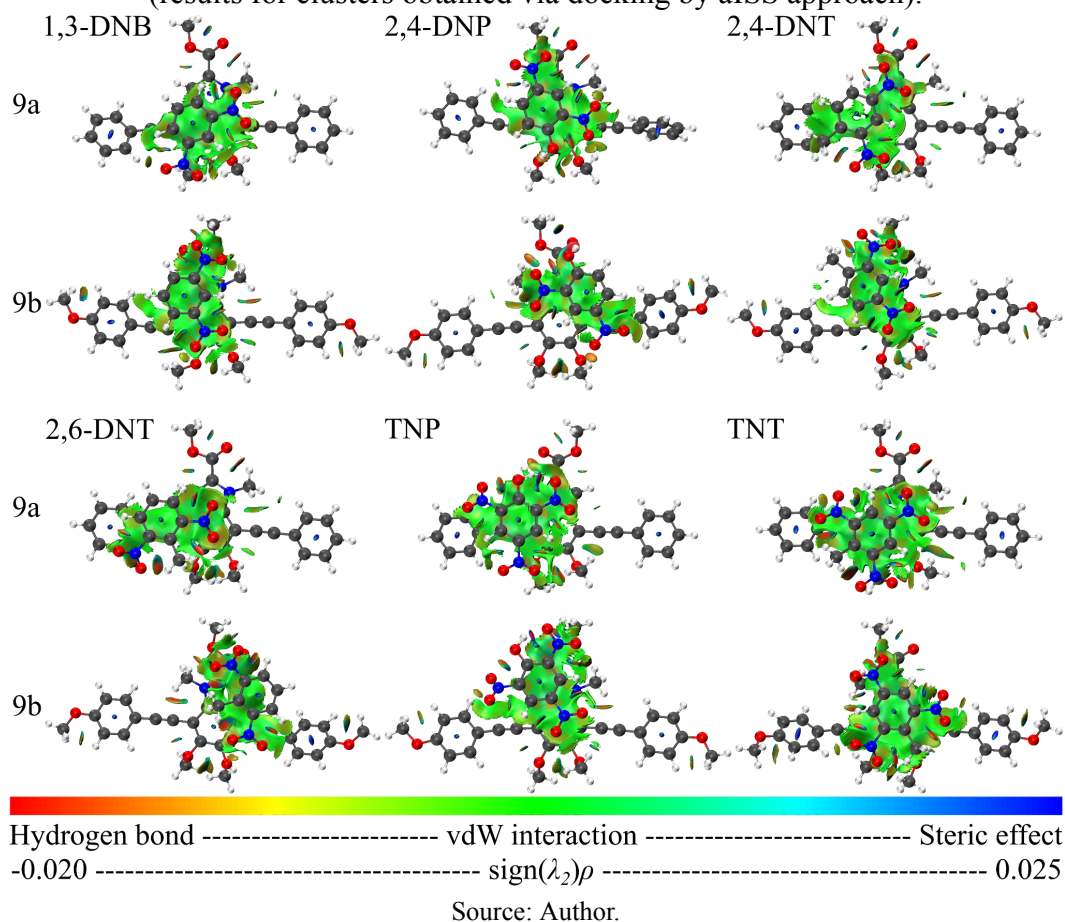


Figure A10 shows a significant increase in the complexation energy of the clusters based on 2,4-DNP analytes. As shown in Figure 2.10, the complexation energy for 1,3-DNB, 2,4-DNT, and 2,6-DNT compounds is lower than that of the trinitro compounds. With the exception of 2,4-DNT and TNP, compound 9b exhibits a higher complexation energy compared to compound 9a.

The higher complexation energies identified for clusters obtained via docking by aISS approach indicate the existence of strong analyte-substrate interactions. However, once these systems present higher total energies in relation to CAFI guided adsorption process, we can consider that such interactions lead to more expressive structural distortions of the systems, increasing the total energy of the clusters.

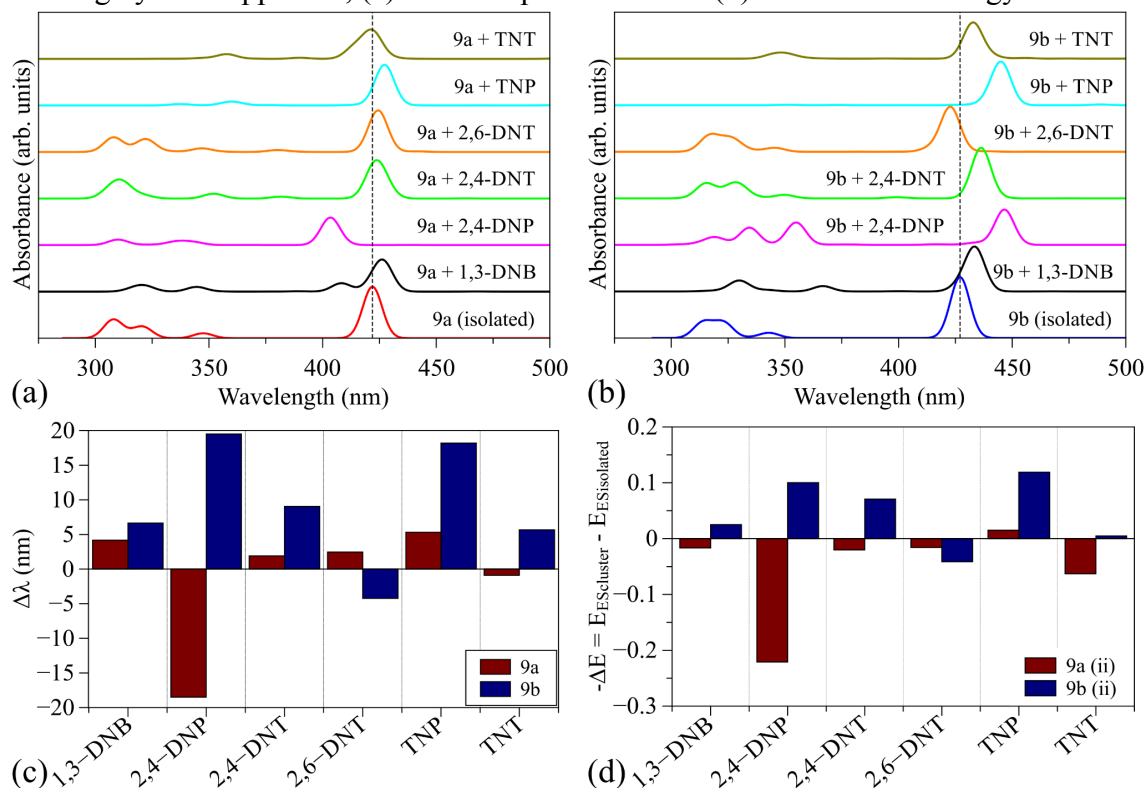
**Figure A11** - Analyte-melanin-based compound interactions: strength and interaction areas (results for clusters obtained via docking by aISS approach).



Note that the interactions of compound 9 with the analyte are predominantly van der Waals (vdW) interactions. Most systems exhibit interactions primarily occurring at the core of compound 9 and a portion of side groups and central rings. An exception is observed for the 9a+2,4-DNP cluster, where interactions occur with both side groups, resulting in a notable distortion of compound 9a and consequently a higher complexation energy. Except for the systems 9a-TNP, 9b-2,4-DNP, 9b-2,6-DNT, and 9b-TNT, in all the other systems the analyte final structure is aligned on the opposite side of the melanin-based compound compared to the manually assembled systems (CAFI guided adsorption).

Figure A12a-b depicts the absorption spectra of compounds 9a and 9b isolated and adsorbed with distinct NACs, as well as the main peak shift noticed for each substrate/analyte system. Figure A12c presents the numerical shift observed in Fig. A12a and A12b. Figure A12d shows the variation of energy of  $E_{\text{ES}}$  (Excited state energy) of the cluster in relation to the compound 9 isolated.

**Figure A12** - Theoretical optical absorption spectra of compounds 9a (a) and 9b (b) (gaussian curves with half width of 5 nm): isolated and adsorbed with NACs clusters obtained via docking by aISS approach, (c) the absorption shift and (d) Excited state energy variation.



Source: Author.

Note that, in general, the NACs adsorption leads to more significant changes on the main peak optical absorption of the compound 9b than 9a. Some compounds presented bathochromic shift (red shifted: 1,3-DNB; 2,4-DNT; and TNP) and anomalous (with no pattern: 2,4-DNP; 2,6-DNT and TNT) analytes. Significant deviations are noticed for 2,4-DNP ( $\Delta\lambda = -18.5$  nm with 9a and  $\Delta\lambda = +19.5$  nm with 9b) and TNP ( $\Delta\lambda = +18.18$  nm with 9b).

With the exception of 9a with 1,3-DNB, 2,4-DNT and 2,6-DNT clusters, a decrease in energy results in a red shift, while an increase in energy results in a blue shift.

Table A4 presents the theoretical optical absorption spectra of compounds 9a and 9b, both in their isolated forms and after adsorption, (clusters obtained via docking by aISS approach).

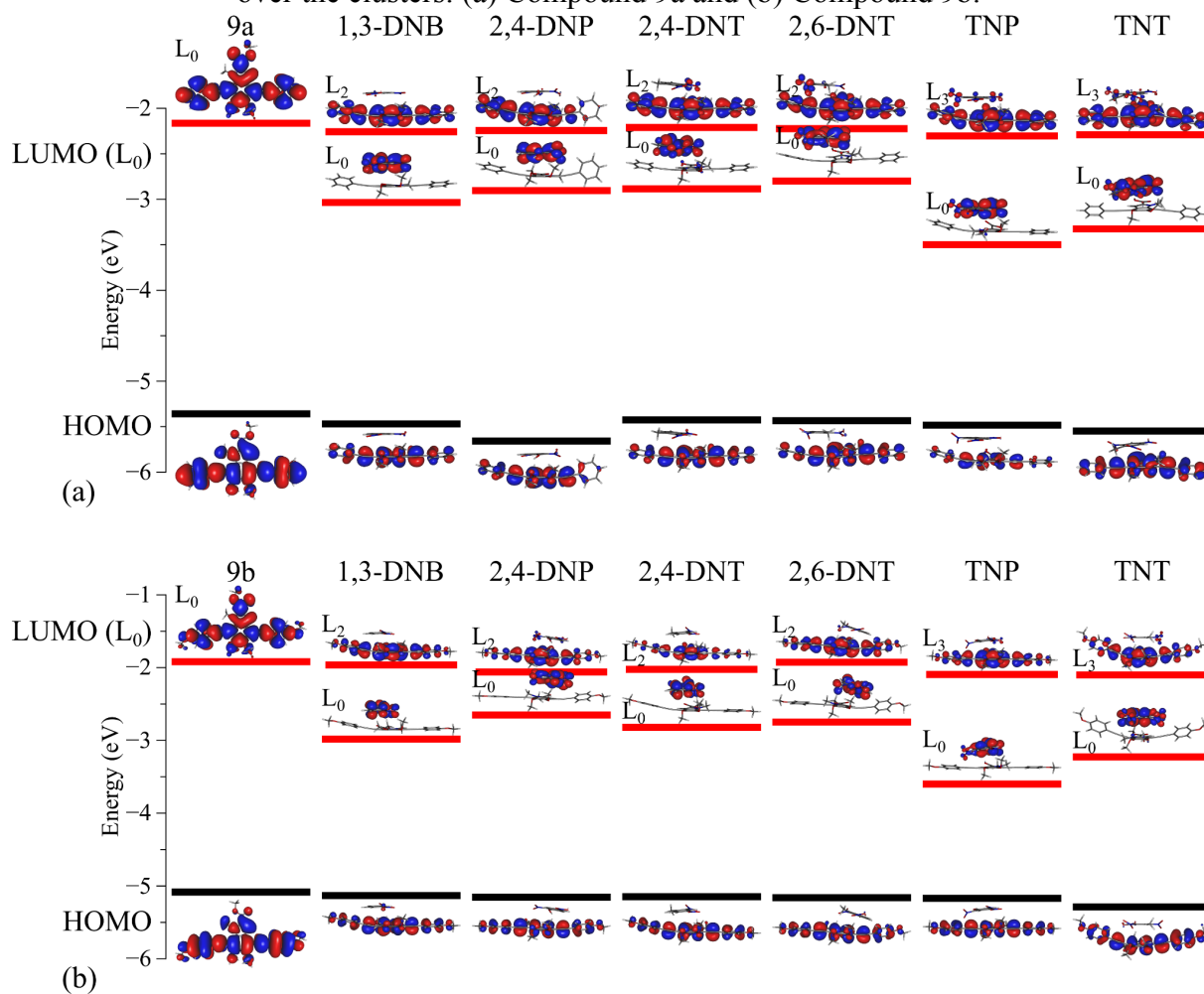
**Table A4** - Theoretical optical absorption spectra of compounds 9a and 9b adsorbed, clusters obtained via docking by aISS approach.

<b>Derivative</b>	$E_{\text{vert}}$ (eV)	$\lambda_{\text{max}}$ (nm)	$f_{\text{osc}}$	<b>Main transit.</b>	$\Delta E$ (eV)	$c_i^2 \times 100$
9a	2.9385	421.93	1.1064	<b>H→L</b>	3.19	49.2846
9a+1,3-DNB	2.9056	426.7	0.6088	<b>H<sub>2</sub>→L</b>	3.54	5.3991
				<b>H<sub>1</sub>→L<sub>1</sub></b>	3.55	4.8748
				<b>H→L<sub>2</sub></b>	3.21	38.8677
9a+2,4-DNP	3.0733	403.42	0.5911	<b>H→L<sub>2</sub></b>	3.45	47.7440
9a+2,4-DNT	2.9322	422.84	0.6539	<b>H<sub>1</sub>→L<sub>1</sub></b>	3.55	14.8071
				<b>H→L<sub>2</sub></b>	3.21	33.2272
9a+2,6-DNT	2.9215	424.39	0.8954	<b>H<sub>1</sub>→L</b>	3.48	1.1366
				<b>H→L<sub>2</sub></b>	3.21	47.4597
9a+TNP	2.9019	427.26	0.8716	<b>H→L<sub>3</sub></b>	3.18	48.1358
9a+TNT	2.9399	421.73	0.5192	<b>H<sub>3</sub>→L</b>	3.53	11.2091
				<b>H<sub>2</sub>→L<sub>1</sub></b>	3.49	4.4108
				<b>H→L<sub>3</sub></b>	3.26	32.0560
<b>Derivative</b>	$E_{\text{vert}}$ (eV)	$\lambda_{\text{max}}$ (nm)	$f_{\text{osc}}$	<b>Main transit.</b>	$\Delta E$ (eV)	$c_i^2 \times 100$
9b	2.9032	427.06	1.3066	<b>H→L</b>	3.17	49.3717
9b+1,3-DNB	2.8587	433.71	0.8956	<b>H<sub>3</sub>→L</b>	3.46	4.4808
				<b>H<sub>2</sub>→L<sub>1</sub></b>	3.30	3.0457
				<b>H→L<sub>2</sub></b>	3.17	41.4453
9b+2,4-DNP	2.7764	446.56	0.7578	<b>H→L<sub>2</sub></b>	3.09	47.2753
9b+2,4-DNT	2.8430	436.11	0.9535	<b>H<sub>2</sub>→L</b>	3.26	2.3437
				<b>H<sub>1</sub>→L</b>	3.25	3.4708
				<b>H→L<sub>2</sub></b>	3.12	42.5769
9b+2,6-DNT	2.9323	422.83	0.9597	<b>H<sub>2</sub>→L</b>	3.29	1.1922
				<b>H<sub>1</sub>→L<sub>1</sub></b>	3.43	1.2728
				<b>H→L<sub>2</sub></b>	3.24	45.6030
9b+TNP	2.7846	445.25	0.8910	<b>H<sub>1</sub>→L<sub>3</sub></b>	3.91	2.9801
				<b>H→L<sub>3</sub></b>	3.08	45.3225
9b+TNT	2.8652	432.73	0.7704	<b>H<sub>2</sub>→L<sub>2</sub></b>	3.42	3.9038
				<b>H→L<sub>3</sub></b>	3.19	43.8575

Source: Author.

Figure A13 shows the spatial distribution of the frontier molecular orbitals and the most relevant orbitals (largest  $c_i^2 \times 100$ ) presented in Table A4, resulting from the optical absorption calculations made using TD-DFT.

**Figure A13** - Spatial distribution and energy levels of the FMOs and most relevant orbitals over the clusters: (a) Compound 9a and (b) Compound 9b.



Source: Author.

Similar to Figures A8 and A9, Figure A13 demonstrates that  $LUMO_n$  (for  $n > 1$ ) are centered on the melanin-based structures instead of the analytes.

## CHAPTER III – DFT-Guided Design of Melanin-Inspired Materials for High-Performance Organic Solar Cells<sup>2</sup>

### 3.1 Abstract

Organic solar cells (OSCs) have rapidly emerged as a promising alternative to traditional photovoltaic technologies, such as crystalline silicon and perovskites, due to their potential for low-cost, lightweight, and flexible applications. The development of efficient, non-toxic, and earth-abundant materials has motivated the transition from fullerene-based acceptors to non-fullerene counterparts. While current non-fullerene acceptors offer improved spectral absorption, they still present limitations in terms of absorption bandwidth and exciton dissociation efficiency, which constrain overall device performance. In this work, we designed and computationally evaluated a series of donor and acceptor molecules based on Y6 derivatives and eumelanin-inspired motifs. Specifically, we investigated the effect of incorporating hydroxyindole-based end groups ( $EG_{\text{mel}}$ ) into the  $Y6_{\text{core}}$  structure using density functional theory (DFT). Our results demonstrate that these  $EG_{\text{mel}}$  groups extend the optical absorption and enhance electron-accepting capabilities. Furthermore, we assessed a set of eumelanin-like oligomers as potential donor materials, which showed open-circuit voltage predictions comparable to benchmark donors such as PM6 and D18. These findings underscore the potential of bio-inspired modifications, such as hydroxyindole end groups and indolic donor cores, to improve the performance and sustainability of next-generation organic photovoltaic materials.

**Keywords:** Organic Solar Cells, Melanin-Inspired compounds, Density Functional Theory, Non-Fullerene Acceptors.

---

<sup>2</sup> Note: Parts of this chapter were previously published as:

Cachaneski-Lopes, J. P.; Alves, G. G. B.; Bégué, D.; Batagin-Neto, A. DFT-guided design of melanin-inspired materials for high-performance organic solar cells. *Computational and Theoretical Chemistry*, 1255, 115580 (2026).

The content was restructured and expanded for incorporation into this thesis.

## 3.2 Introduction

In recent years, considerable efforts have been devoted to the development of novel and more efficient solar cell technologies. In this context, the use of organic solar cells (OSCs) has achieved great prominence<sup>98–103</sup>. Over time, various strategies have been implemented to improve their performance, leading to PCE values reaching approximately 20%<sup>11,98</sup>. A key breakthrough was the incorporation of donor-acceptor (D-A) material blends in the active layer, which gave rise to bulk heterojunction organic solar cells (BHJOSCs)<sup>104</sup>.

Early BHJOSCs employed wide-bandgap polymers as donors and fullerene-based acceptors<sup>105</sup>, but their performance was hindered by poor light absorption and limited tunability<sup>11</sup>. To overcome these drawbacks, small-molecule acceptors (SMAs) with narrow band gaps were introduced as alternatives to fullerene derivatives. Due to their anisotropic and non-spherical structures, SMAs require precise donor matching to maximize device performance<sup>106</sup>.

SMAs have undergone significant design improvements to achieve higher PCEs, leading to the development of A-D-A type SMAs<sup>106</sup>, which consist of blocks with distinct donor (D) and acceptor (A) properties. The search for optimized structures has been gradual, involving chemical modifications, such as the addition of alkyl side chains, and alterations to the core block A/D nature. For instance, Zou et al. advanced the typical A-D-A structure by introducing an A-DA'D-A design, where A' represents an electron-deficient acceptor subunit incorporated into the traditional donor core<sup>106</sup>. More recent developments in SMA design stem from the work of Feng et al., that used 2-(3-oxo-2,3-dihydroinden-1-ylidene) as A units at the edge of the dithieno[3,2-b]pyrrolobenzotriazole (BZTP) core, leading to the non-fullerene acceptor (NFA) BZIC<sup>107</sup>.

Key progress in NFA optimization came with benzothiadiazole-core-based structures, exemplified by the Y-series and BZTP-series<sup>14,106,107</sup>. The Y-series comprises a family of similar NFAs, differentiated by minor modifications in side chains<sup>108</sup>, main cores<sup>108,109</sup>, and/or end-groups (EG)<sup>109</sup>. In particular, end groups (EG) can significantly affect a broad range of critical properties, such as charge carrier mobility, dimer interactions, molecular stacking, crystallinity, quadrupole moments, frontier orbital energies, reorganization energies, and light absorption spectra<sup>109–111</sup>.

Since the development of ITIC, most widely studied NFA materials have employed similar EGs, typically derived from 2-(3-oxo-2,3-dihydroinden-1-ylidene)malononitrile (INCN). Modifications to this group often involve the introduction of different functional

groups or ring substitutions (such as the incorporation of a thiophene ring in BTTPC)<sup>109</sup>. The use of INCN-based EGs were the key factor for promoting efficient  $\pi$ - $\pi$  stacking, leading to improved films<sup>108,109</sup>. Their strong electron-withdrawing character also broadens the optical absorption and reduces bandgaps<sup>13,109,112</sup>. Recent strategies employing substitutions and use of asymmetric EGs have opened new pathways for enhancing the photovoltaic performance of NFAs, but deeper exploration is still required to achieve fully optimized and efficient systems<sup>110,113–115</sup>.

Among the potential EGs to consider, indole quinone-based systems stand out as promising candidates. These structures are typical building blocks of melanins, complex structural pigments found in living organisms<sup>116,117</sup>. Incorporating these compounds as EGs could offer significant benefits, given their stability and ability to support both ionic and electronic transport<sup>118</sup>. Moreover, these compounds share structural similarities with commonly used EGs, which may facilitate their integration into traditional NFAs<sup>119,120</sup>.

In this study, we evaluate the impact of incorporating bioinspired eumelanin-based and modified traditional EG (named EG<sub>mel</sub>-R and EG-R, respectively) into the typical Y6 core (Y6<sub>core</sub>). The acceptor and donor capabilities, local reactivity, optoelectronic properties, and other properties were assessed through electronic structure calculations using density functional theory (DFT). Performance parameters were analyzed by considering well-known donor structures reported for Y6, namely PM6 and D18. Additionally, melanin-inspired oligomeric structures (MIOs), reported by Selvaraju et al.<sup>7</sup>, were evaluated as potential donors. These molecules, derived from renewable feedstocks such as vanillin, are accessible via efficient synthetic routes and are compatible with well-established cross-coupling methodologies, supporting their practical use in organic electronics<sup>7,48,121</sup>. MIOs incorporate C $\equiv$ C triple bonds within their  $\pi$ -conjugated backbones, promoting molecular planarity, enhancing charge-carrier mobility, and facilitating frontier orbital delocalization<sup>7,50,51</sup>. These alkynyl units also contribute to vibrational modes relevant to electronic coupling, while supporting efficient intramolecular charge separation<sup>49</sup>. Additionally, electron-donating methoxy groups further modulate the optoelectronic properties of the material by increasing electron density and preserving planarity<sup>52,53</sup>.

Our findings highlight the potential of eumelanin-inspired structures as EGs of non-fullerene acceptors (NFAs) and donors (MIOs). By incorporating bio-derived EG<sub>mel</sub> derivatives onto the Y6<sub>core</sub>, we demonstrate a broad tunability of electronic properties, including enhanced light absorption and favorable frontier molecular orbital (FMO) alignments, key factors for efficient exciton dissociation. Functionalization of the EG-R<sub>n</sub> and

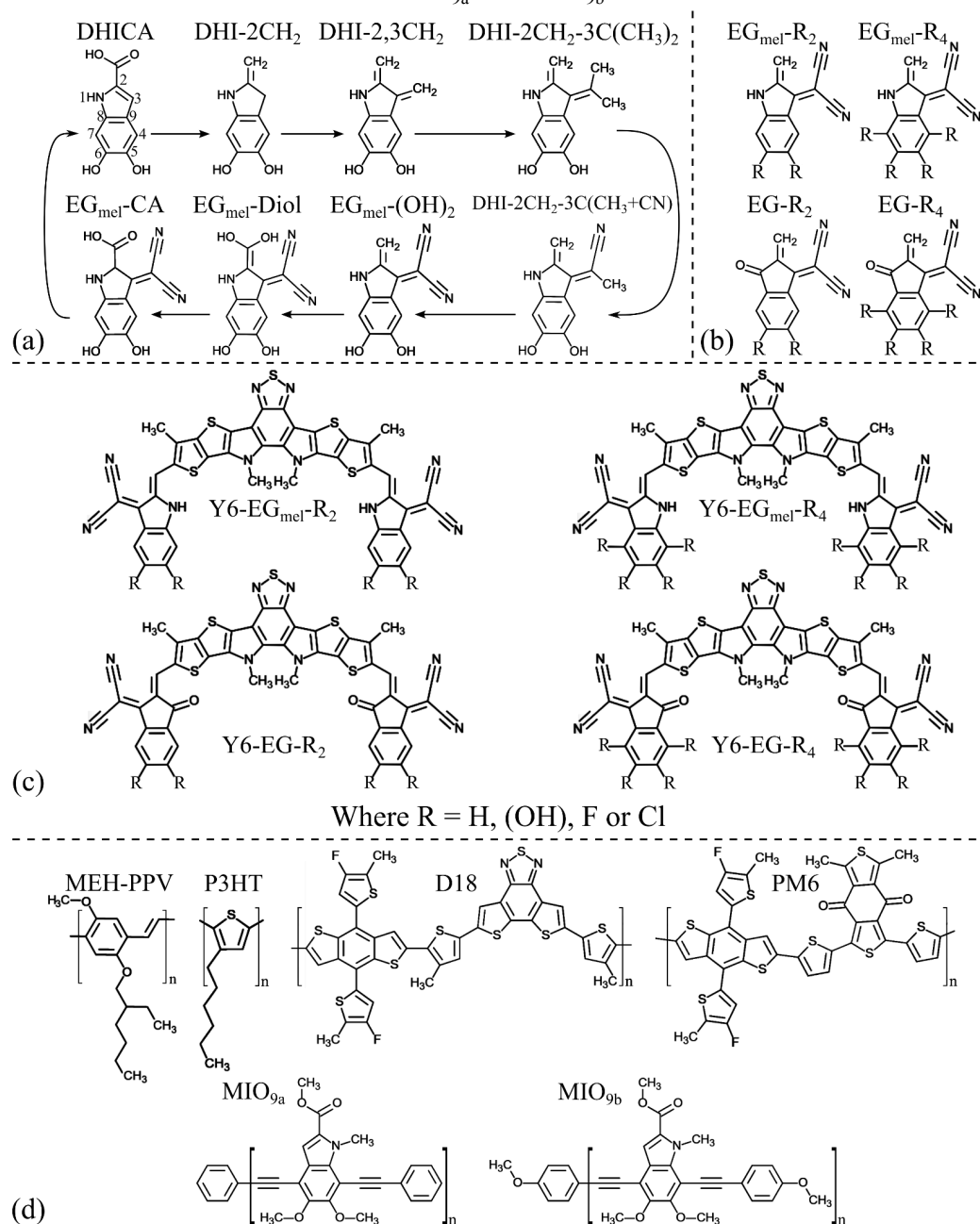
$EG_{mel}\text{-}R_n$  structures significantly influences the energy level alignment between donor and acceptor materials, as well as their electron-donating or -accepting capabilities. Certain donor–acceptor pairs, such as  $(MIO_{9b})_m\text{:}Y6\text{-}EG_{mel}\text{-}H$ ,  $(MIO_{9b})_m\text{:}Y6\text{-}EG\text{-}(OH)_4$ , and  $(MIO_{9b})_m\text{:}EG_{mel}\text{-}Y6\text{-}EG\text{-}(OH)_2$ , also exhibited promising properties, positioning  $MIO_{9b}$ -based systems as interesting donor candidates.

### 3.3 Material and Methods

#### 3.3.1 Material

Figure 3.1a summarizes the chemical structure of the distinct  $EG_{mel}$  considered in the present study. DHICA (5,6-dihydroxy-1*H*-indole-2-carboxylic acid) represents one of the most common building block of natural eumelanins; the other compounds: DHI-2CH<sub>2</sub> (2-methylene indoline-5,6-diol), DHI-2,3CH<sub>2</sub> (2,3-dimethylene indoline-5,6-diol), DHI-2CH<sub>2</sub>-3C(CH<sub>3</sub>)<sub>2</sub> (2-methylene-3-(propan-2-ylidene)indoline-5,6-diol), DHI-2CH<sub>2</sub>-3C(CH<sub>3</sub>+CN) ((*Z*)-2-(5,6-dihydroxy-2-methyleneindolin-3-ylidene)propanenitrile),  $EG_{mel}\text{-}(OH)_2$  (2-(5,6-dihydroxy-2-methyleneindolin-3-ylidene)malononitrile),  $EG_{mel}\text{-}Diol$  (2-(2-(dihydroxy-methylene)-5,6-dihydroxyindolin-3-ylidene)malononitrile),  $EG_{mel}\text{-}CA$  (3-(dicyanomethylene)-5,6-dihydroxyindoline-2-carboxylic acid) define DHICA modified structures, designed to resemble  $EG\text{-}F_2$  (2-(5,6-difluoro-2-methylene-3-oxo-2,3-dihydro-1*H*-inden-1-ylidene)-malononitrile), the traditional EG of Y6. All these intermediate structures were analyzed to investigate the effect of chemical modifications on the structure of DHICA, ultimately leading to the formation of the  $EG_{mel}\text{-}(OH)_2$  (our proposed melanin-based EG); the effect of COOH incorporation on modified structures was also evaluated for completeness. Figure 3.1b illustrates di- and tetra-substituted  $EG_{mel}$  and EG, while Figure 3.1c presents the overall structure of Y6 derivatives. Figure 1d shows the chemical structure of polymer donors considered for performance evaluation: MEH-PPV, P3HT, D18, and PM6. Melanin-based oligomeric compounds  $MIO_{9a}$  (methyl5,6-dimethoxy-1-methyl-4,7-bis(phenylethynyl)-1*H*-indole-2-carboxylate) and  $MIO_{9b}$  (methyl5,6-dimethoxy-4,7-bis((4-methoxyphenyl)ethynyl)-1-methyl-1*H*-indole-2-carboxylate) <sup>7</sup> were considered to investigate their potential applications as electron donors.

**Figure 3.1** - (a) Typical basic unit of the DHICA and modifications up to the EG<sub>mel</sub>-(OH)<sub>2</sub>; (b) Side groups compounds: EG<sub>mel</sub> and EG; (c) NF acceptors: Y6 with distinct EG<sub>mel</sub> and EG, and (d) Typical polymer donors: MEH-PPV, P3HT, D18, PM6 and melanin-inspired compounds MIO<sub>9a</sub> and MIO<sub>9b</sub>.



Source: Author.

Aiming to conduct comparative analyses, typical fullerene acceptors (PCBM and ICBA) were also evaluated.

### 3.3.2 Methods

All the structures were designed with the aid of the Gaussview computational package<sup>56</sup>. The 3D geometries were then optimized in the framework of the density functional theory

(DFT) using B3LYP<sup>58,59,122</sup> exchange-correlation (XC) functional and 6-311G(d,p) basis set on all the atoms. Polymeric systems were evaluated considering oligomeric structures in a DFT/B3LYP/6-311G(d,p) approach for MIO<sub>9a</sub>, MIO<sub>9b</sub>, MEH-PPV and P3HT. The PM6 and D18 oligomers were optimized via a simplified DFT/B3LYP/6-31G(d) approach, due to the higher computational costs associated with these structures. Nevertheless, larger basis sets (6-311G(d, p)) were employed to evaluate their optoelectronic properties for comparison.

The local reactivities were evaluated via the condensed-to-atoms Fukui indexes (CAFIs)<sup>60,123</sup> analysis and investigation of the Kohn-Sham (KS) frontier molecular orbitals (FMO) spatial distribution (considering the highest occupied and the lowest unoccupied KS orbitals, HOMO and LUMO, respectively).

The donation and acceptance indexes ( $R_D/R_A$ ) were estimated from the analysis of the relative electron accepting and electron donating powers as reported by in refs<sup>67,68</sup>.

The relative alignments between the FMOs were also evaluated to investigate the potential applicability of distinct D:A pairs. The HOMO and LUMO energies ( $E_{\text{HOMO}}$  and  $E_{\text{LUMO}}$ ) were estimated via KS eigenvalues. The electronic gaps were obtained from  $E_{\text{gap}} = E_{\text{LUMO}} - E_{\text{HOMO}}$ .

The solar absorption yield was estimated by integrating the product of solar irradiance and the Gaussian-convoluted theoretical optical absorption spectra of the molecules (Eq. 3.1 and 3.2), from the ultraviolet (UV) to the infrared (IR) (e.g. from ~200 nm to ~3500 nm, see Fig. B18):

$$\int_{UV}^{IR} [I(\lambda) \times \varepsilon(\lambda)] d\lambda \quad (3.1)$$

$$\varepsilon(\lambda) = \sum_{i=1}^n \varepsilon_i(\lambda) = \sum_{i=1}^n \left[ \frac{\sqrt{\pi} \cdot e^2 \cdot N}{1000 \cdot \ln(10) \cdot c^2 \cdot m_e} \cdot \frac{f_i}{(10^7 \cdot \sigma^{-1})} \cdot e^{-\frac{(\lambda-\lambda_i)^2}{\sigma^2}} \right] \quad (3.2)$$

where  $I(\lambda)$  represents the solar irradiance as a function of  $\lambda$ ,  $\varepsilon_i(\lambda)$  denotes the absorption of interest with oscillation strength  $f_i$  at each wavelength  $\lambda_i$ ,  $\lambda$  and  $\lambda_i$  are the wavelengths corresponding to solar irradiance and excited state of interest, respectively.  $e$ ,  $N$ ,  $c$ ,  $m_e$  represents the fundamental electron charge, Avogadro's number, speed of light, and electron mass.  $\sigma = 0.4 \text{ eV} = 1/3099.6 \text{ nm}^{-1}$  represents the standard deviation of the Gaussian<sup>124</sup>.

The optical properties of the compounds were evaluated via a time dependent DFT (TD-DFT) approach, employing the B3LYP/6-311G(d,p) approach. The optical gaps ( $E_{\text{opt}}$ )

were estimated via vertical transitions involving the first singlet excited states of each system ( $E_{\text{vert}}$ ). Exciton binding energies were estimated by  $E_X = E_{\text{gap}} - E_{\text{opt}}$ <sup>125</sup>. Reorganization energies for electrons ( $\Lambda_e$ ) and holes ( $\Lambda_h$ ) were calculated via Eqs. 3 and 4, considering only the internal reorganization energies<sup>126–128</sup>:

$$\Lambda_h = [E_T(v_{N-1}, N) - ET(v_N, N)] + [E_T(v_N, N-1) - E_T(v_{N-1}, N-1)] \quad (3)$$

$$\Lambda_e = [E_T(v_{N+1}, N) - ET(v_N, N)] + [E_T(v_N, N+1) - E_T(v_{N+1}, N+1)] \quad (4)$$

where  $E_T(v_{N+k}, N+j)$  represents the total energy coming from single-point calculations for the species  $M^j$  (i.e.,  $M$  with  $N+j$  electrons) with the structure previously obtained from the optimization of the  $M^k$  species (i.e.,  $M$  with  $N+k$  electrons)<sup>128,129</sup>. Materials with low values of  $\Lambda_e$  ( $\Lambda_h$ ) facilitate the transport of electrons (holes). All the calculations were conducted with the aid of Gaussian 16 computational package<sup>69</sup>.

Additional performance parameters were also evaluated for the distinct D:A pairs, which are better illustrated in Figure B1<sup>14,129–131</sup>. The  $\Delta E_{\text{LL}}$  represents the difference between the LUMO levels of the donor ( $\text{LUMO}_D$ ) and the acceptor ( $\text{LUMO}_A$ ) while  $\Delta E_{\text{HH}}$  represents the difference between the HOMO levels of these compounds. Such parameters allow estimating the probabilities of exciton dissociation and recombination, respectively<sup>132,133</sup>, efficient devices are supposed to present  $\Delta E_{\text{LL}}$  and  $\Delta E_{\text{HH}}$  higher than the exciton binding energies ( $E_X$ , typically 0.3 eV)<sup>134</sup>.  $E_{\text{gap}}$  defines the fundamental electronic gap of the donor material, and is associated with its optical absorption capacity. Low  $E_{\text{gap}}$  values result in more efficient donor absorption, however, very small values may significantly reduce other relevant parameters such as:  $\Delta E_{\text{HDLA}}$  (associated with the open circuit voltage of the devices (Eq. 5)),  $\Delta E_{\text{AN-D}}$  and  $\Delta E_{\text{A-CA}}$  (associated with the differences between FMO levels of the donor/acceptor and the work function of anode and cathode).

$$e \cdot V_{\text{OC}} = (|E_{\text{HOMO,D}} - E_{\text{LUMO,A}}| - E_X) \quad (5)$$

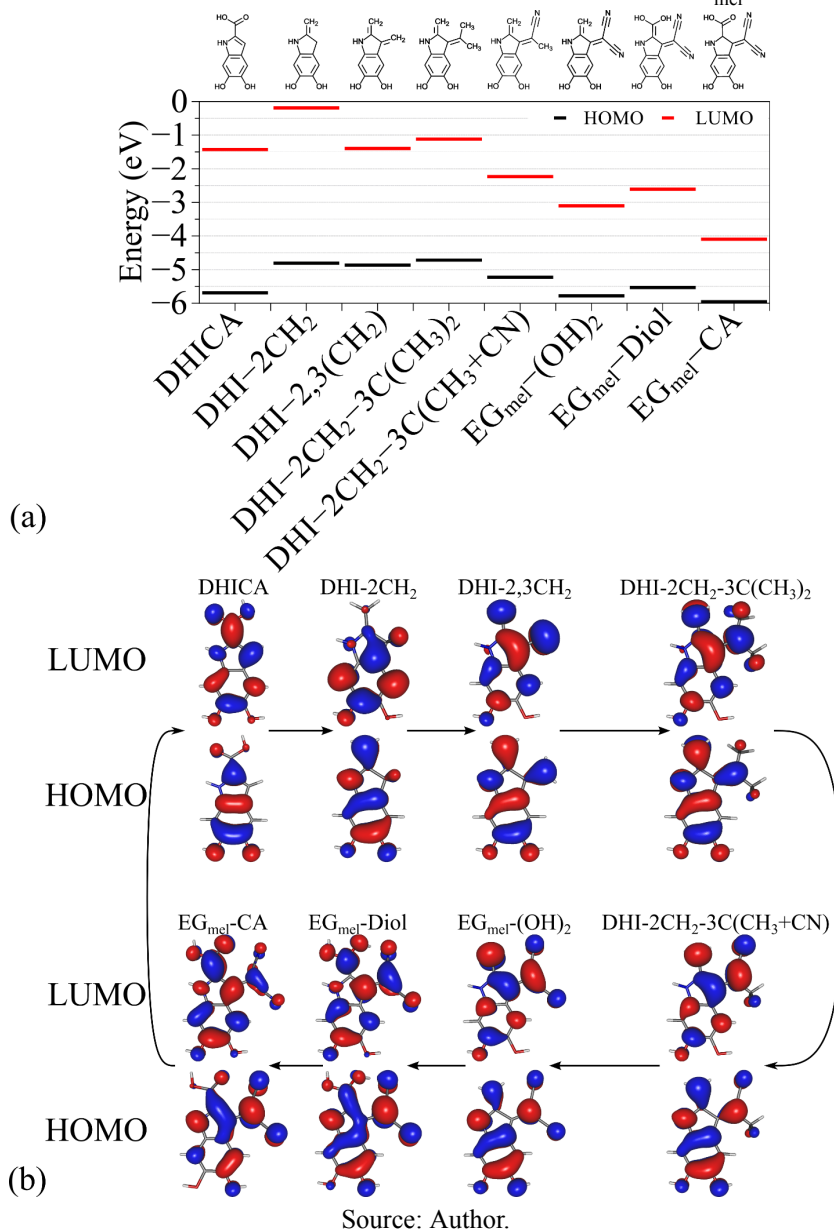
## 3.4 Results and discussions

### 3.4.1 Evaluation of $\text{EG}_{\text{mel}}$ : from DHICA to $\text{EG}_{\text{mel}}\text{-(OH)}_2$ and other intermediates

Figure 3.2a shows the relative alignment of the FMOs of DHICA and its derivatives up to the conversion to  $\text{EG}_{\text{mel}}\text{-(OH)}_2$  (our proposed melanin-based EG) and then to  $\text{EG}_{\text{mel}}\text{-CA}$ .

Figure 3.2b summarizes the spatial distribution of the Kohn-Sham molecular orbitals associated with these frontier energy levels.

**Figure 3.2** - (a) FMOs of DHICA and intermediate structures up to EG<sub>mel</sub>-CA; (b) Spatial distribution of DHICA and modifications to EG<sub>mel</sub>-



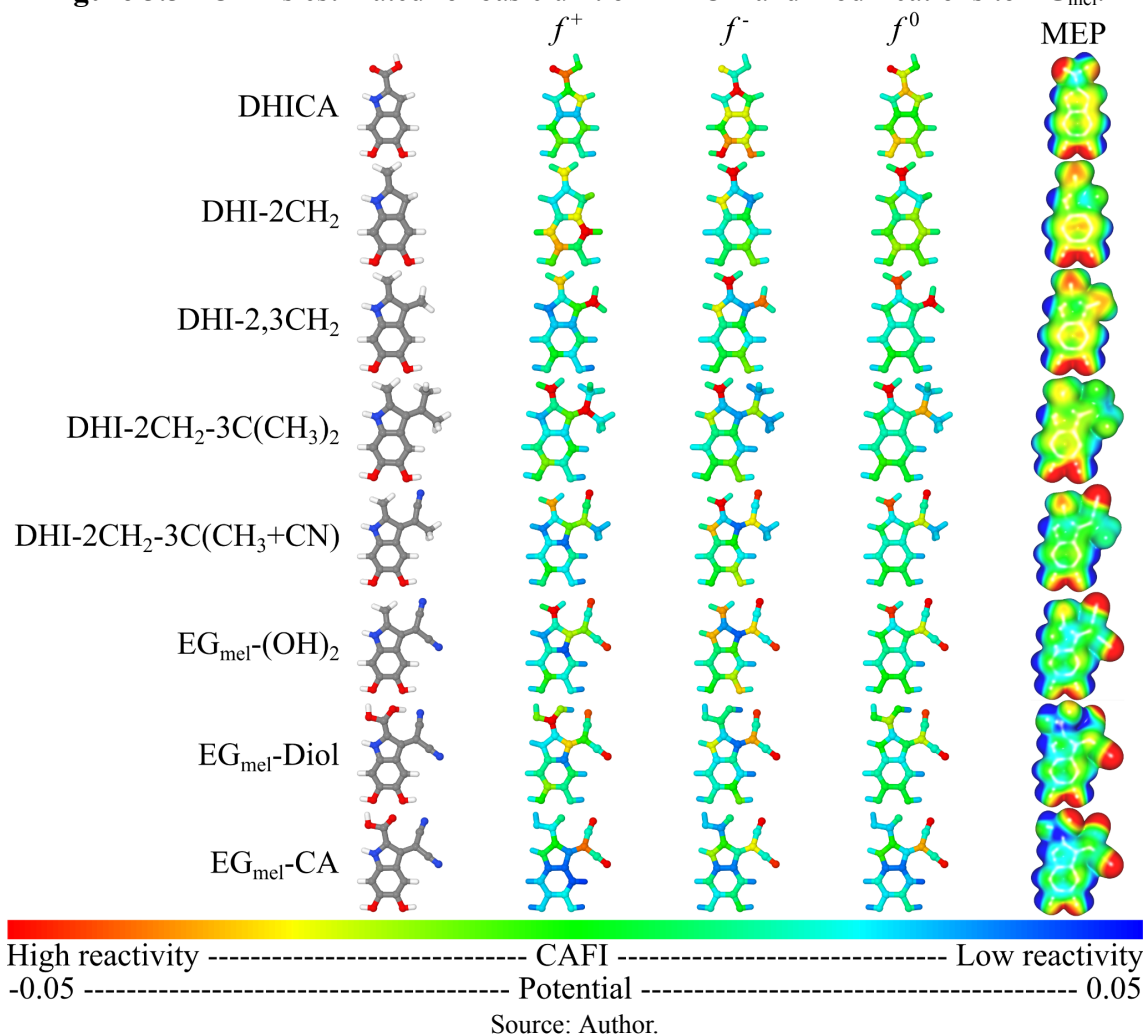
Note that the incorporation of methylene at 2-carboxylic acid (CA) position increases both FMOs energy. The addition of methylene at carbon 3 decreases the  $E_{\text{LUMO}}$  and consequently the  $E_{\text{gap}}$ . The subsequent changes up to EG<sub>mel</sub>-(OH)<sub>2</sub> reduce the HOMO and LUMO values, with no substantial changes to  $E_{\text{gap}}$ . The final incorporation of COOH at carbon 2 promotes a significant reduction on  $E_{\text{gap}}$ , leading to EG<sub>mel</sub>-CA, however, it eliminates the anchoring methylene group.

In relation to spatial distribution of the HOMO: (i) from DHICA to DHI-2CH<sub>2</sub> it is noticed a reduced contribution of carbon 2 and increased contribution of nitrogen, methylene, and carbon 3; (ii) the inclusion of methylene group on carbon 3 in DHI-2,3CH<sub>2</sub> increases the HOMO around the region. This pattern is repeated for subsequent structures up to EG<sub>mel</sub>-(OH)<sub>2</sub>, so that higher localization of the HOMO around five-membered ring ligands is noticed (mainly on C<sup>2</sup>-CH<sub>2</sub> and C<sup>3</sup>-C(CN)<sub>2</sub>, where C<sup>X</sup> indicates the carbon X of the main structure - see Fig. 3.1a. The replacement of 2-methylene by 2-(di-hydroxymethylene) and COOH spread out the HOMO over the main structure.

Regarding the LUMO, it is possible to address the following points: (i) from DHICA to DHI-2DH<sub>2</sub> the contributions of C<sup>2</sup>-COOH and C<sup>9</sup> decrease while C<sup>4</sup>, C<sup>5-6</sup> (linking C<sup>5</sup> and C<sup>6</sup>) and C<sup>7</sup> increase; (ii) the addition of the methylene group to C<sup>3</sup> in DHI-2,3CH<sub>2</sub> increases the contribution of methylene from C<sup>2</sup> and C<sup>3</sup>, in addition to C<sup>2-3-9</sup>. This pattern is maintained up to EG<sub>mel</sub>-(OH)<sub>2</sub>; (iii) with the replacement of 2-methylene by 2-(di-hydroxymethylene) and COOH, the LUMO comes back to the nitrogen, C<sup>2</sup>-Diol and C<sup>2</sup>-COOH. Similar localization effects can be seen at the quinone unit of DHICA, EG<sub>mel</sub>-Diol and EG<sub>mel</sub>-CA.

To investigate the role of the distinct units in electron acceptance/donation processes, we examined the local reactivities of these compounds. Figure 3.3 presents the CAFI (MEP) results as color scales. Red and blue regions indicate the position of reactive (negatively charged) and non-reactive (positively charged) sites, respectively. Intermediate reactivities (charge concentration) are represented by other colors following the RGB scale. High CAFIs (red atoms) indicate regions that are prone to interact with nucleophiles ( $f^+$ , accepting electrons from the environment), electrophiles ( $f^-$ , donating electrons to the environment), and free radicals ( $f^0$ , with no net change in the total number of electrons).

**Figure 3.3** - CAFIs estimated for basic unit of DHICA and modifications to EG<sub>mel</sub>.



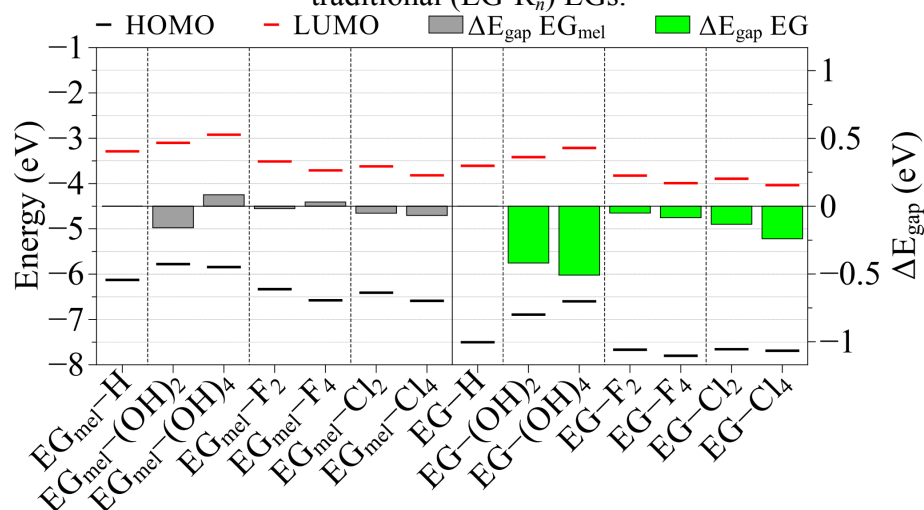
It is interesting to note that significant changes are noticed only from DHICA-to-DHI-2,3CH<sub>2</sub> species. From this structure up to EG<sub>mel</sub>-CA the local reactivity remains over the side groups, attached to the five-membered ring. It is important to identify the dominant role of the CN group on the reactivity of EG<sub>mel</sub>-(OH)<sub>2</sub>, indicating its high electron-acceptance/donation properties (see Figure B14a), already observed in distinct NFA structures<sup>13</sup>. The high reactivity identified on C<sup>2</sup>-CH<sub>2</sub> indicates the plausibility of EGs incorporation on NFA cores.

The MEP analysis reveals a high electron density on the nitrogen of the nitrile group and the oxygen of the hydroxyl group in all cases, which is consistent with the configuration observed for EG-F<sub>2</sub><sup>13</sup>. Notably, high charge concentration is also present on the indole groups, suggesting their potential for ionic conduction and ability to anchor within the device.

### 3.4.2 Comparison between EG<sub>mel</sub>-R and EG-R: influence of side groups attached on phenyl rings

To better understand the impact of additional side groups on EG<sub>mel</sub>, we conducted a comparative analysis between our eumelanin-inspired EGs (EG<sub>mel</sub>-R<sub>n</sub>) and traditional ones (EG-R<sub>n</sub>, for  $n = 2$  or  $4$ , and R = H, OH, F, or Cl). Figure 3.4 presents the relative positions of the KS-FMOs for these systems, along with the changes in the  $E_{\text{gap}}$  relative to R = H for each case. Notably, the EG-H and EG-F<sub>2</sub> systems correspond to EGs already incorporated into commercial NFAs, such as BZIC, ITIC, and Y6.

**Figure 3.4** - Energy levels of the FMO estimated for eumelanin-inspired (EG<sub>mel</sub>-R<sub>n</sub>) and traditional (EG-R<sub>n</sub>) EGs.

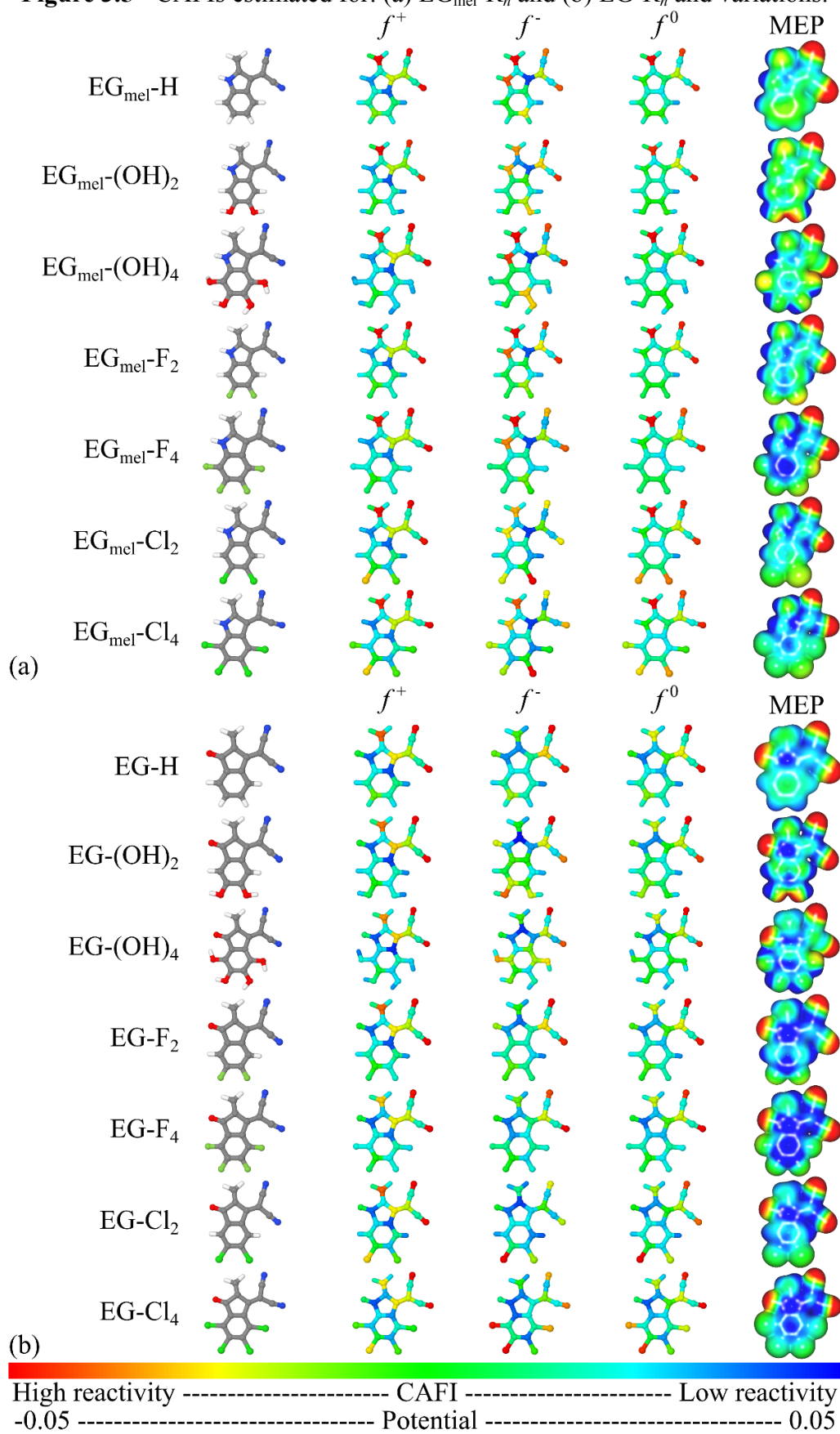


Source: Author.

When considering R = H as the reference system, it is observed that the inclusion of hydroxyl groups leads to an increase in the FMOs energies. In contrast, the incorporation of halogens promotes a decrease in FMO energy, with chlorine having a slightly stronger effect than fluorine. All structures show reduced  $E_{\text{gap}}$ , except EG<sub>mel</sub>-(OH)<sub>4</sub> and EG<sub>mel</sub>-F<sub>4</sub>, where the order of influence is: (OH)<sub>n</sub> > Cl<sub>n</sub> > F<sub>n</sub>. Notably, the impact on  $E_{\text{gap}}$  is more pronounced in the EG-R systems compared to their EG<sub>mel</sub>-R counterparts.

CAFI analyses were conducted to investigate the role of the distinct side groups on the local reactivity of the compounds. Figure 3.5 presents a summary of the obtained results, using the same definitions as in Figure 3.3.

**Figure 3.5** - CAFIs estimated for: (a)  $EG_{mel}-R_n$  and (b)  $EG-R_n$  and variations.



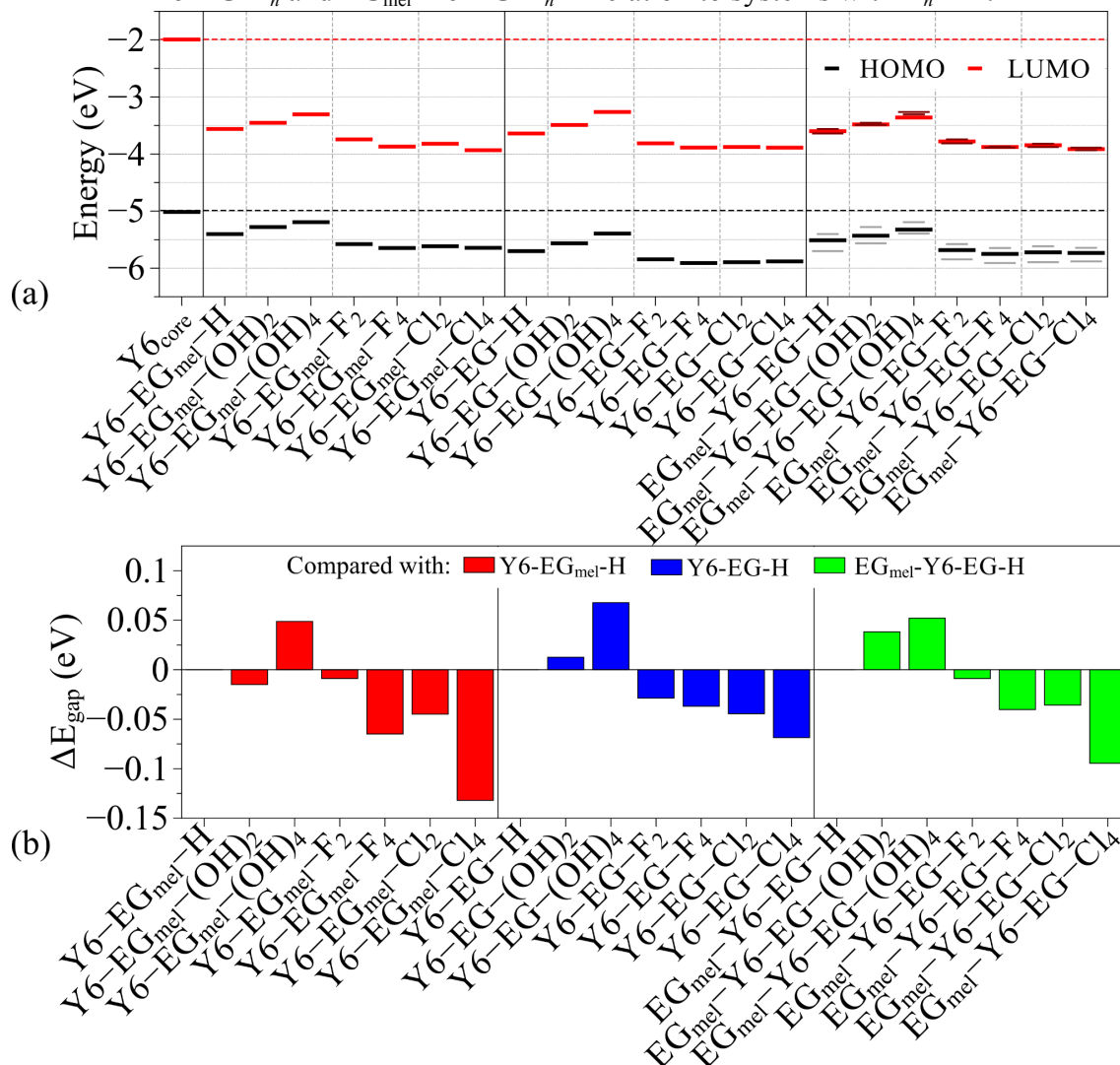
Figures 3.5a and 3.5b show that the high  $f^+$  indices for both,  $\text{EG}_{\text{mel}}$  and EG, are primarily located at the 2-methylene position. The  $f^-$  indices indicate high reactivity at the nitrogen of the indole, with some structures (e.g.  $\text{EG}_{\text{mel}}\text{-Cl}_2$ ,  $\text{EG}_{\text{mel}}\text{-Cl}_4$ ,  $\text{EG-Cl}_2$ , and  $\text{EG-Cl}_4$ ) also displaying elevated  $f^-$  values at atoms bonded to carbons 5, 6, and 7. Additionally, all structures exhibit high  $f^+$  and  $f^-$  indices at the nitrile groups. The MEP analysis reveals a high electron density mainly on the nitrogen of the nitrile and on the oxygen of the hydroxyl group in  $\text{EG}_{\text{mel}}$ . High electron density is also noticed on the oxygen of ketone in EG.

In general, there are no significant changes in the CAFI indexes and MEP of  $\text{C}\equiv\text{N}$  groups for traditional EG and  $\text{EG}_{\text{mel}}$ . Given the relevance of EGs on the performance of NFAs, this suggests that the EG-R and  $\text{EG}_{\text{mel}}\text{-R}$  can present similar responses. The high  $f^-$  and  $f^+$  reactivity indexes in  $\text{C}^2$  of  $\text{EG}_{\text{mel}}\text{-R}$  suggest an improved internal charge transfer of this group compared to EG.

### 3.4.3 Incorporation of $\text{EG}_{\text{mel}}\text{-R}_n$ and $\text{EG-R}_n$ groups on $\text{Y6}_{\text{core}}$

Figure 3.6 shows the effect induced on the frontier energy levels and electronic gaps by incorporating  $\text{EG}_{\text{mel}}\text{-R}_n$  and  $\text{EG-R}_n$  groups into the Y6 core. These effects are evaluated for both, symmetric ( $\text{EG}_{\text{mel}}/\text{Y6}_{\text{core}}/\text{EG}_{\text{mel}}$  and  $\text{EG}/\text{Y6}_{\text{core}}/\text{EG}$ , referred to as  $\text{Y6-EG}_{\text{mel}}\text{-R}_n$  and  $\text{Y6-EG-R}_n$ , respectively) and asymmetric structures ( $\text{EG}_{\text{mel}}/\text{Y6}_{\text{core}}/\text{EG}$ , referred to as  $\text{EG}_{\text{mel}}\text{-Y6-EG-R}_n$ , where both EG share the same  $\text{R}_n$  ligand). The changes noticed on the gaps (Figure 3.6b) were estimated in relation to systems with  $\text{R}_n = \text{H}$ .

**Figure 3.6** - (a) Relative alignment of the FMOs for Y6-based structures, the tiny (H: gray and L: wine) levels displayed for heterogeneous systems indicate the energy levels of homogeneous analogues (short: EG<sub>mel</sub> long: EG) and (b) Variation of  $E_{\text{gap}}$  of Y6-EG<sub>mel</sub>-R<sub>n</sub>, Y6-EG-R<sub>n</sub> and EG<sub>mel</sub>-Y6-EG-R<sub>n</sub> in relation to systems with R<sub>n</sub> = H.



Source: Author.

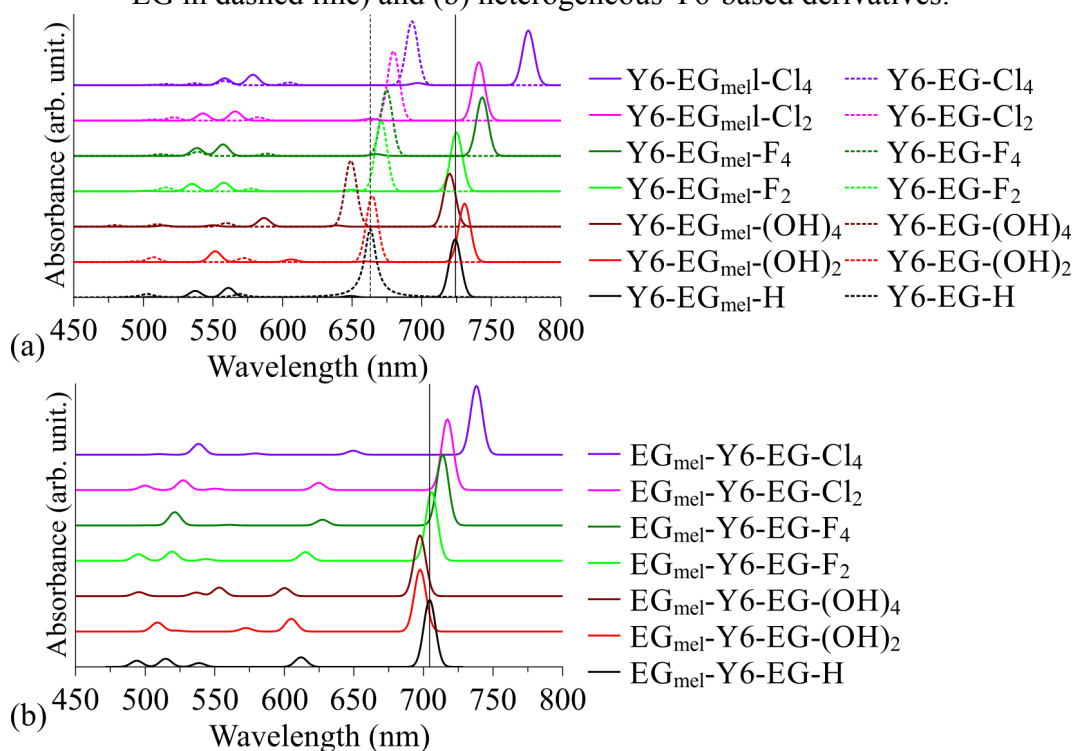
Figure 3.6a illustrates a significant reduction of the electronic gaps in relation to Y6<sub>core</sub>. In general, it is noticed the same trend observed in Figure 3.4 for FMO evolution. The impact of functional groups becomes more pronounced as the number of halogens or hydroxyls ( $n$ ) increases. Notably, heterogeneous structures exhibit intermediate energy levels relative to their homogeneous counterparts. In particular, greater differences between EG<sub>mel</sub>-R<sub>n</sub> and EG-R<sub>n</sub> homogeneous structures are observed in the HOMO levels.

Figure 3.6b reveals a general trend in  $E_{\text{gap}}$  variations: (i) the incorporation of halogens leads to a reduction in  $E_{\text{gap}}$ , with more pronounced effects as the number of substituents ( $n$ ) increases; (ii) hydroxyl groups, in contrast, increase  $E_{\text{gap}}$  values, with stronger effects for  $n = 4$  compared to  $n = 2$ . An exception is observed in the homogeneous EG<sub>mel</sub>-(OH)<sub>2</sub>-based system,

though this behavior aligns with the trend shown in Figure 3.4. Notably, halogens have a greater impact on  $EG_{mel}-R_n$  systems than on  $EG-R_n$  counterparts.

Figure 3.7 presents the optical absorption spectra for both homogeneous and heterogeneous systems. The absorbance intensities are normalized to the most intense peak within each type of structure.

**Figure 3.7** - Theoretical optical absorption spectra of: (a) homogeneous ( $EG_{mel}$  solid line and EG in dashed line) and (b) heterogeneous Y6-based derivatives.

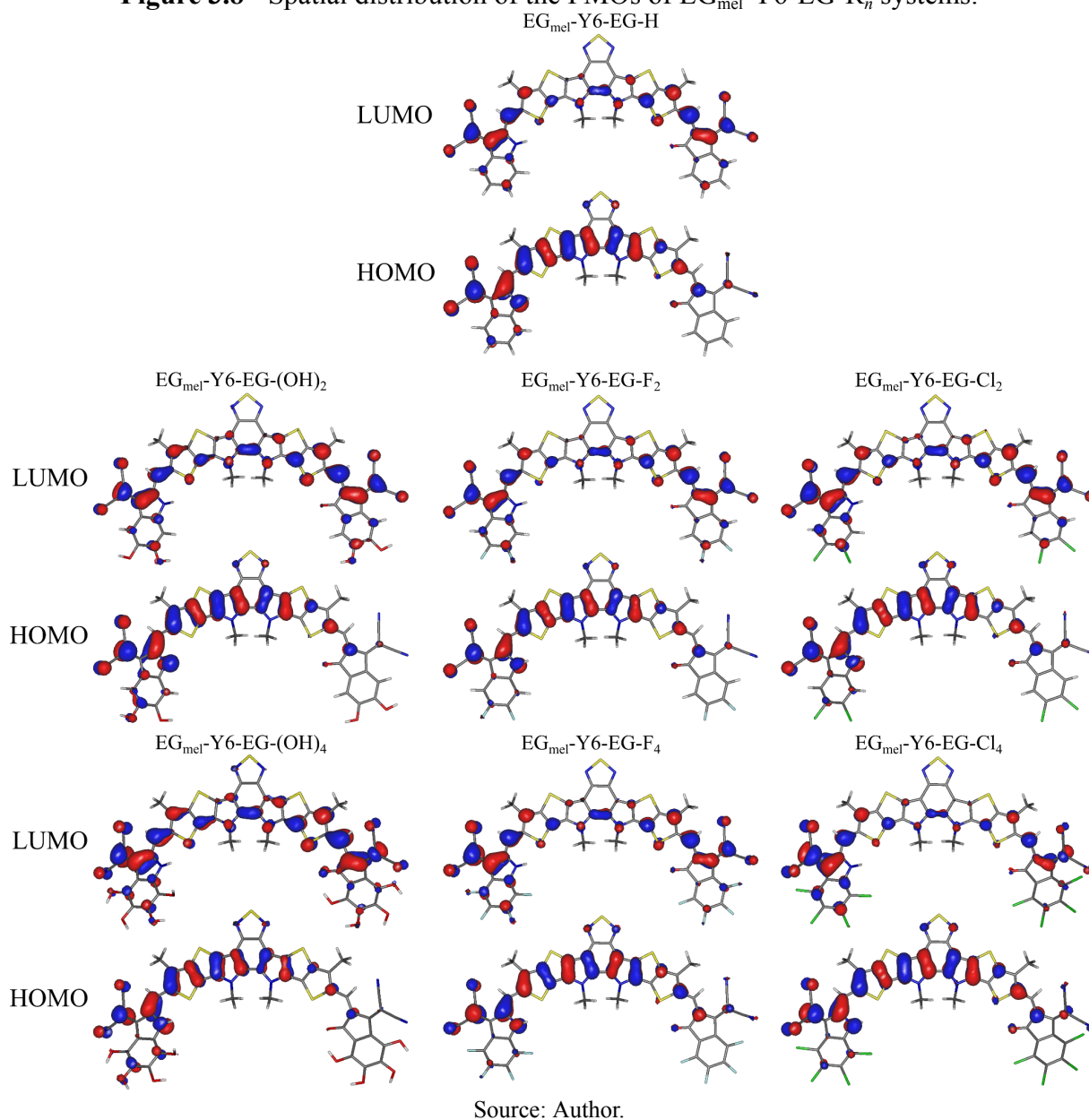


Source: Author.

Most of the homogeneous systems exhibit a slight red shift when compared to  $Y6-EG_{mel}-H$  and  $Y6-EG-H$  (724 and 663 nm, respectively), except for  $R_n = (OH)_4$ .  $EG_{mel}-R_n$  based systems present a wide absorption range, from 720 to 777 nm (for  $Y6-EG_{mel}-(OH)_4$  and  $Y6-EG_{mel}-Cl_4$ , respectively), while  $EG-R_n$  based ones absorb between 649 and 693 nm ( $Y6-EG-(OH)_4$  and  $Y6-EG-Cl_4$ , respectively). Figure 3.7b shows that the presence of OH groups on heterogeneous systems promotes a slight blue-shift in the spectra, while halogens lead to red-shifts, of up to 33 nm for  $R = Cl_4$  (compared to  $EG_{mel}-Y6-EG-H$ ). The effects are sensitive to the  $n$ , with stronger effects for a higher number of ligands (the individual results of the optical absorption spectra of DHICA and EGs are presented in Figures B2 and B3 in the Appendix B).

The above presented results suggest that a blend of such NFAs could amplify the optical absorption range of the devices (from 649 up to 777 nm). In order to assess the properties of the mixture of Y6 melanin-based and Y6 traditional structures, complementary studies considering clusters were conducted. These studies indicated an effective absorption range between 695 and 765 nm (see Figure B4 in Appendix B). This finding suggests that the melanin-based structures can dominate the optical absorption properties in mixed systems.

**Figure 3.8** - Spatial distribution of the FMOs of  $EG_{mel}$ -Y6-EG- $R_n$  systems.

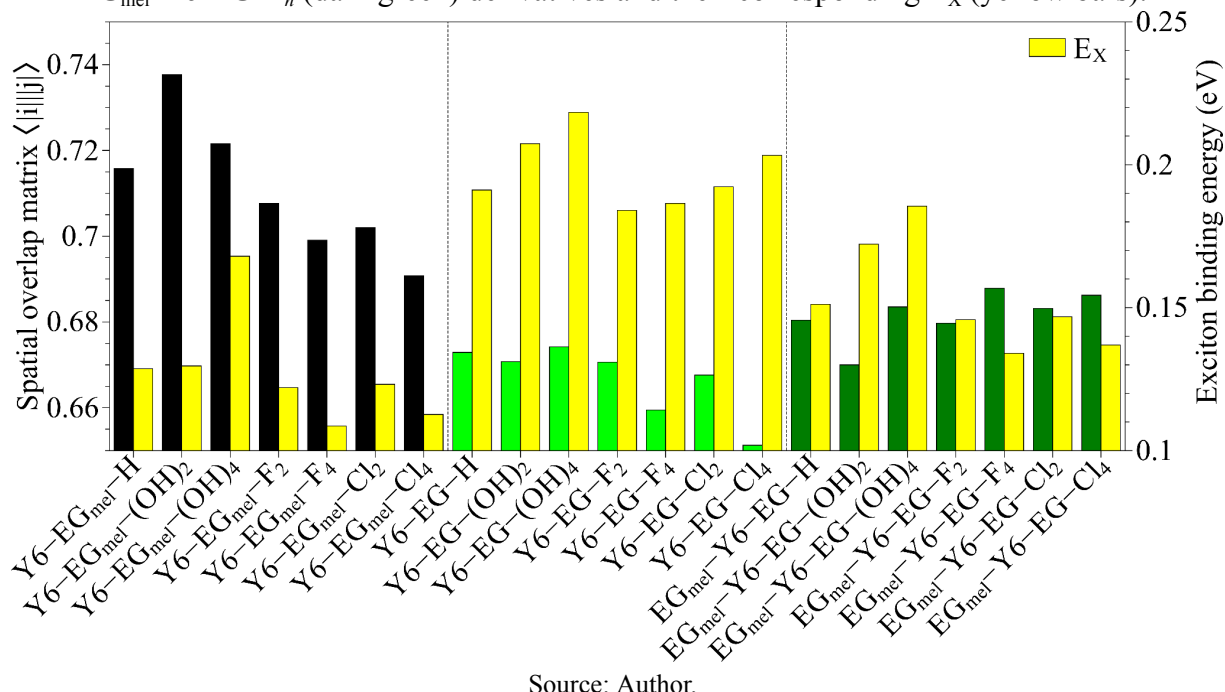


Homogeneous symmetric Y6-EG<sub>mel</sub>- $R_n$  and Y6-EG- $R_n$  structures (Figures B8 and B9 respectively) present an uniform spatial distribution of the FMOs on the Y6<sub>core</sub>, with the

LUMO primarily situated on the EGs. It is noticed the influence of hydroxyls on the HOMO composition, shifting this orbital to carbons 5, 7, and 9. Small, similar effects are noticed for  $R_n = F_4$  and  $Cl_4$ . The strong orbital overlap reduces the exciton binding energy and enhances charge mobility by promoting greater delocalization of the frontier molecular orbitals along the acceptor structure.

Figure 3.8 highlights the dominance of  $EG_{mel}-R_n$  groups in the HOMO compared to  $EG-R_n$  in heterogeneous derivatives, which is not so evident for the LUMO. Consequently, the H-L overlap is reduced in  $EG_{mel}-R_n$ -based homogeneous systems, although it remains generally larger than in  $Y6-EG-R_n$  ones (see Figure 3.9). Conversely, for exciton binding energies (Figure 3.9), smaller  $E_x$  values are observed for  $EG_{mel}-R_n$ -based structures, followed by  $EG_{mel}-Y6-EG-R_n$  heterogeneous asymmetric systems.  $Y6-EG-R_n$  structures exhibit the highest  $E_x$  values (see Table B2, Table B3, Figures B10 and B11 in Appendix B for details), indicating that charge mobility is favored in melanin-based systems.

**Figure 3.9** - H-L spatial overlap for  $Y6-EG_{mel}-R_n$  (black),  $Y6-EG-R_n$  (light green) and  $EG_{mel}-Y6-EG-R_n$  (dark green) derivatives and their corresponding  $E_x$  (yellow bars).



Source: Author.

Figures 3.10a-b and 3.11 display color maps corresponding to the CAFIs and MEPs of the systems, using the same definitions as those in Figure 3.3.

**Figure 3.10** - CAFIs estimated for homogeneous symmetric systems (a) Y6-EG<sub>mel</sub>-R<sub>n</sub> and (b) Y6-EG-R<sub>n</sub>.

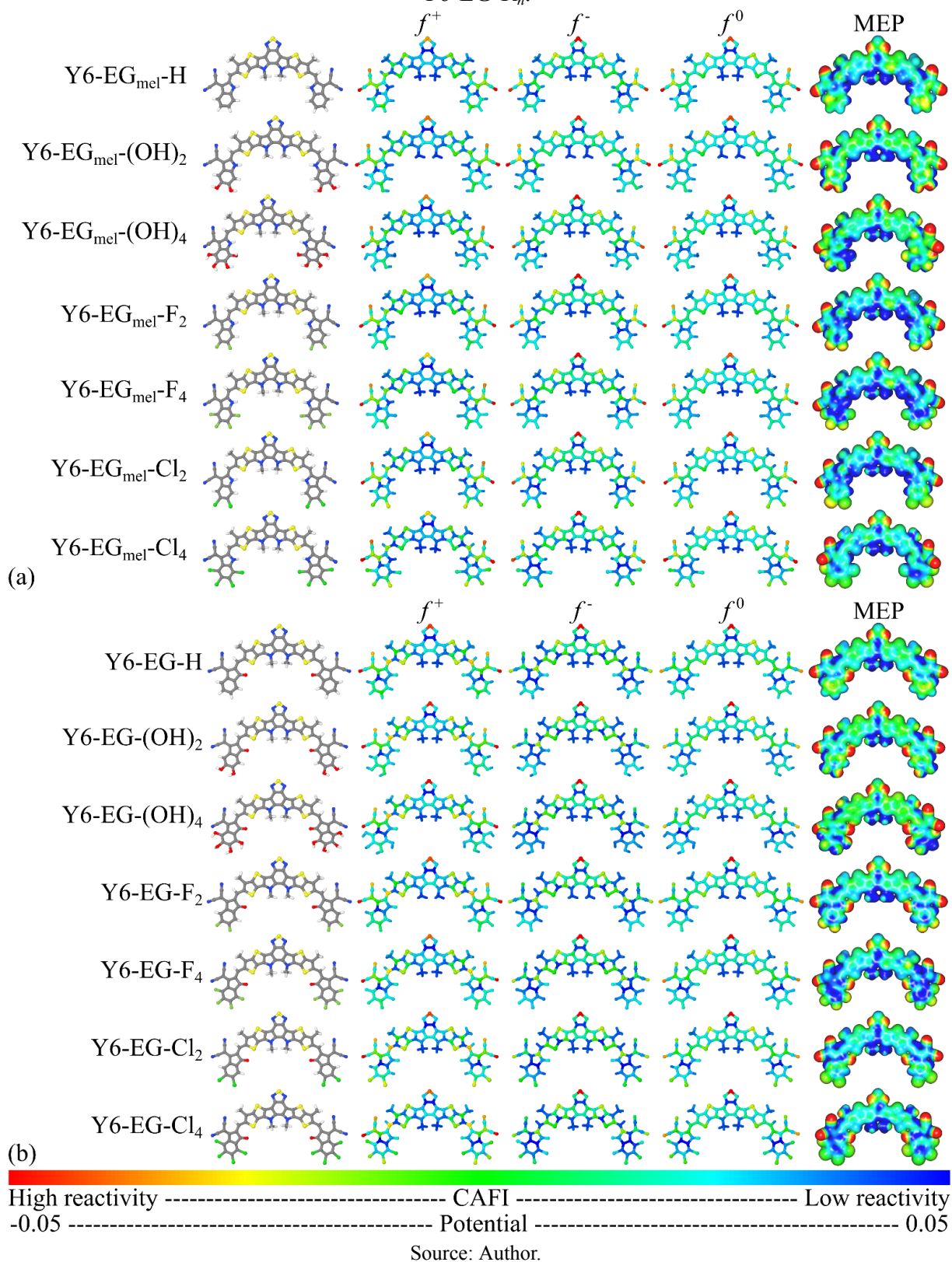
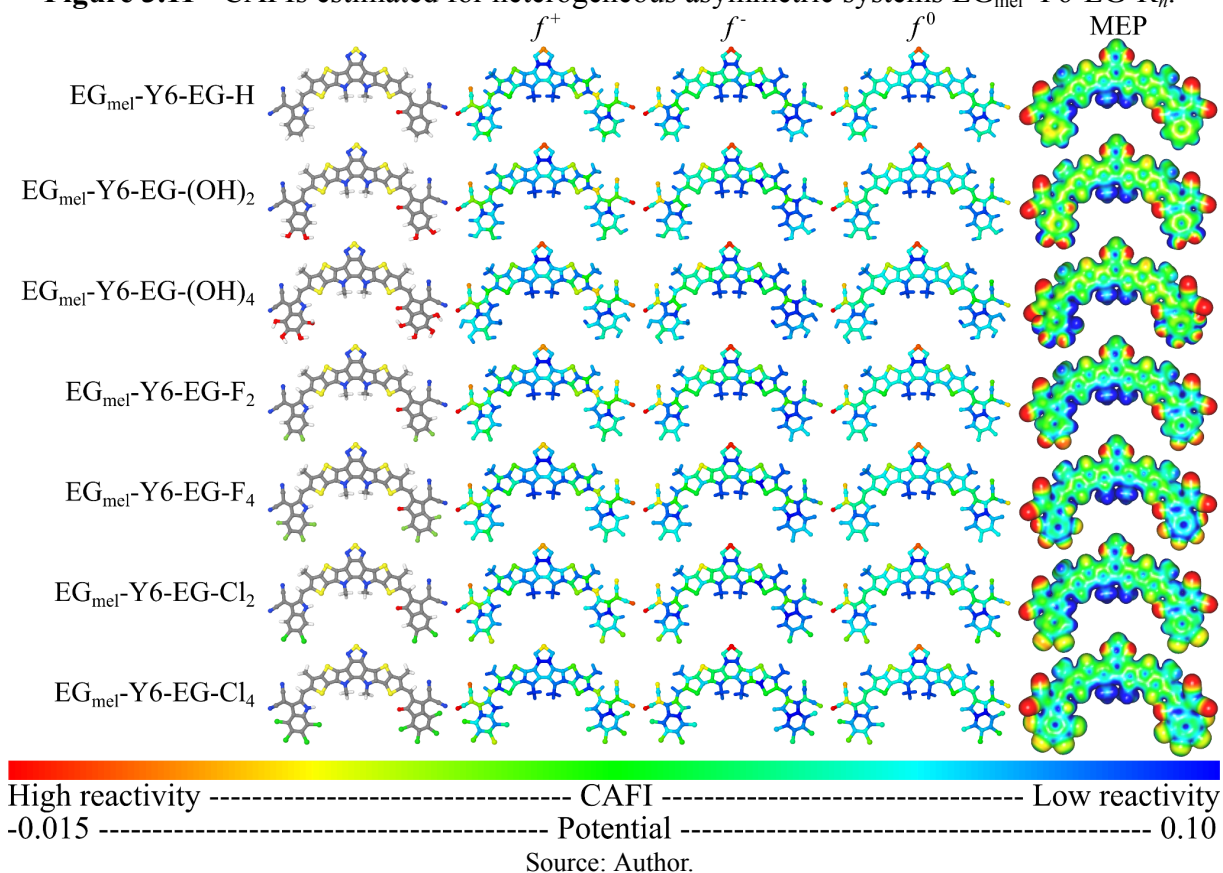


**Figure 3.11** - CAFIs estimated for heterogeneous asymmetric systems  $\text{EG}_{\text{mel}}\text{-Y6-EG-R}_n$ .



The local reactivity of Y6 (Y6-EG-F<sub>2</sub>) reveals three primary reactive sites for  $f^+$ : (i) the central sulfur atom, and (ii) the two nitriles attached to the EG. In contrast, a single reactive site for  $f^-$  is observed, located on the central sulfur. This pattern suggests two main charge transfer (CT) routes involving EG and the central region of the core, with a predominant contribution from the central sulfur. This behavior has been reported for Y6<sup>13,112</sup> and is observed in all Y6-EG-R<sub>n</sub>-based derivatives.

Conversely, the Y6-EG<sub>mel</sub>-R<sub>n</sub>-based systems exhibit a slightly different behavior, with charge transfer (CT) processes primarily centered around the side CN groups rather than the central sulfur. This distinction could significantly impact charge transport, especially when considering the various stacking configurations of Y6<sup>135,136</sup>.

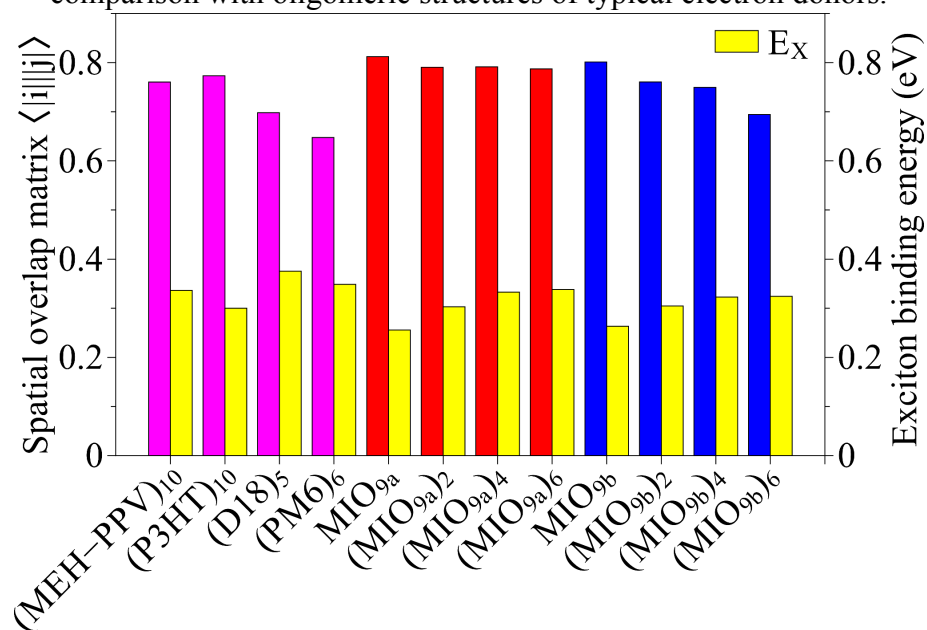
Heterogeneous structures exhibit asymmetrical reactivity, particularly noticeable for  $f^-$ , with the dominance of EG<sub>mel</sub>-R<sub>n</sub>. This feature could hinder some charge transfer (CT) processes by reducing the effective spatial alignment between the donor and acceptor domains in the device's active layer.

Finally, MEP shows a weak dependence with the distinct EGs. Heterogeneous structures present slightly asymmetrical charge distribution, which could affect NFA crystallization and lead to different molecular packing compared to literature reports<sup>135–137</sup>.

### 3.4.4 Evaluation of melanin-inspired oligomeric structures: MIO<sub>9a</sub> and MIO<sub>9b</sub>

The MIO<sub>9a</sub> and MIO<sub>9b</sub> oligomers investigated in this work are based on melanin-inspired structures originally developed by Selvaraju et al.<sup>7</sup> as bio-derived semiconducting materials. These molecules, synthesized from the renewable compound vanillin, feature  $\pi$ -conjugated backbones with alkynyl linkers that enhance molecular planarity and charge transport<sup>49</sup>. Polymerization of the eumelanin-inspired core resulted in a material with a maximum absorption at 526 nm in thin films, with high absorption in the visible range. This indicates a strong potential for light harvesting, enhancing their applicability in photovoltaic devices. Figure 3.12 illustrates the H-L orbital overlap and exciton binding energies of these melanin-inspired compounds in comparison with widely used polymeric donors, including MEH-PPV, P3HT, PM6, and D18. This comparison provides valuable insights into the optoelectronic viability of MIO<sub>9a</sub> and MIO<sub>9b</sub> as alternative donor materials, particularly considering their bio-based origin, synthetic accessibility, and structural features that support efficient exciton separation and charge mobility.

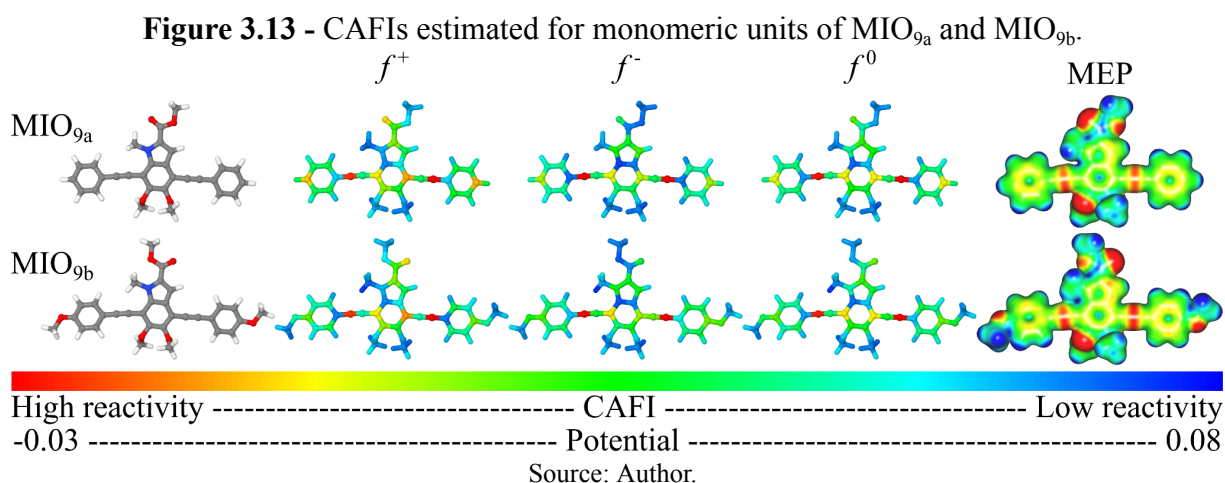
**Figure 3.12** - H-L spatial overlap and exciton binding energies of MIO<sub>9a</sub> and MIO<sub>9b</sub> in comparison with oligomeric structures of typical electron donors.



Source: Author.

As shown in Figure B12 (Appendix B), the HOMO of these compounds are evenly distributed across the entire structure, while the LUMOs are mainly concentrated at the center of the oligomeric chains. As the main chain length increases, a reduction in H-L overlap is observed, especially in the MIO<sub>9b</sub> structures. Despite this feature, as shown in Figure 3.12, the H-L overlap remains significantly higher for these structures in comparison to those of typical donors, indicating an efficient optical response of these melanin-based systems. Furthermore, it is still worth mentioning that the exciton binding energies are comparable to those of standard donor materials.

Figure 3.13 shows CAFI and MEP color maps estimated for MIO monomers, utilizing the same definitions outlined for Figure 3.3. Results associated with more extended oligomeric structures are presented in Figure B13 (Appendix B), showing similar behaviors.

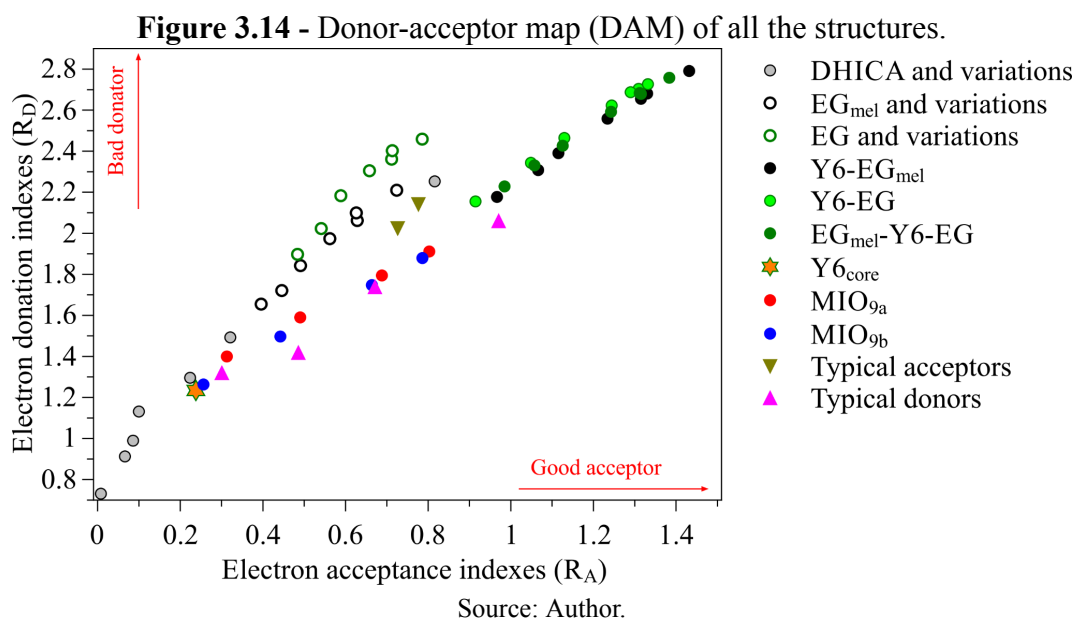


For both cases, high reactivity is noticed on the C≡C groups, these bonds facilitate conjugation and delocalization, while reinforcing molecular rigidity and planarity, that are essential for efficient charge transport in organic materials<sup>49</sup>. The molecular electrostatic potential exhibits high electronic density at the carbon-carbon triple bond and oxygen atoms. Similar trends are observed for larger oligomers, although the reactivity shifts towards the terminal units (see Figure B13 in Appendix B for details).

### 3.4.5 Estimation of performance parameters

Figure 3.14 presents the donor-acceptor map (DAM) for all the structures evaluated in the previous sections, alongside typical fullerene-based acceptors and polymeric donors. The gray circles represent the set of DHICA-modified EGs, while open circles indicate the various (isolated) EG<sub>mel</sub>-R<sub>n</sub> and EG-R<sub>n</sub> groups. Y6<sub>core</sub> is marked by an orange star, representing the

central structure of Y6 as described by Lu et al.<sup>109</sup>. Typical polymeric donors are shown as magenta upward triangles, which can be compared with the MIO<sub>9a</sub> and MIO<sub>9b</sub> (represented by red and blue filled circles). Fullerene-based acceptors are indicated by dark yellow downward triangles, while black, light green, and dark green filled circles represent different Y6-based NFA compounds (further details can be found in Figure B14 in the Appendix B). In DAM, low  $R_D$  values indicate a good donor, while high  $R_A$  are associated with good acceptors.



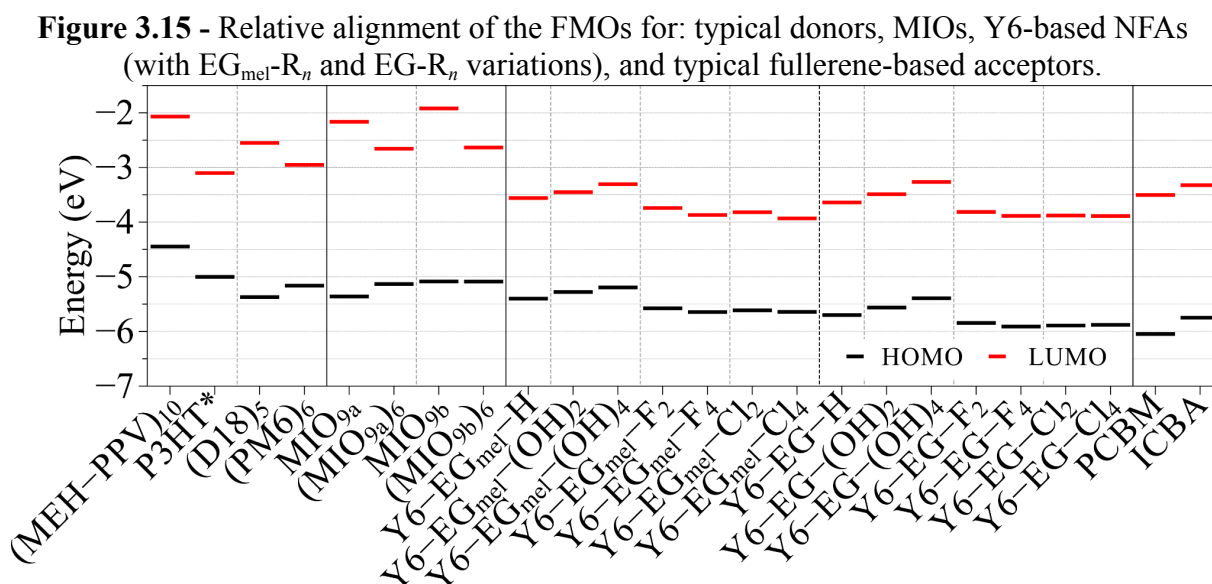
Note that isolated DHICA and its variations can be characterized as good electron donors and bad acceptors. MIO<sub>9a</sub>, MIO<sub>9b</sub> and Y6<sub>core</sub> are good electron donors, being situated around typical electron donors (where P3HT > MEH-PPV > D18 > PM6 in terms of electron donation indexes, see Figure B15 for details). The substitution/addition of  $R_n$  groups induces the similar effects on EG<sub>mel</sub> and EG, improving the acceptance ability of these structures, according to the following sequence: (OH)<sub>4</sub> < (OH)<sub>2</sub> < H < F<sub>2</sub> < F<sub>4</sub> < Cl<sub>2</sub> < Cl<sub>4</sub>. The overall influence sequence: (OH)<sub>n</sub> < H<sub>n</sub> < F<sub>n</sub> < Cl<sub>n</sub> on the acceptance abilities of the compounds is also noticed for the proposed NFAs.

All the proposed Y6-EG<sub>mel</sub>-R<sub>n</sub>, Y6-EG-R<sub>n</sub> and EG<sub>mel</sub>-Y6-EG-R<sub>n</sub> present higher  $R_A$  in relation to their isolated building blocks (Y6<sub>core</sub> and EGs), being located on the right top of the DAM. Note that such NFAs present higher electron acceptance power in relation to typical fullerene-based acceptors. In particular, among the entire set of molecules, EG<sub>mel</sub>-Y6-EG-Cl<sub>4</sub> and Y6-EG<sub>mel</sub>-Cl<sub>4</sub> emerge as the most effective acceptors (see Fig. B14).

Figures 3.14 and B16 reveal linear trends for donors (typical systems and MIO<sub>9a/9b</sub>) and acceptors (fullerene- and Y6-based ones), with similar slopes ( $\alpha \approx 1.19$  and 1.12) but

different intercepts, indicating quasi-parallel behavior (see Fig. B16 for details). This suggests that as acceptor strength increases, donor capacity decreases at a consistent rate, with an average slope  $\alpha^* \approx 1.155$ . A similar behavior has been identified by our group for other systems<sup>138</sup>, which defines a criterion for efficient D:A pairs: lines connecting the points ( $R_A^A$ ,  $R_D^A$ ) and ( $R_A^D$ ,  $R_D^D$ ) in DAM should present slopes greater than 1.16, as shown in Figure B16.

To estimate the applicability of eumelanin-inspired structures in optoelectronic devices, comparative analysis regarding the relative alignment of the FMOs were performed considering typical electron donors and acceptors. Figure 3.15 shows the HOMO and LUMO levels of the compounds (experimental data were considered for P3HT\*<sup>139</sup> due to saturation problems).



Source: Author.

Note that Y6-based compounds present appropriate LUMO level alignments with most of the polymer-based donors (including MIO<sub>9a</sub> and MIO<sub>9b</sub>) for electron acceptance. However, some drawbacks are noticed in relation to the HOMO.

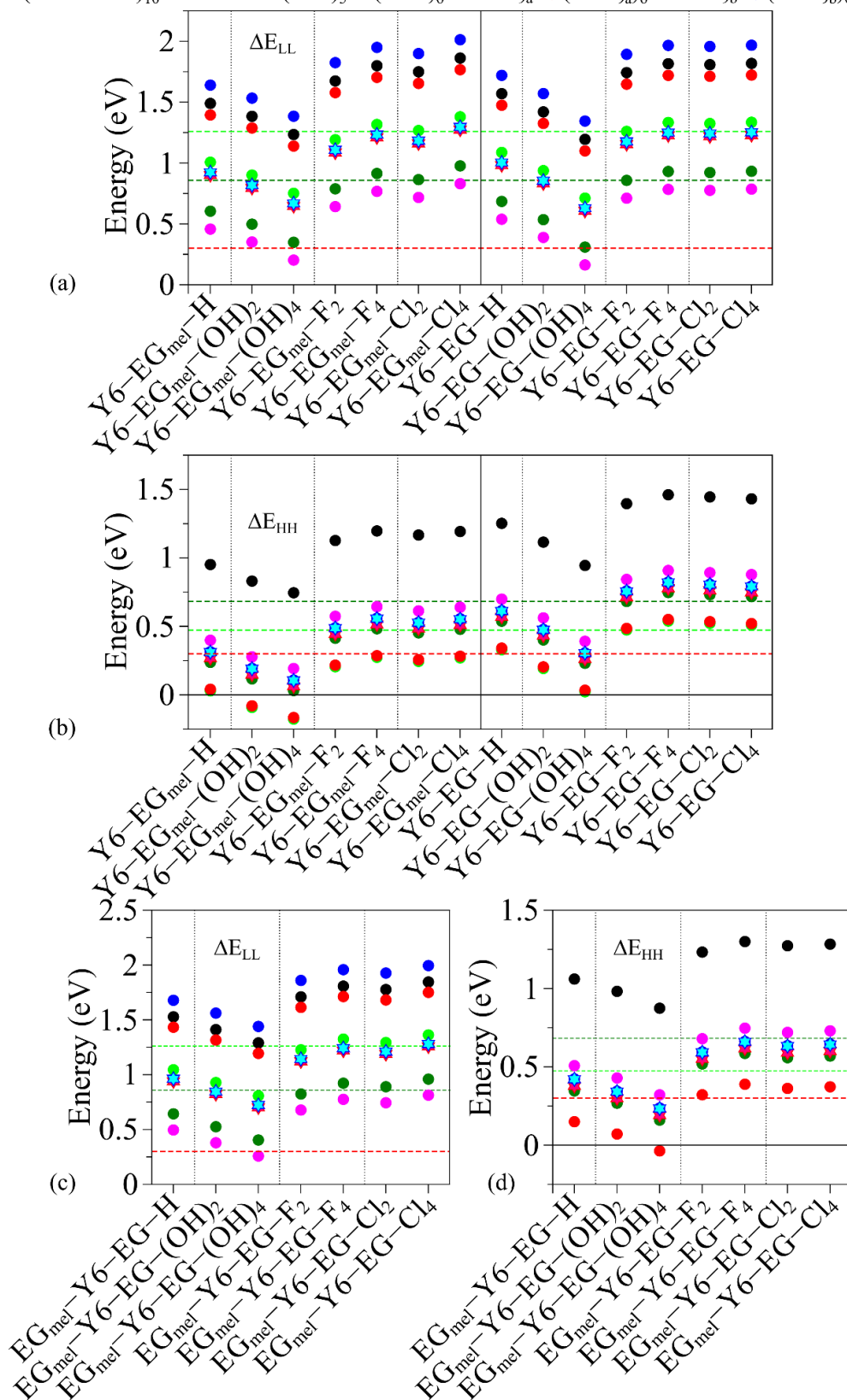
In general, efficient BHJOSCs are supposed to present high  $V_{OC}$  (maximum voltage that can be provided by a photovoltaic device under certain conditions of radiation and temperature), which are associated with high  $\Delta E_{HDLA}$  values<sup>140,141</sup>. However, an appropriate balance between  $\Delta E_{HDLA}$  and other parameters, such as  $E_{gap}$ ,  $\Delta E_{HH}$  and  $\Delta E_{LL}$  (see Figure B1) is necessary to facilitate the excitons dissociation (and avoid their recombination) while still maintaining an appreciable  $V_{OC}$ . In particular,  $\Delta E_{HH}$  and  $\Delta E_{LL}$  values higher than  $E_X$  (e.g. 0.3 eV) are desirable. In addition, effective alignments between electrodes work functions ( $w_{anode}$

and  $w_{\text{cathode}}$ ) and D and A FMOs are expected to achieve effective charge transfers (e.g.  $w_{\text{anode}} > \text{HOMO}_D$  and  $w_{\text{cathode}} < \text{LUMO}_A$ )<sup>131,142-144</sup> (see Figure B1 for a better visualization of parameters relevance).

To help the analysis of systems' performance  $\Delta E_{\text{LL}}$ ,  $\Delta E_{\text{HH}}$  and  $V_{\text{OC}}$  parameters were estimated for distinct D:A combinations, as presented in Figures 3.16-3.17. The red dashed line represents the typical exciton binding energy value (0.3 eV), which sets a threshold for non-operational devices. Systems below this line exhibit undesirable negative  $\Delta E_{\text{LL}}$  and  $\Delta E_{\text{HH}}$  values. The green and bright green dashed lines correspond to the values for PM6:Y6 and D18:Y6, respectively, D:A pairs with the high PCE<sup>98,11,106,108,136</sup>.

**Figure 3.16** - Analyses of  $\Delta E_{LL}$  and  $\Delta E_{HH}$  performance parameters for homogeneous asymmetric Y6-based systems, Y6-EG<sub>mel</sub>-R<sub>n</sub> (a) and Y6-EG-R<sub>n</sub> (b), as well as heterogeneous asymmetric ones (c and d) by considering distinct donors.

● (MEH-PPV)<sub>10</sub> ● P3HT\* ● (D18)<sub>5</sub> ● (PM6)<sub>6</sub> ● MIO<sub>9a</sub> ★ (MIO<sub>9a</sub>)<sub>6</sub> ● MIO<sub>9b</sub> ★ (MIO<sub>9b</sub>)<sub>6</sub>

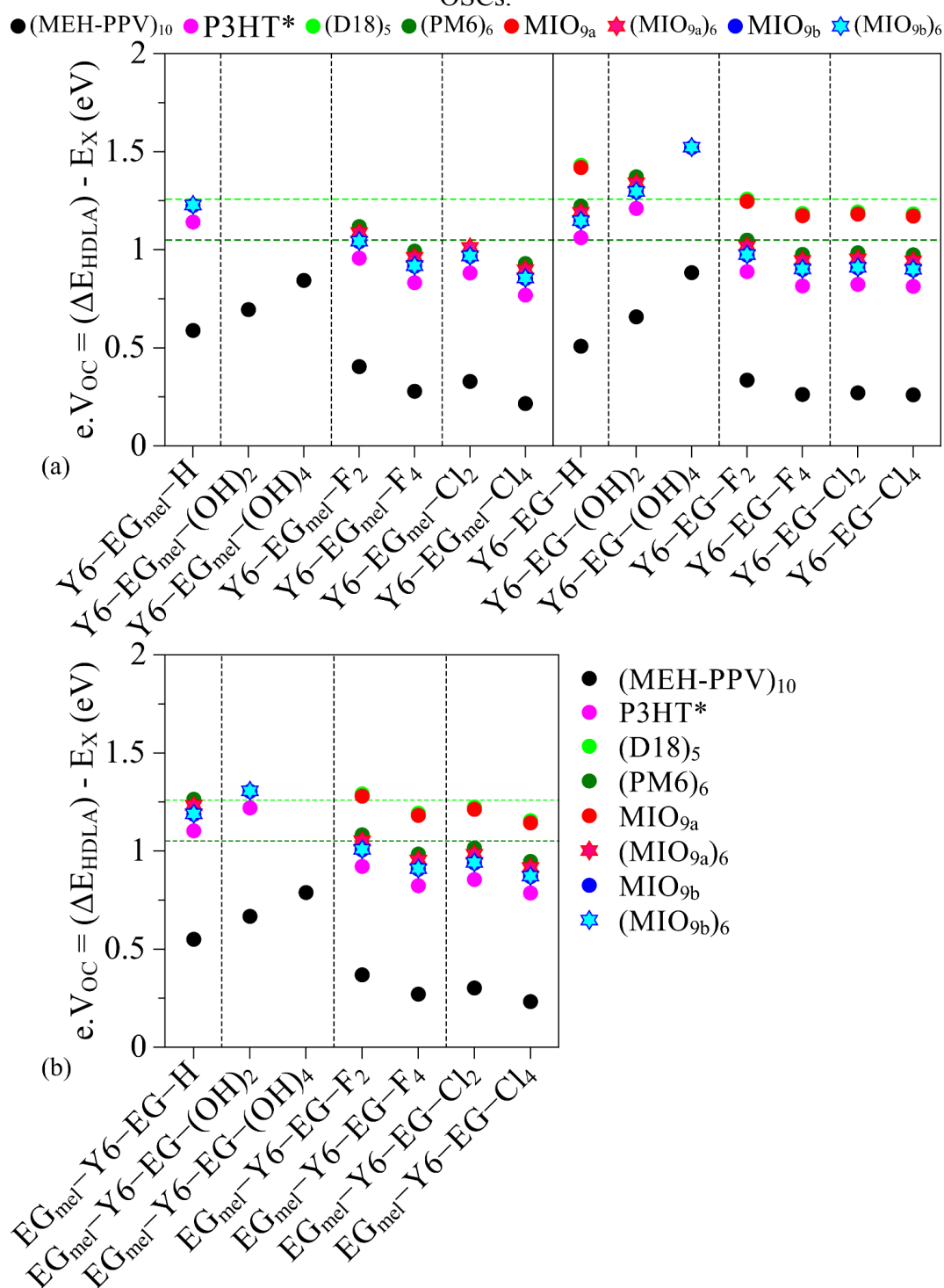


Source: Author.

Figure 3.16a highlights the inability of the P3HT:Y6-EG<sub>mel</sub>-(OH)<sub>4</sub> and P3HT:Y6-EG-(OH)<sub>4</sub> pairs in enabling efficient photovoltaic performances. Figure 3.16b indicates that several combinations, specifically those under the dashed red line, are non-functional. This includes most of the Y6-EG<sub>mel</sub>-R<sub>n</sub>, MIO<sub>9a</sub>, MIO<sub>9b</sub>, and D18-based systems. For the Y6-based heterogeneous systems (Figure 3.16c), inappropriate  $\Delta E_{LL}$  values are observed for P3HT:EG<sub>mel</sub>-Y6-EG-(OH)<sub>4</sub>. Furthermore, many MIO<sub>9a</sub>-based systems, except for those with R<sub>n</sub> = F<sub>n</sub> and Cl<sub>n</sub>, show poor  $\Delta E_{HH}$  values (Figure 3.16d).

Figure 3.17 presents the V<sub>OC</sub> values, estimated from Eq. 3.5. Only systems with  $\Delta E_{HH}$  and  $\Delta E_{LL}$  greater than 0.3 eV were considered. The V<sub>OC</sub> values estimated for MIO<sub>9b</sub> and (MIO<sub>9b</sub>)<sub>6</sub> are graphically indistinguishable, given their very close HOMO values, as well as those of MIO<sub>9a</sub> and D18.

**Figure 3.17** - Comparative analyses of  $V_{OC}$  of the eumelanin-base compounds as donors, Y6 EGmel and Y6 SG in relation to the fullerene compounds and donors typically employed in OSCs.



Source: Author.

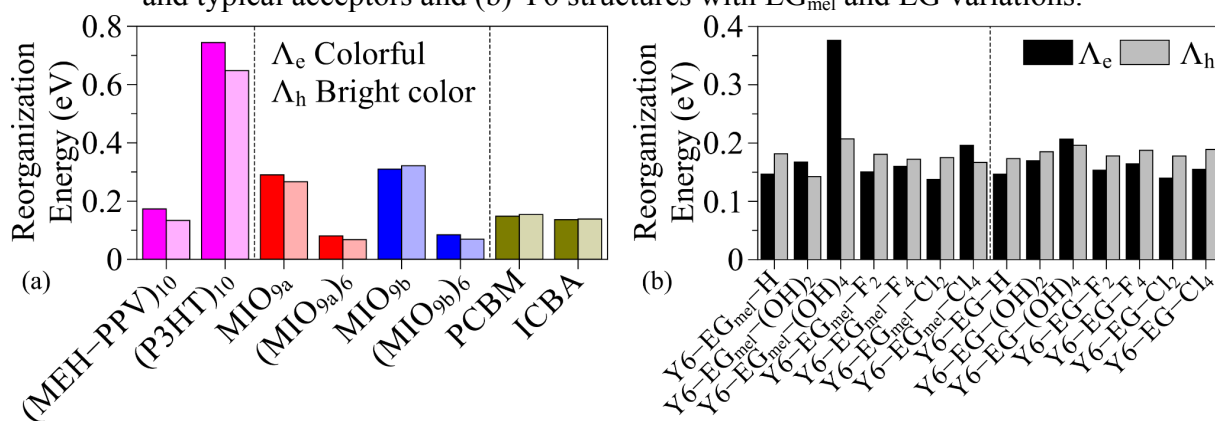
In terms of  $V_{OC}$ , the best result among the proposed Y6-EG<sub>mel</sub>-R<sub>n</sub>-based NFAs was obtained for (MIO<sub>9b</sub>)<sub>6</sub>:Y6-EG<sub>mel</sub>-H, followed by MIO<sub>9b</sub>:Y6-EG<sub>mel</sub>-H. For Y6-EG-R<sub>n</sub> based structures, higher values are obtained for (MIO<sub>9b</sub>)<sub>6</sub>:Y6-EG-(OH)<sub>4</sub> followed by

MIO<sub>9b</sub>:Y6-EG-(OH)<sub>4</sub>. Regarding heterogeneous NFAs, it is observed the following order (MIO<sub>9b</sub>)<sub>6</sub>:EG<sub>mel</sub>-Y6-EG-(OH)<sub>2</sub> > MIO<sub>9b</sub>:EG<sub>mel</sub>-Y6-EG-(OH)<sub>2</sub> > D18:EG<sub>mel</sub>-Y6-EG-F<sub>2</sub>.

It is worth noting that MIO<sub>9b</sub>-based compounds present promising performances as electron donors. The results obtained for eumelanin-based acceptors, indicate the need for systems with larger electronic gaps, and reduced  $\Delta E_{LL}$  to improve the  $V_{OC}$  values (detailed data are presented in Tables B4 and B5 in Appendix B). It is also interesting to note the good overall performance of typical high efficient D:A pairs (PM6:Y6-EG-F<sub>2</sub> and D18:Y6-EG-F<sub>2</sub>) for all the combinations of parameters.

Still regarding the performance of the systems, the internal reorganization energies ( $\Lambda$ ) of the structures were evaluated. Such parameters represent the energy required for geometric relaxation due to charge transfer processes and is inversely proportional to the mobility of charge carriers<sup>145</sup>. Such descriptors can also indicate the dominant charge transport mechanism within the systems: typically  $\Lambda_h < \Lambda_e$  in donor materials, where greater hole mobility is expected, while  $\Lambda_h > \Lambda_e$  is observed for acceptors. Figure 3.18 presents the estimated electron ( $\Lambda_e$ ) and hole ( $\Lambda_h$ ) reorganization energies for each compound.

**Figure 3.18** - Reorganization energy of: (a) Typical donors, compounds MIO<sub>9a</sub> and MIO<sub>9b</sub>, and typical acceptors and (b) Y6 structures with EG<sub>mel</sub> and EG variations.



Source: Author.

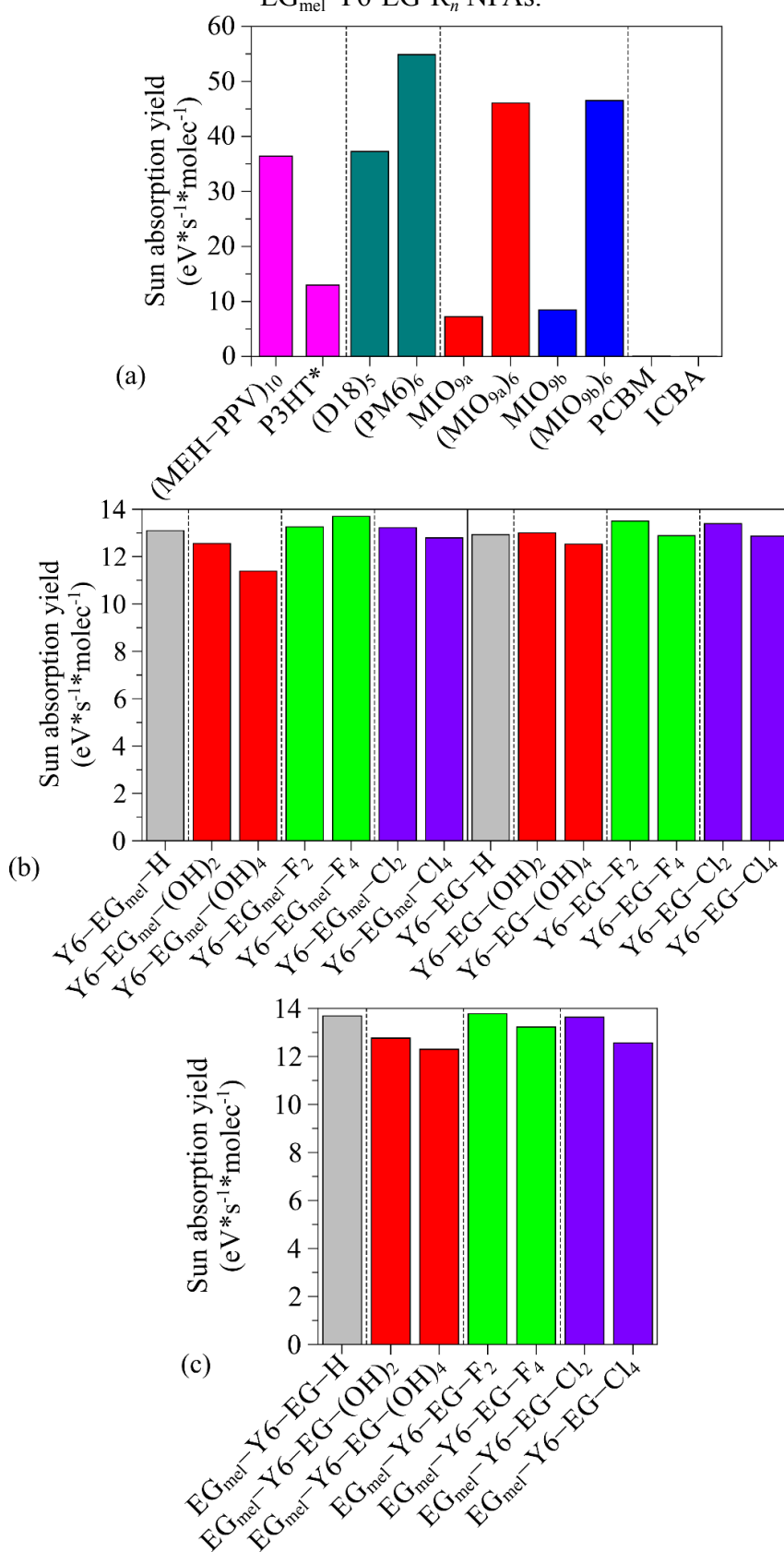
Note that most polymeric donors present reorganization energies smaller than 0.4 eV, except P3HT (which is compatible with values reported in the literature<sup>126,146</sup>). Even though donors are supposed to present  $\Lambda_h < \Lambda_e$ , an opposite effect is noticed for MIO<sub>9b</sub>, however with very close values. The reorganization energy tends to decrease as the oligomer size increases (see Figure B17a in Appendix B).

Low reorganization energies are observed for most of the proposed NFAs (< 0.25 eV), with higher values for R<sub>n</sub> = (OH)<sub>4</sub> in both structures. The high  $\Lambda_e$  value of Y6-EG<sub>mel</sub>-(OH)<sub>4</sub>

stands out from the others, being a clear outlier, so more in-depth studies are needed to find out the cause. In general, most Y6-based NFAs present  $\Lambda_e < \Lambda_h$ , except Y6-EG<sub>mel</sub>-(OH)<sub>2</sub>, Y6-EG<sub>mel</sub>-(OH)<sub>4</sub>, Y6-EG<sub>mel</sub>-Cl<sub>4</sub> and Y6-EG-(OH)<sub>4</sub>.

Finally, aiming to estimate the overall efficiency of sunlight absorption of the systems, a theoretical sun absorption yield parameter was estimated by the superposition of sun irradiance (direct+circumsolar solar irradiation <sup>147</sup>, Figure B18 in Appendix B) and gaussian convoluted theoretical optical absorption spectra of the molecules (Eq. 3.5). Figure 3.19 illustrates the results of typical donors, acceptors, MIOs, and proposed NFAs.

**Figure 3.19** - Solar absorption yield estimated for: (a) typical donors, fullerene-based acceptors and MIOs; (b) homogeneous Y6-EG<sub>mel</sub>-R<sub>n</sub> and Y6-EG-R<sub>n</sub> NFAs; (c) heterogeneous EG<sub>mel</sub>-Y6-EG-R<sub>n</sub> NFAs.



Source: Author.

Strong sun irradiation is commonly observed from 435 up to 790 nm with the maximum around 536 nm<sup>147</sup>. Within this range, however, some irradiation gaps are observed due to atmosphere absorption/reflection, leading to absorption yield decrease in some compounds. For donors, the highest yields are noted for (PM6)<sub>6</sub>, followed by (MIO<sub>9b</sub>)<sub>6</sub>/(MIO<sub>9a</sub>)<sub>6</sub>, (D18)<sub>5</sub> and (MEH-PPV)<sub>10</sub>. For homogeneous symmetric NFAs it is noticed the following decreasing order: Y6-EG<sub>mel</sub>-F<sub>4</sub> > Y6-EG-F<sub>2</sub> > Y6-EG-Cl<sub>2</sub> > Y6-EG<sub>mel</sub>-F<sub>2</sub> > Y6-EG<sub>mel</sub>-Cl<sub>2</sub> > Y6-EG<sub>mel</sub>-H > Y6-EG-(OH)<sub>2</sub> > Y6-EG-H > Y6-EG-F<sub>4</sub> > Y6-EG-Cl<sub>4</sub> > Y6-EG<sub>mel</sub>-Cl<sub>4</sub> > Y6-EG<sub>mel</sub>-(OH)<sub>2</sub> > Y6-EG-(OH)<sub>4</sub> > Y6-EG<sub>mel</sub>-(OH)<sub>4</sub>. Regarding heterogeneous asymmetric compounds EG<sub>mel</sub>-Y6-EG-F<sub>2</sub> has the best absorption yield followed by EG<sub>mel</sub>-Y6-EG-H, EG<sub>mel</sub>-Y6-EG-Cl<sub>2</sub>, EG<sub>mel</sub>-Y6<sub>trad</sub>-EG-F<sub>4</sub>, EG<sub>mel</sub>-Y6-EG-(OH)<sub>2</sub>, EG<sub>mel</sub>-Y6-EG-Cl<sub>4</sub> and EG<sub>mel</sub>-Y6-EG-(OH)<sub>4</sub>. Generally, heterogeneous structures present higher absorption yields than the homogeneous ones.

It is also important to highlight that, despite their broad spectral absorption, the absolute absorption yields of the Y6-EG<sub>mel</sub>-R<sub>n</sub> structures are one order of magnitude lower than those of the donor compounds, typically around 14 eV·s<sup>-1</sup>·molecule<sup>-1</sup> (similarly to the other NFAs, including Y6), compared to 45-55 eV·s<sup>-1</sup>·molecule<sup>-1</sup> for donor materials such as PM6 and MIO<sub>9b</sub>.

Given the complementary absorption spectra of Y6-based compounds (see Fig. 3.7) additional performance analyses were conducted for clusters based on dimeric homogeneous systems. Significant improvements were observed for Y6-EG Y6-EG<sub>mel</sub>-H and Y6-EG Y6-EG<sub>mel</sub>-Cl<sub>2</sub> clusters, suggesting that a blend of melanin and non-melanin-based NFAs can lead to good optical performances (see Figure B20 in Appendix B for details).

In summary, our results demonstrate the potential of Y6-EG<sub>mel</sub>-R<sub>n</sub> and Y6-EG-R<sub>n</sub> as electron acceptors in OSC, particularly with specific EGs. DAM maps showed improvements in Y6-EG<sub>mel</sub>-Cl<sub>4</sub> and EG<sub>mel</sub>-Y6-EG-Cl<sub>4</sub> structures compared to the conventional Y6-EG-F<sub>2</sub> structure. On average, Y6-EG<sub>mel</sub> exhibited a higher HOMO and LUMO overlap than Y6-EG, resulting in lower exciton binding energies. For reactivity, Y6-EG<sub>mel</sub> does not differ strongly from Y6-EG; however, heterogeneous structures exhibit an asymmetrical reactivity, particularly in relation to  $f^-$ . Y6-EG<sub>mel</sub>-F<sub>4</sub> and EG<sub>mel</sub>-Y6-EG-F<sub>2</sub> showed the highest solar irradiation absorption efficiencies among the homogeneous compounds. All the Y6-based structures present low relative reorganization energies, which is a desirable feature. In terms of V<sub>OC</sub>, the best results were obtained for (MIO<sub>9b</sub>)<sub>m</sub> based pairs (for  $m = 1$  or  $6$ ), in particular (MIO<sub>9b</sub>)<sub>m</sub>:Y6-EG<sub>mel</sub>-H, (MIO<sub>9b</sub>)<sub>m</sub>:Y6-EG-(OH)<sub>4</sub>, (MIO<sub>9b</sub>)<sub>m</sub>:EG<sub>mel</sub>-Y6-EG-(OH)<sub>2</sub>, indicating MIO<sub>9b</sub>-based systems as promising D materials for the proposed NFAs. It is important to

highlight that, while Y6-EG<sub>mel</sub>-R<sub>n</sub> derivatives show great potential as NFAs, the identification of more compatible donor materials remains essential for optimizing their performance.

### 3.5 Conclusions

This study presented a comprehensive theoretical investigation into the modification of Y6-based NFAs by: (i) functionalized melanin-based end groups (EG<sub>mel</sub>-R<sub>n</sub>) and (ii) modified traditional end groups (EG-R<sub>n</sub>) for potential applications in organic solar cells. The applicability of melanin-based donors, MIO<sub>9b</sub> and MIO<sub>9b</sub>, were also investigated.

Modification of a DHICA into the EG<sub>mel</sub>-(OH)<sub>2</sub> evidence the tuning of the frontier energy levels, electronic gaps, and optical absorption spectra, leading to properties that are similar to traditional EGs.

Isolated modified EG<sub>mel</sub> and typical EGs showed similar electronic behaviors, especially regarding the addition of several functional groups (e.g., H, OH, F, Cl), which affected key properties such as electron donation and acceptance. Notably, OH substitutions enhanced electron donation, while F and Cl favored electron acceptance. These modifications significantly influenced performance parameters, including the energy gaps and exciton binding energies.

Among the Y6-derived structures, Y6-EG<sub>mel</sub> (both homogeneous and heterogeneous) exhibited promising performance as acceptors, with functional groups playing a critical role in optimizing electronic properties and performance. The incorporation of halogens improved the electron acceptance power, reduced the electronic gaps (bathochromic effects on optical absorption), and increased the  $\Delta E_{LL}$  and  $\Delta E_{HH}$  parameters. Hydroxyl groups induced opposite effects, which are sensitive to the number of ligands (more intense effects for larger  $n$ ). Some hydroxyl modifications (OH)<sub>n</sub> were detrimental to device performance, leading to a number of non-functional donor-acceptor pairs.

It has been shown the potential of MIO-based systems to act as electron donors in such NFAs-based OSCs (MIO<sub>9b</sub> consistently outperformed MIO<sub>9a</sub>), presenting high predicted  $V_{OC}$ , good FMOs energy levels alignments, and reduced reorganization energies. However, further optimization of donors is needed to fully complement melanin-based acceptors.

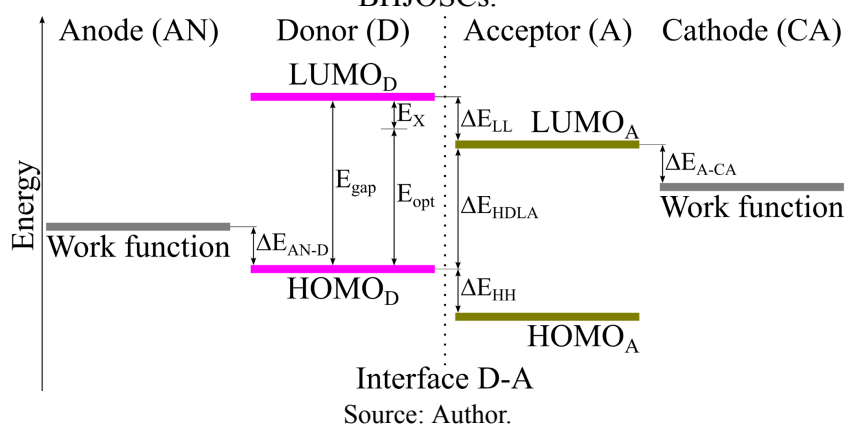
In summary, this study underscores the versatility of melanin-derived structures in organic solar cell applications, offering a foundation for tuning electronic and optical properties through strategic functional group modifications. The results highlight the promising potential of melanin-based materials in advancing sustainable energy technologies.

## APPENDIX B – DFT-Guided Design of Melanin-Inspired Materials for High-Performance Organic Solar Cells

### B1. Theoretical parameters relevant to the BHJOSCs performance

To establish a foundational understanding of the electronic features that govern the performance of bulk-heterojunction organic solar cells (BHJOSCs), it is necessary to evaluate the alignment of frontier molecular orbitals (FMOs) for donor and acceptor compounds, as well as the work function of the electrodes. These parameters are critical for predicting charge transfer efficiency, exciton dissociation potential, and energy level compatibility between materials. The key parameters are illustrated in Figure B1.

**Figure B1** - FMOs alignments and relevant parameters associated with the performance of BHJOSCs.



$\Delta E_{LL}$  ( $\Delta E_{HH}$ ) represents the energy difference between the LUMO (HOMO) levels of the donor and acceptor materials, which indicates the likelihood of exciton dissociation (recombination).  $\Delta E_{gap}$  refers to the electronic gap of the donor material, associated with its optical absorption capability and exciton binding energy ( $E_{gap} = E_{opt} + E_X$ ).  $\Delta E_{HDLA}$  denotes the energy difference between the LUMO of the acceptor and the HOMO of the donor, which is proportional to the open-circuit voltage ( $V_{OC}$ ) of the system. Finally,  $\Delta E_{AN-D}$  and  $\Delta E_{A-CA}$  describe the energy offset between the donor's HOMO and the anode work function, and between the acceptor's LUMO and the cathode work function, respectively.

$V_{OC}$  is the maximum voltage a photovoltaic device can deliver to a load under specific radiation and temperature conditions. In bulk heterojunction organic solar cells (BHJ-OSCs), it can be estimated using the expression  $e.V_{OC} = (\Delta E_{HDLA}) - 0.3$ , where 0.3 eV typically

corresponds to the exciton binding energy in organic materials, indicating that a higher  $\Delta E_{\text{HDLA}}$  leads to a higher  $V_{\text{OC}}$  value<sup>14</sup>.

## B2. Opto-electronic properties of oligomeric donor systems and traditional fullerene-based acceptors

Table B1 summarizes opto-electronic properties of oligomeric donor systems and traditional fullerene-based acceptors. As can be seen the theoretical results present a reasonable agreement with the literature<sup>11,148–153</sup>. Greater deviations were observed for P3HT values resulting in larger electronic gaps and exciton dissociation energies<sup>139,154–157</sup>.

**Table B1** - Summary of opto-electronic properties of compounds.

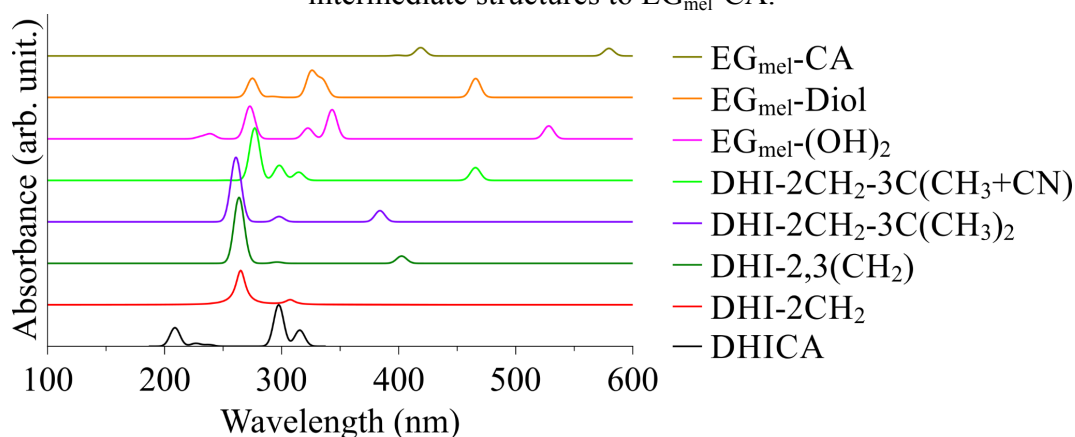
<b>Compound</b>	<b>E<sub>HOMO</sub> (eV)</b>	<b>E<sub>LUMO</sub> (eV)</b>	<b>E<sub>gap</sub> (eV)</b>	<b>E<sub>opt</sub> (eV)</b>	<b>E<sub>x</sub>(eV)</b>
(MEH-PPV) <sub>10</sub>	-4.447	-2.068	2.379	2.043	0.336
(P3HT) <sub>10</sub>	-5.523	-1.953	3.570	3.059	0.511
(D18) <sub>5</sub>	-5.369	-2.551	2.818	2.443	0.375
(PM6) <sub>6</sub>	-5.161	-2.953	2.208	1.859	0.349
MIO <sub>9a</sub>	-5.360	-2.160	3.190	2.940	0.250
(MIO <sub>9a</sub> ) <sub>6</sub>	-5.130	-2.656	2.474	2.135	0.338
MIO <sub>9b</sub>	-5.080	-1.920	3.170	2.900	0.270
(MIO <sub>9b</sub> ) <sub>6</sub>	-5.087	-2.634	2.453	2.129	0.324
ICBA	-5.746	-3.324	2.422	1.783	0.640
PCBM	-6.047	-3.502	2.544	1.912	0.632

Source: Author.

### B3. Theoretical optical absorption spectra of typical donors, acceptors and Y6 clusters

To pre-estimate the potential impact of these end groups (EGs) on the optical properties of NFAs, the theoretical optical absorption spectra of the isolated groups were evaluated, as shown in Figure B2.

**Figure B2** - Theoretical optical absorption spectra of melanin-based compounds DHICA and intermediate structures to EG<sub>mel</sub>-CA.

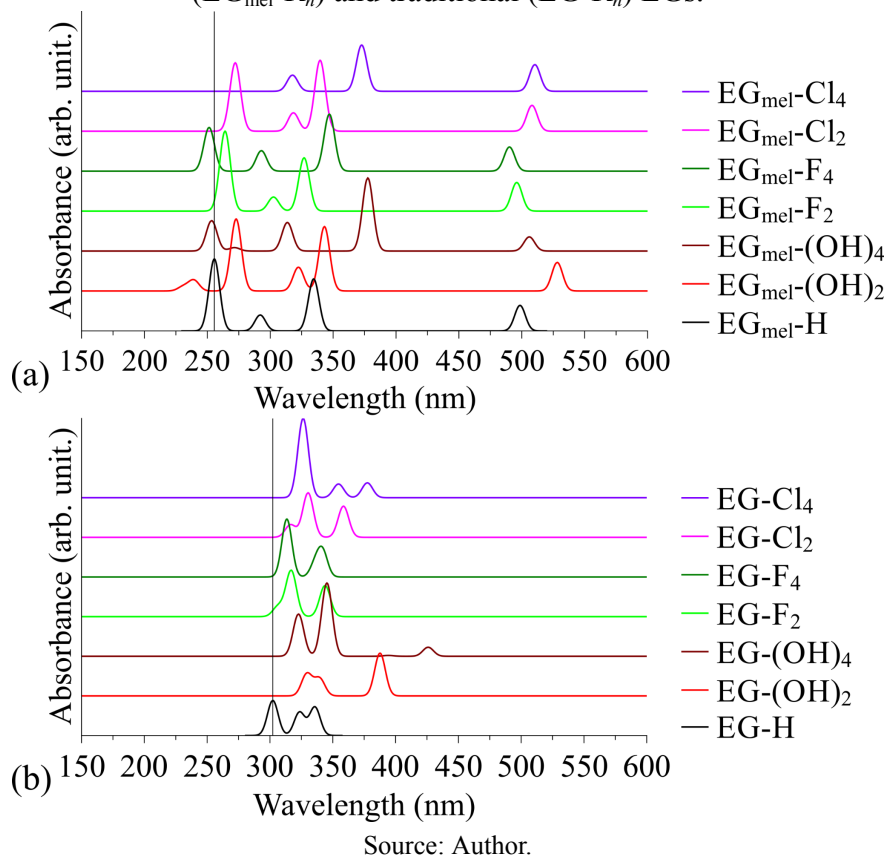


Source: Author.

Significant changes on the optical absorption spectra (compared to DHICA) are noticed due to the chemical modifications. Additional low-intensity peaks appear at higher wavelengths, which can be attributed to a reduction in the bandgap (Figure 3.4). Notably, the optical response of the derivatives DHI-2,3(CH)<sub>2</sub>, DHI-2CH<sub>2</sub>-3C(CH<sub>3</sub>)<sub>2</sub>, EG<sub>mel</sub>-(OH)<sub>2</sub> and EG<sub>mel</sub>-Diol is particularly interesting, as they exhibit increased absorbance in the visible region, albeit with lower intensity.

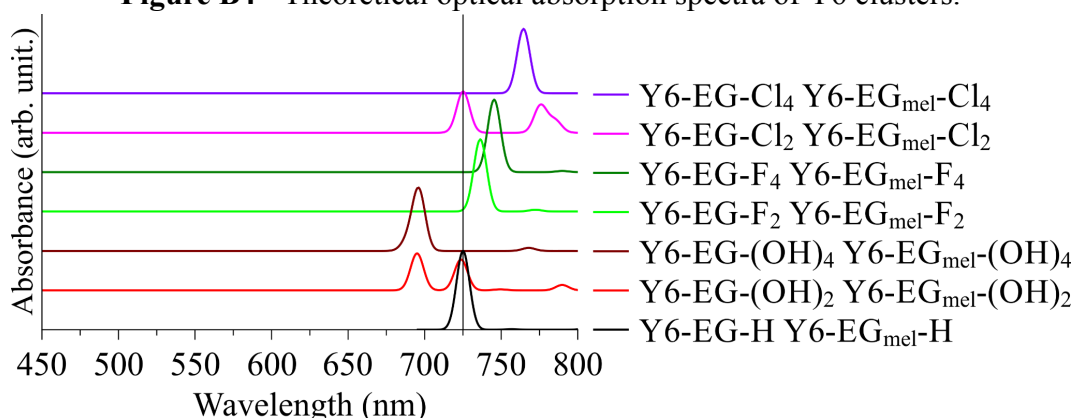
Figure B3 illustrates the theoretical optical absorption spectra estimated for EG<sub>mel</sub>-R<sub>n</sub> and EG-R<sub>n</sub> structures (normalized in relation to derivatives with R = H).

**Figure B3** - Theoretical optical absorption spectra estimated for eumelanin-inspired ( $EG_{mel}-R_n$ ) and traditional ( $EG-R_n$ ) EGs.



Melanin-inspired compounds exhibit a significant optical response in the visible range, with absorption peaks around 375 and 500 nm, which are absent in traditional EGs. Notably, the peak around 500 nm persists even when  $R = H$ . Bathochromic shifts are observed for this peak due to  $(OH)_n$  and  $Cl_n$  insertion, while hypsochromic shifts occur for  $F_n$ . The presence of additional halogens enhances the peak's intensity, whereas  $(OH)_4$  reduces it. Strong absorption around 400 nm is noted for  $EG_{mel}-(OH)_4$ ,  $EG_{mel}-Cl_4$ , and  $EG-(OH)_2$ .

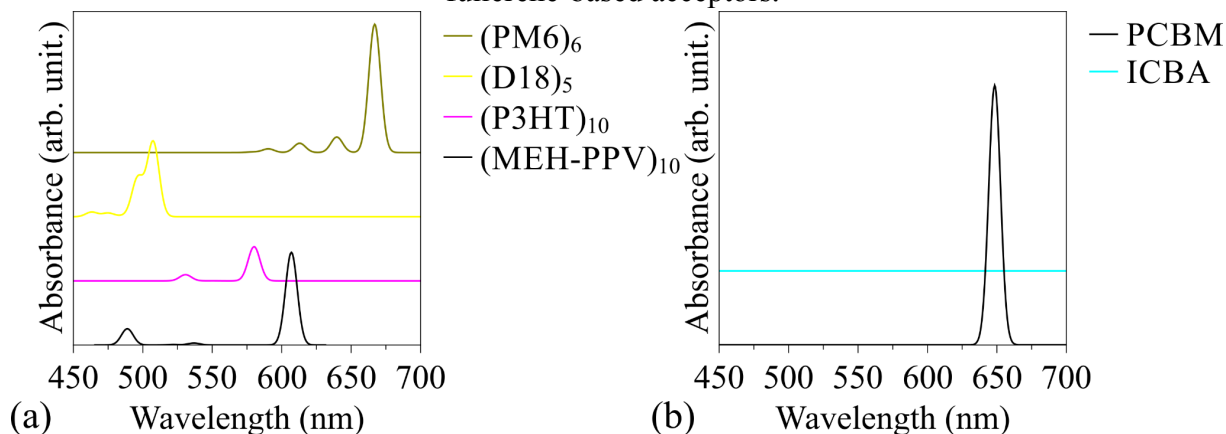
Figure B4 shows the theoretical optical absorption spectra of the Y6 cluster formed by two Y6 with  $EG_{mel}-R_n$  and  $EG-R_n$  type with the same quantity and type of functional groups ( $R_n$ ) like H, OH, F and Cl.

**Figure B4** - Theoretical optical absorption spectra of Y6 clusters.

Source: Author.

The cluster systems with  $(\text{OH})_n$  exhibit a red shift when compared to Y6-EG-H Y6-EG<sub>mel</sub>-H while the system with halogens exhibit a blue-shift. The Y6-EG-(OH)<sub>2</sub> Y6-EG<sub>mel</sub>-(OH)<sub>2</sub> and Y6-EG-Cl<sub>2</sub> Y6-EG<sub>mel</sub>-Cl<sub>2</sub> display new large peaks, close to 725 and 765 nm respectively. In summary the results suggest that the cluster systems present an effective absorption range between 695 and 765 nm.

Figure B5 shows the optical absorption spectra of the typical donors and acceptors.

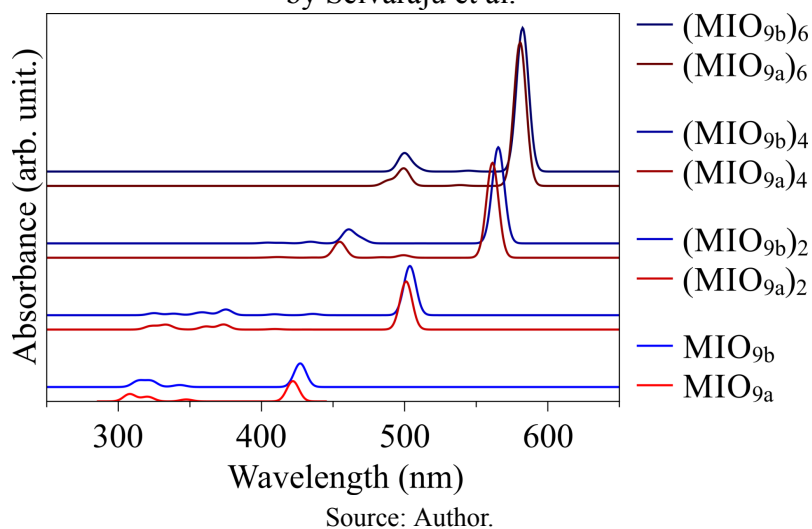
**Figure B5** - Theoretical optical absorption spectra of (a) typical donor polymers and (b) fullerene-based acceptors.

Source: Author.

Typical donors present optical absorption from 475 up to 675 nm, while PCBM presents a very weak peak around 650 nm. The ICBA does not show absorption in this range. The intensity of absorbance was normalized by the higher peak of each figure showing the strongest absorbance from the PM6 and the weaker from the P3HT.

Figure B6 shows the optical absorption spectra of the eumelanin-based oligomeric structures  $\text{MIO}_{9a}$  and  $\text{MIO}_{9b}$ , as well as its evolution with the main chain increase. All the spectra were normalized in relation to the more intense peak, obtained for  $(\text{MIO}_{9b})_6$ .

**Figure B6** - Theoretical optical absorption spectra of (a) eumelanin-based polymer proposed by Selvaraju et al. <sup>7</sup>

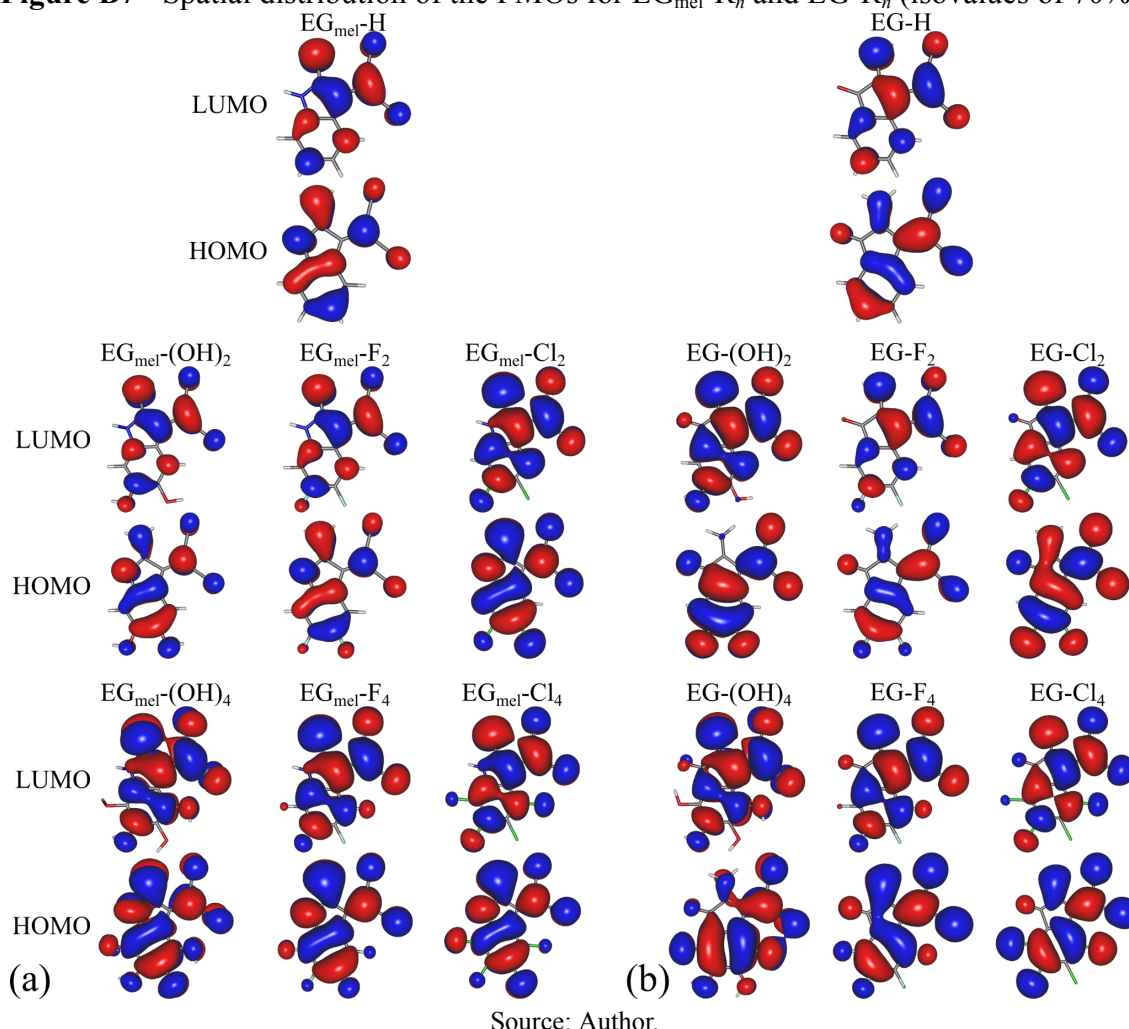


Notably, the  $\text{MIO}_{9a}$  and  $\text{MIO}_{9b}$  compounds exhibit strong absorption in the visible and near infrared range <sup>7</sup>, complementing non-fullerene acceptors; chain elongation results in a red shift and enhances their effective light absorption into the visible range.

#### B4. Spatial overlap and distribution of Kohn-Sham frontier molecular orbitals

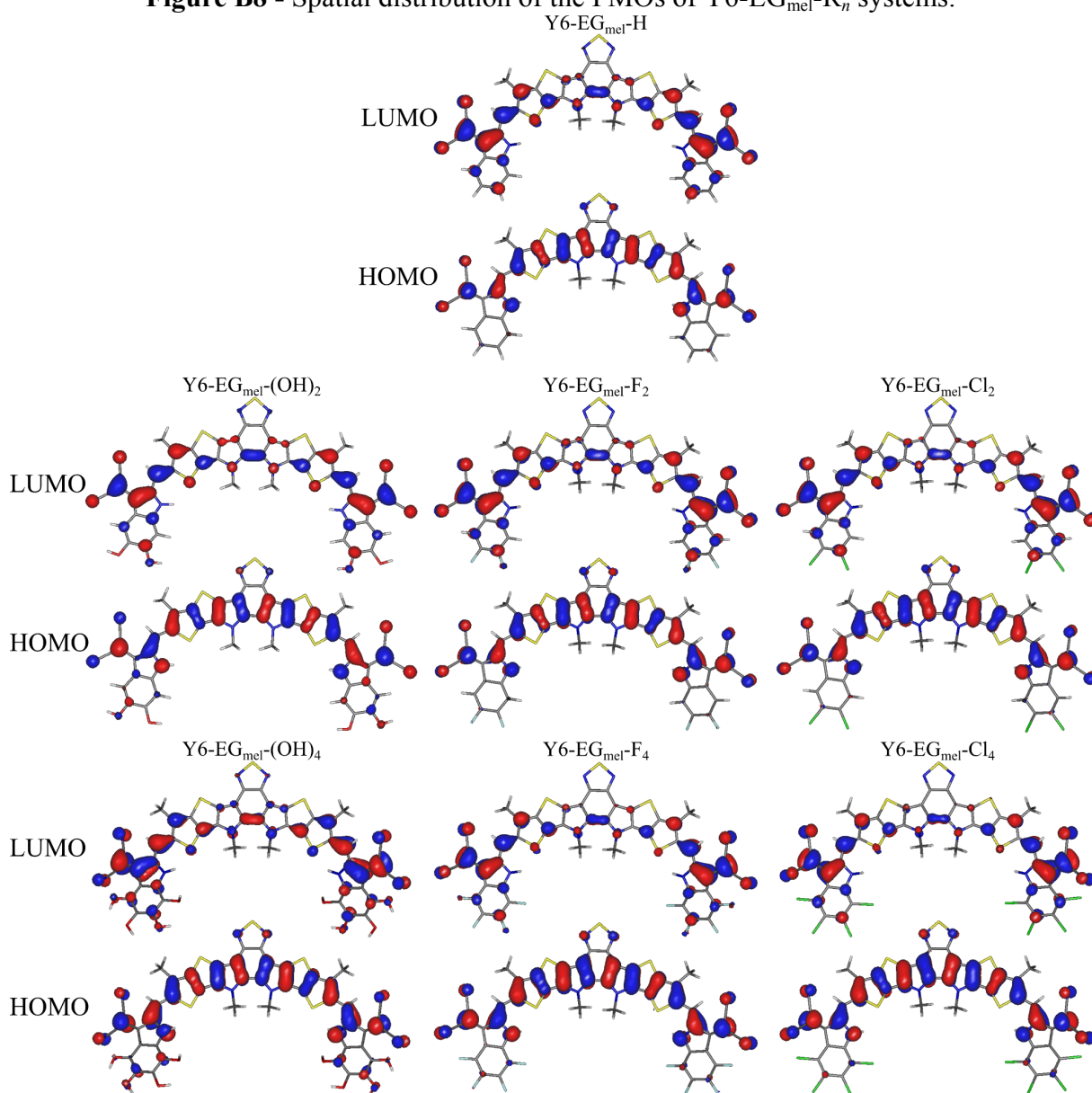
Figure B7 summarizes the spatial distributions of the FMOs for  $\text{EG}_{\text{mel}}\text{-R}_n$  and  $\text{EG-R}_n$ .

**Figure B7** - Spatial distribution of the FMOs for  $\text{EG}_{\text{mel}}\text{-R}_n$  and  $\text{EG-R}_n$  (isovalues of 70%).

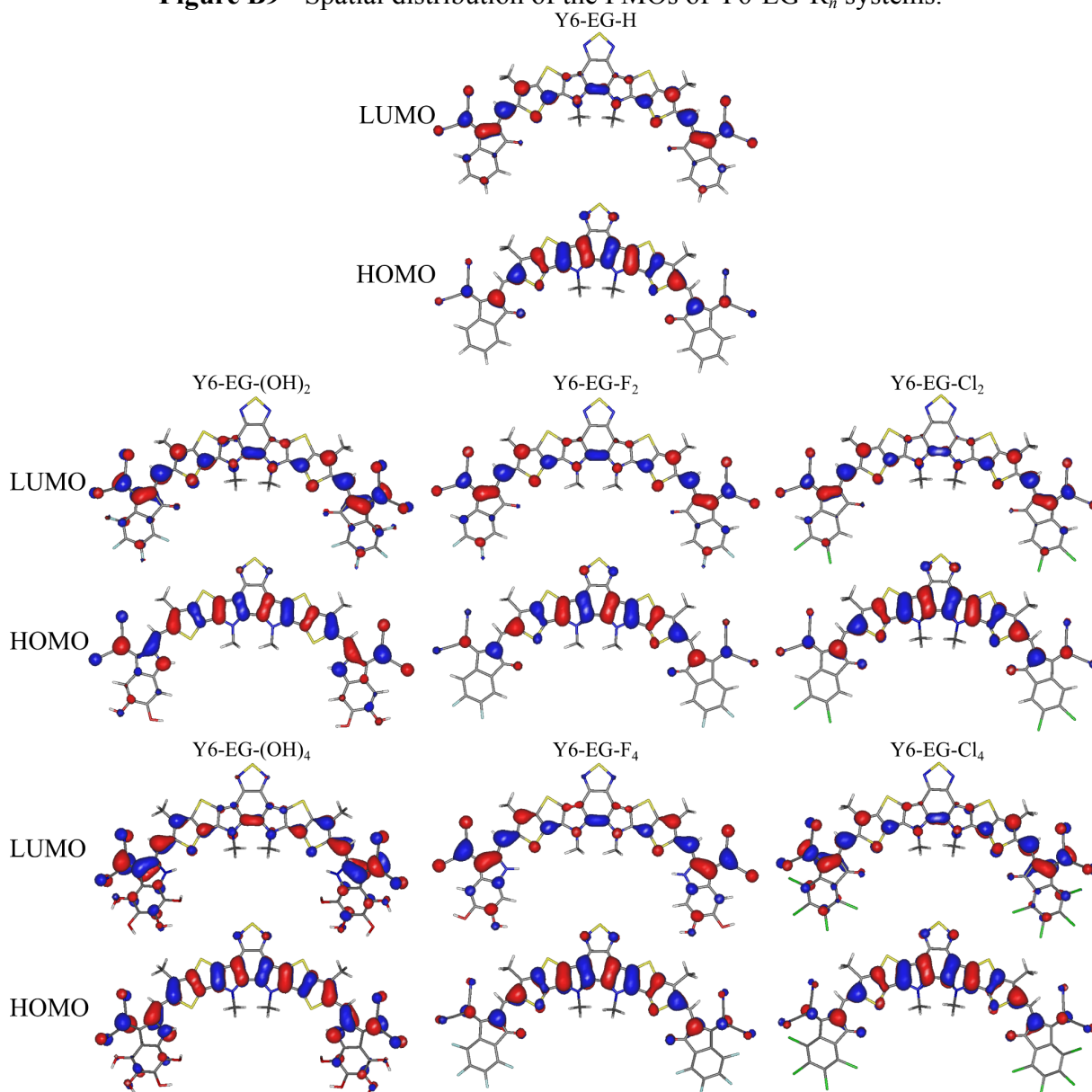


Note that both, HOMO and LUMO spatial distributions of  $\text{EG}_{\text{mel}}\text{-R}_n$ , remain largely unaffected by chemical modifications. In contrast,  $\text{EG-R}_n$  exhibits noticeable sensitivity in HOMO symmetry upon the insertion of hydroxyls, halogens, and variations in the number of substituents. While the LUMO distributions of  $\text{EG}_{\text{mel}}\text{-R}_n$  and  $\text{EG-R}_n$  are generally similar, significant differences arise in their HOMO structures. Notably, the  $\text{C}^3\text{-C(CN)}_2$  unit plays a crucial role in the composition of the FMOs for all the systems.

Figures B8 and B9 summarize the FMOs spatial distributions of  $\text{Y6-EG}_{\text{mel}}\text{-R}_n$ ,  $\text{Y6-EG-R}_n$  homogeneous structures and  $\text{EG}_{\text{mel}}\text{-Y6-EG-R}_n$  heterogeneous ones.

**Figure B8** - Spatial distribution of the FMOs of Y6-EG<sub>mel</sub>-R<sub>n</sub> systems.

Source: Author.

**Figure B9** - Spatial distribution of the FMOs of Y6-EG- $R_n$  systems.

Source: Author.

Homogeneous symmetric Y6-EG<sub>mel</sub>- $R_n$  and Y6-EG- $R_n$  structures (Figures S8 and S9 respectively) present a uniform spatial distribution of the FMOs on the Y6<sub>core</sub>, with the LUMO primarily situated on the EGs. It is noticed the influence of hydroxyls on the HOMO composition, shifting this orbital to carbons 5, 7, and 9. Small, similar effects are noticed for  $R_n = F_4$  and  $Cl_4$ . The strong orbital overlap reduces the exciton binding energy and enhances charge mobility by promoting greater delocalization of the frontier molecular orbitals along the acceptor structure.

Tables B2 and B3 present the spatial HOMO-LUMO overlap of homogeneous and heterogeneous Y6-based structures.

**Table B2** - Spatial H-L overlap rate of Y6-based homogeneous structures.

<b>Compound</b>	<b>Spatial overlap matrix <math>\langle  i  j  \rangle</math> (%)</b>
Y6-EG <sub>mel</sub> -H	71.58
Y6-EG <sub>mel</sub> -(OH) <sub>2</sub>	73.76
Y6-EG <sub>mel</sub> -(OH) <sub>4</sub>	72.16
Y6-EG <sub>mel</sub> -F <sub>2</sub>	70.76
Y6-EG <sub>mel</sub> -F <sub>4</sub>	69.91
Y6-EG <sub>mel</sub> -Cl <sub>2</sub>	70.20
Y6-EG <sub>mel</sub> -Cl <sub>4</sub>	69.08
Y6-EG-H	67.29
Y6-EG-(OH) <sub>2</sub>	67.07
Y6-EG-(OH) <sub>4</sub>	67.42
Y6-EG-F <sub>2</sub>	67.06
Y6-EG-F <sub>4</sub>	65.95
Y6-EG-Cl <sub>2</sub>	66.76
Y6-EG-Cl <sub>4</sub>	65.12

Source: Author.

**Table B3** - Spatial H-L overlap rate of Y6-based heterogeneous structures and clusters.

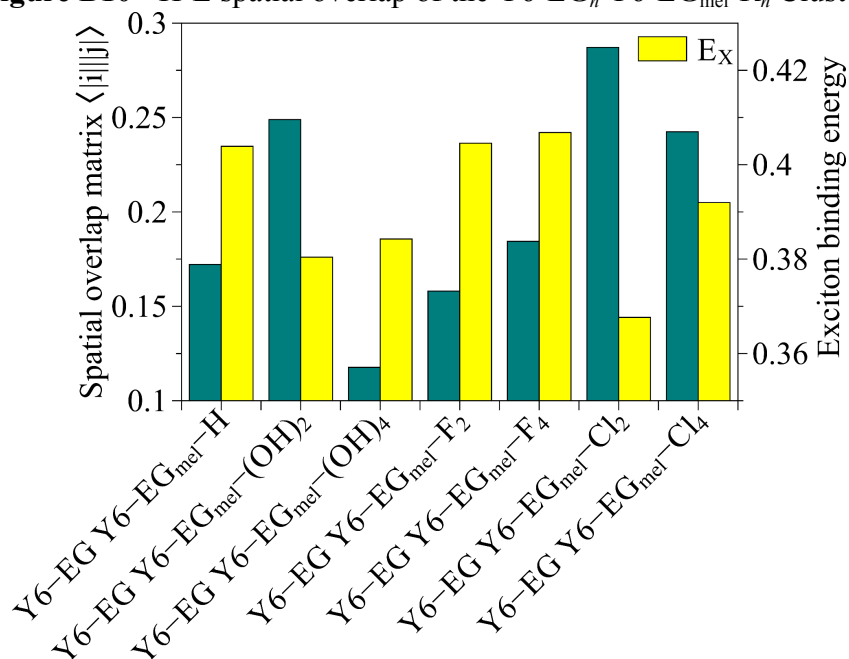
<b>Compound</b>	<b>Spatial overlap matrix <math>\langle  i  j  \rangle</math> (%)</b>
EG <sub>mel</sub> -Y6-EG-H	68.04
EG <sub>mel</sub> -Y6-EG-(OH) <sub>2</sub>	67.00
EG <sub>mel</sub> -Y6-EG-(OH) <sub>4</sub>	68.35
EG <sub>mel</sub> -Y6-EG-F <sub>2</sub>	67.97
EG <sub>mel</sub> -Y6-EG-F <sub>4</sub>	68.76
EG <sub>mel</sub> -Y6-EG-Cl <sub>2</sub>	68.31
EG <sub>mel</sub> -Y6-EG-Cl <sub>4</sub>	68.62
Y6-EG-H Y6-EG <sub>mel</sub> -H	17.22
Y6-EG-(OH) <sub>2</sub> Y6-EG <sub>mel</sub> -(OH) <sub>2</sub>	24.89
Y6-EG-(OH) <sub>4</sub> Y6-EG <sub>mel</sub> -(OH) <sub>4</sub>	11.77
Y6-EG-F <sub>2</sub> Y6-EG <sub>mel</sub> -F <sub>2</sub>	15.80
Y6-EG-F <sub>4</sub> Y6-EG <sub>mel</sub> -F <sub>4</sub>	18.44
Y6-EG-Cl <sub>2</sub> Y6-EG <sub>mel</sub> -Cl <sub>2</sub>	28.72
Y6-EG-Cl <sub>4</sub> Y6-EG <sub>mel</sub> -Cl <sub>4</sub>	24.25

Source: Author.

Tables B2 and B3 mainly show that the average H-L overlap of  $Y6-EG_{mel}-R_n > EG_{mel}-Y6-EG-R_n > Y6-EG-R_n > Y6$  clusters. The smallest overlap was obtained for  $Y6-EG-Cl_4$ , with 65.12 %, which is still an appreciable overlap.

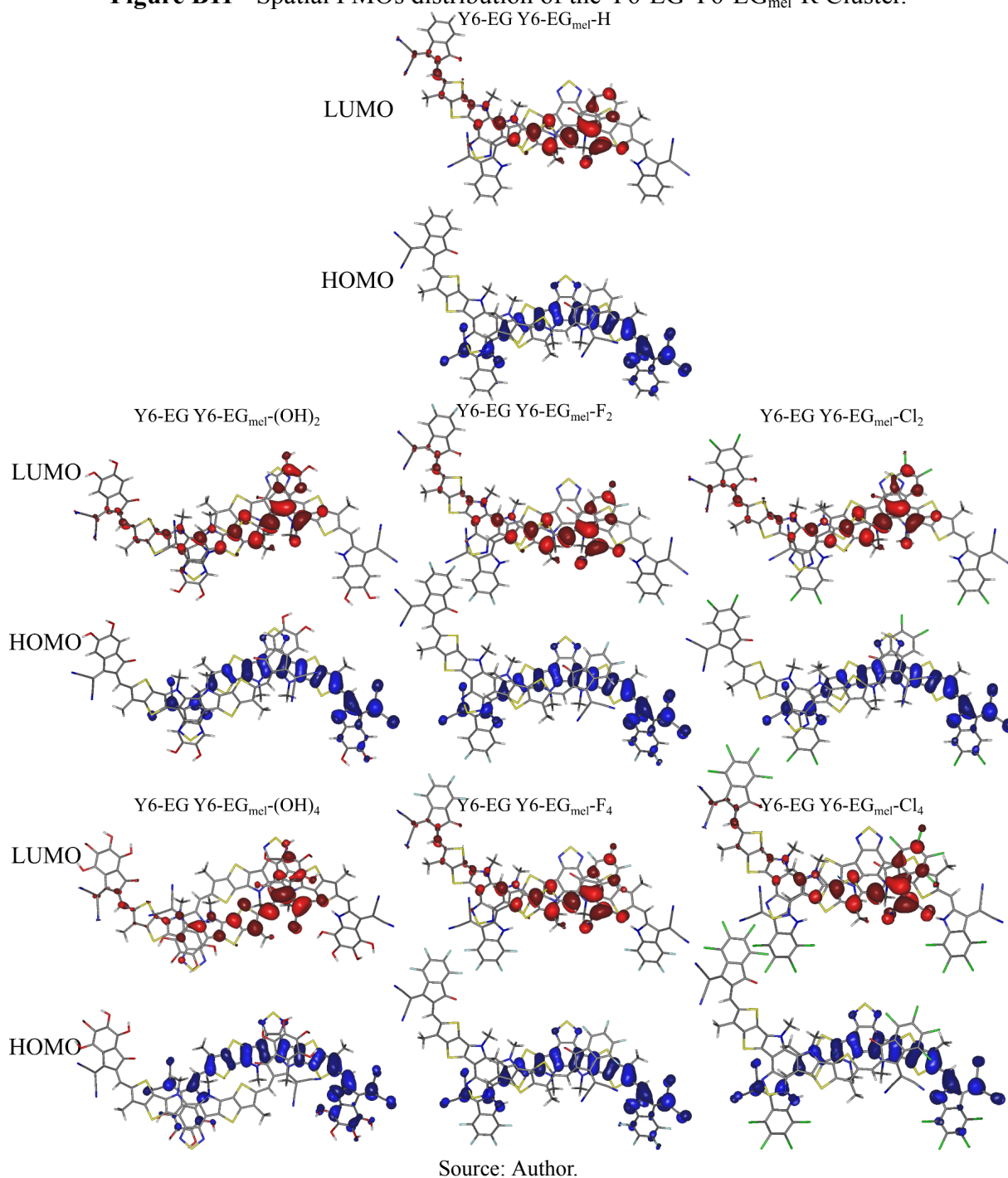
Figure B10 shows the H-L spatial overlap (green columns) and the Exciton binding energy (yellow columns), Figure B11 shows the Spatial distribution of Kohn-Sham frontier molecular orbitals of the Y6 cluster. The orbitals of  $Y6-EG_{mel}-R_n$  are shown in blue and those of  $Y6-EG-R_n$  in red.

**Figure B10** - H-L spatial overlap of the  $Y6-EG_n$   $Y6-EG_{mel}-R_n$  Cluster.



Source: Author.

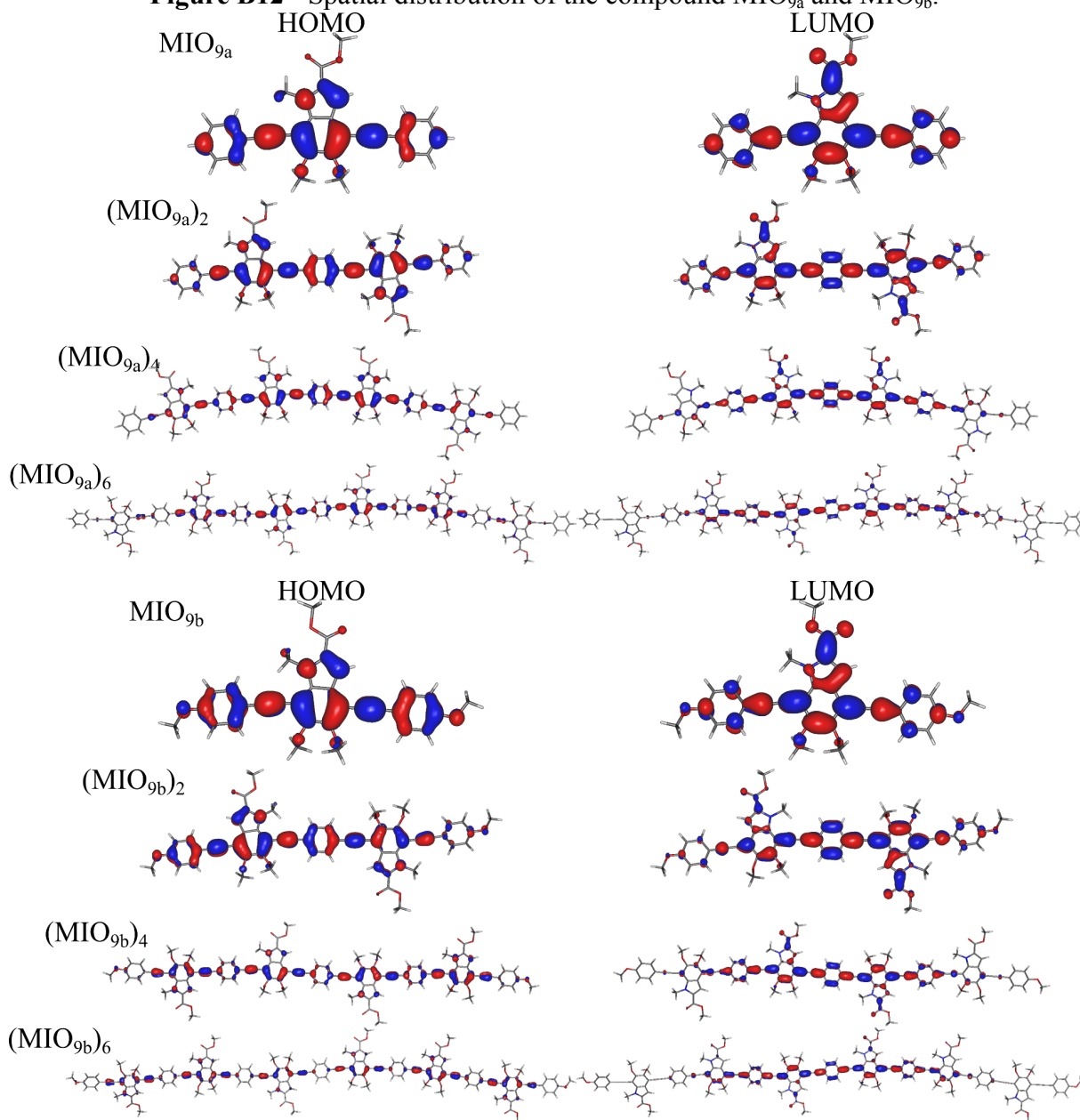
Figure B10 shows that the clusters had an H-L overlap smaller than 30% and exciton binding energies of up to ~0.41 eV.

**Figure B11** - Spatial FMOs distribution of the Y6-EG Y6-EG<sub>mel</sub>-R Cluster.

Note that the HOMO is mainly centered over Y6-EG<sub>mel</sub>-R<sub>n</sub>, while the LUMO is located over Y6-EG-R<sub>n</sub>, preferably at the stacked region. FMO spatial distributions are similar for the distinct functional groups.

Figure B12 shows the spatial distribution of FMOs obtained for oligomeric structures of MIO<sub>9a</sub> and MIO<sub>9b</sub>.

**Figure B12** - Spatial distribution of the compound MIO<sub>9a</sub> and MIO<sub>9b</sub>.



Source: Author.

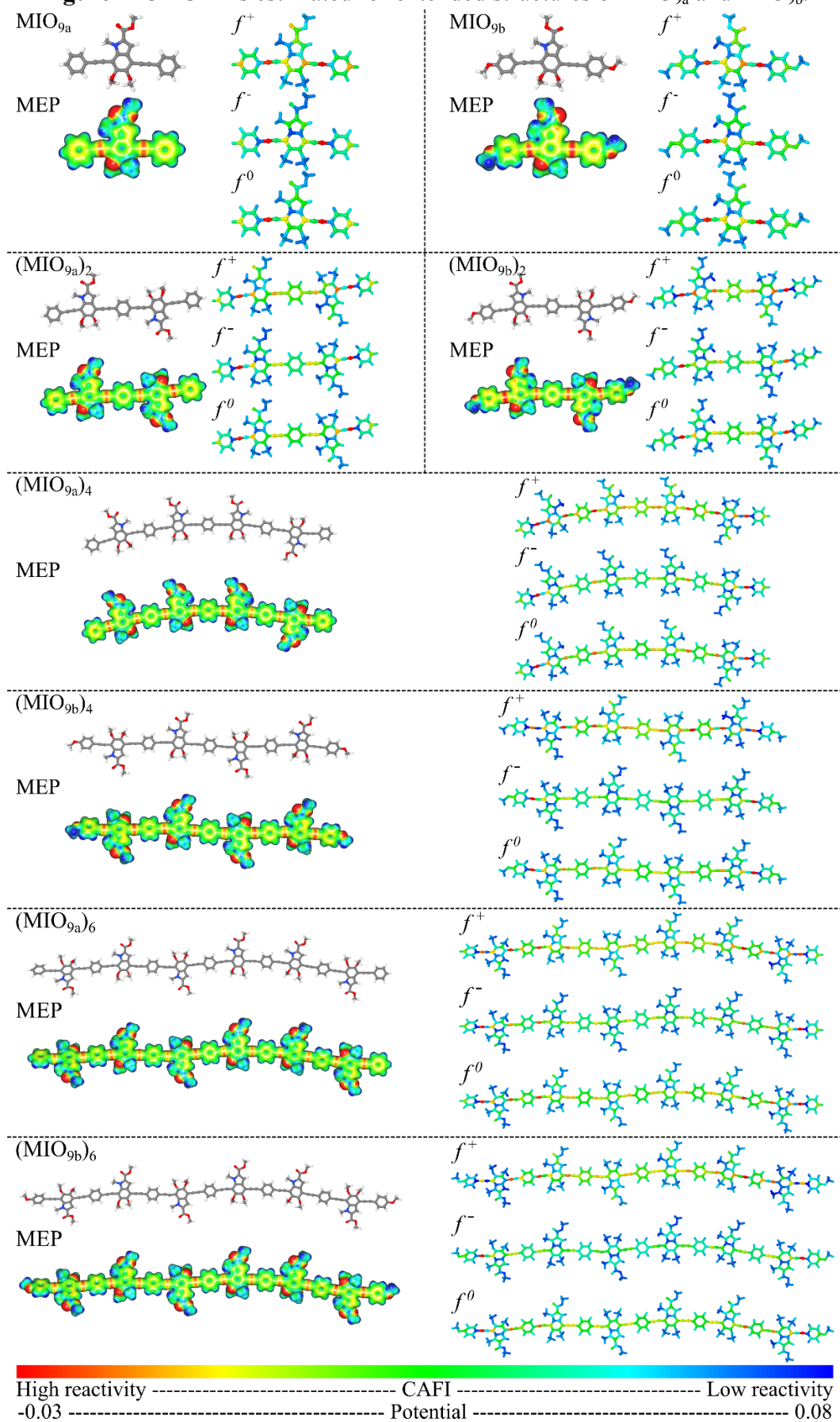
As shown in Figure B12, the HOMO of these compounds are evenly distributed across the entire structure, while the LUMOs are mainly concentrated at the center of the oligomeric chains. As the main chain length increases, a reduction in H-L overlap is observed, especially in the MIO<sub>9b</sub> structures.

### **B5. Condensed to atom Fukui indexes and MEP: extended MIOs**

To gain further insight into the electronic reactivity of the studied materials, condensed-to-atom Fukui indexes (CAFI) and molecular electrostatic potential (MEP) maps were computed for both monomeric and oligomeric structures of MIO<sub>9a</sub> and MIO<sub>9b</sub>. These descriptors are valuable for identifying regions prone to electrophilic or nucleophilic attack, as well as for visualizing charge distribution across the molecule. The results are presented in Figure B13, where both CAFI and MEP values are displayed using RGB color scales: for the CAFI maps, red indicates regions of higher chemical reactivity and blue corresponds to lower reactivity; in the MEP maps, red denotes areas of higher electronegativity (electron-rich regions), while blue highlights zones of lower electronegativity.

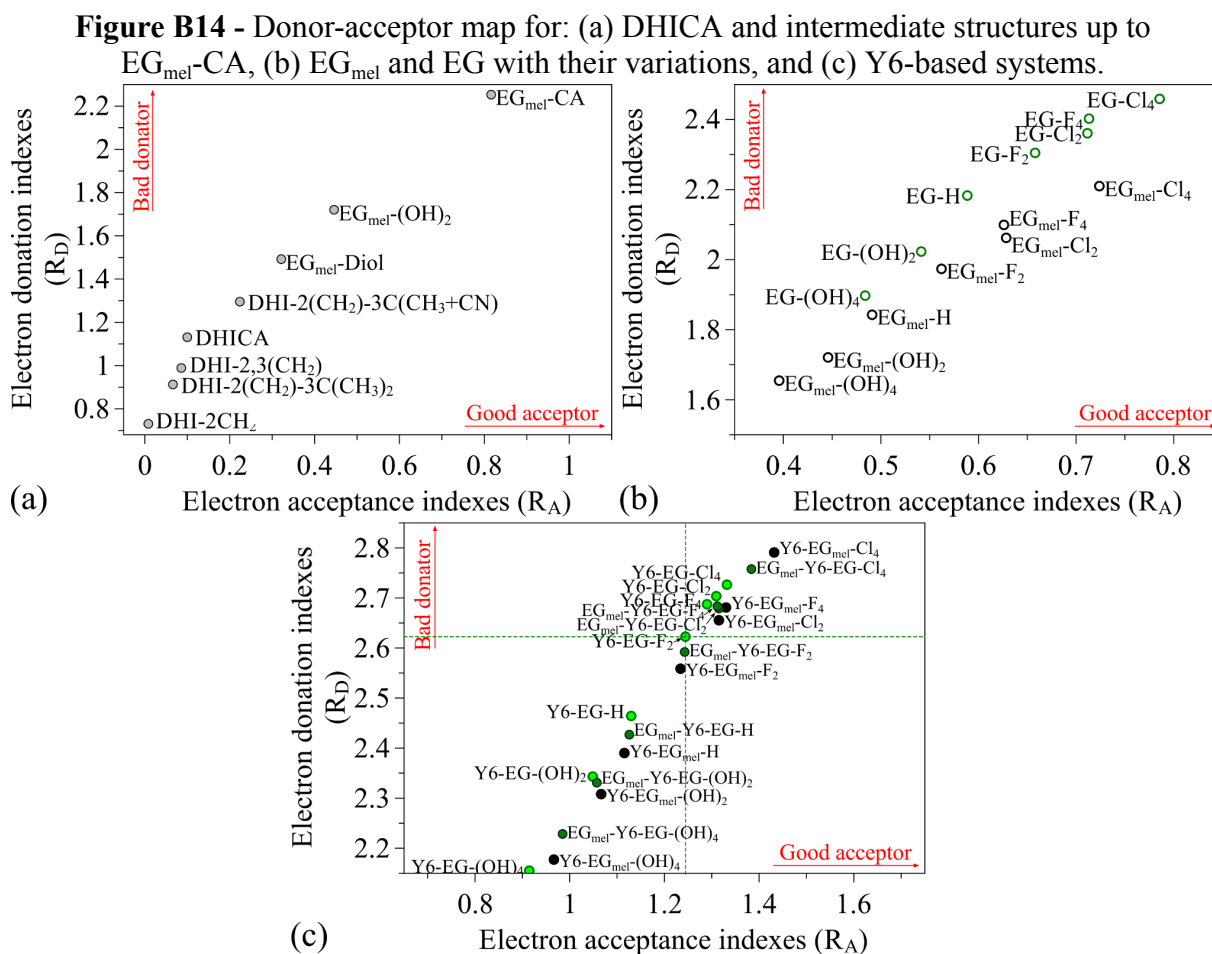
For all cases, high reactivity is noticed on the C≡C groups, these bonds facilitate conjugation and delocalization, while reinforcing molecular rigidity and planarity, that are essential for efficient charge transport in organic materials <sup>49</sup>. The molecular electrostatic potential exhibits high electronic density at the carbon-carbon triple bond and oxygen atoms. Similar trends are observed for larger oligomers, although the reactivity shifts towards the terminal units.

**Figure B13** - CAFIs estimated for extended structures of MIO<sub>9a</sub> and MIO<sub>9b</sub>.



## B6. Donation-acceptance indexes

Figures B14-B16 shows the donor-acceptor indexes for: (i) DHICA and variations up to EG<sub>mel</sub>-CA; (ii) isolated EG<sub>mel</sub> and EG with their variations; (iii) Y6-based systems with EG<sub>mel</sub>, EG and their variations; (iv) typical OSC acceptors and donors; and MIOs and (v) the angular coefficients associated with donors and acceptors.



Source: Author.

**Figure B15** - Donor-acceptor maps for MIOs and typical acceptors/donors employed in OSCs.

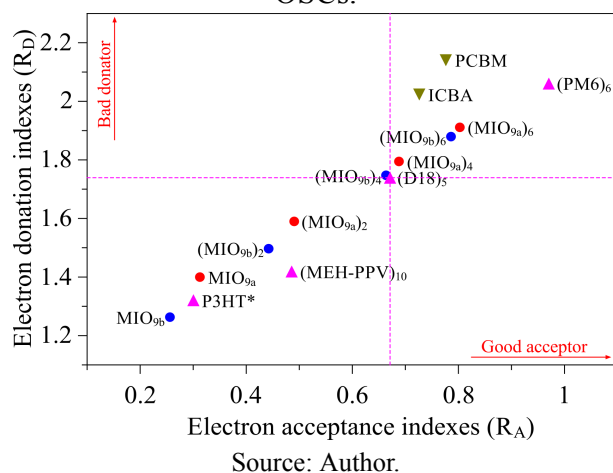
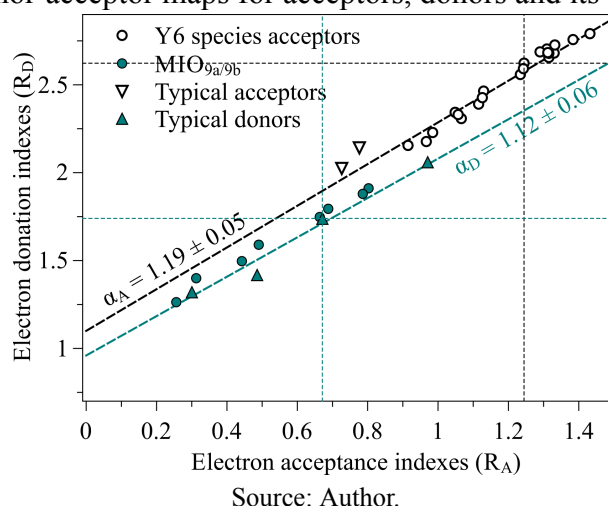


**Figure B16** - Donor-acceptor maps for acceptors, donors and its angular coefficient.



The evaluation of Figure B16 (and Figure 3.14 in the main text) reveals notable linear trends. Specifically, when analyzing only the Typical donor and MIO<sub>9a/9b</sub> materials as donors, alongside Typical fullerene-based and all Y6-based materials as acceptors, one can observe linear fits for both donor (D) and acceptor (A) sets. These fits exhibit similar slopes ( $\alpha$ ), indicating nearly parallel behavior, although they differ in their y-intercepts. This suggests that enhancements in the electron-accepting characteristics of these materials are accompanied by proportional reductions in their electron-donating ability, with the average slope  $\alpha^*$  defined as  $\frac{1}{2}(\alpha_A + \alpha_D) \approx \frac{1}{2}(1.19 + 1.12) \approx 1.155$ . The quasi-parallel nature of the  $R_D(R_A)$  curves for donors and acceptors establishes a meaningful criterion for identifying efficient donor-acceptor (D:A) combinations. In such cases, the line connecting the points  $P^A(R_A^A, R_D^A)$  and  $P^D(R_A^D, R_D^D)$  of a D:A material pair (DAM) should exhibit a slope ( $\Delta R_D/\Delta R_A$ ) greater than  $\alpha^*$ .

## B7. Organic solar cell's efficiency parameters

To evaluate the potential efficiency of the proposed donor–acceptor pairs in organic solar cells (OSCs), we calculated key parameters that influence device performance: the energy offsets for hole and electron transfer ( $\Delta E_{\text{HH}}$  and  $\Delta E_{\text{LL}}$ , respectively), and the open-circuit voltage ( $V_{\text{OC}}$ ). These values provide a theoretical basis for predicting charge separation efficiency and overall photovoltaic potential. The results, shown in Tables B4 and B5, include various combinations of MIO-based donors and functionalized Y6 acceptors, covering both symmetric and asymmetric systems with EG and EG<sub>mel</sub> terminal groups.

**Table B4** - Y6-EG<sub>mel</sub>-R<sub>n</sub> and Y6-EG-R<sub>n</sub> efficiency parameters.

Donor	Acceptor	$\Delta E_{\text{HH}}$ (eV)	$\Delta E_{\text{LL}}$ (eV)	$V_{\text{OC}}$ (eV)
(MIO <sub>9b</sub> ) <sub>6</sub>	Y6-EG-(OH) <sub>4</sub>	0.305	0.629	1.524
MIO <sub>9b</sub>	Y6-EG-(OH) <sub>4</sub>	0.307	1.345	1.521
D18	Y6-EG-H	0.330	1.088	1.431
MIO <sub>9a</sub>	Y6-EG-H	0.342	1.475	1.419
PM6	Y6-EG-(OH) <sub>2</sub>	0.401	0.535	1.372
(MIO <sub>9a</sub> ) <sub>6</sub>	Y6-EG-(OH) <sub>2</sub>	0.433	0.832	1.341
(MIO <sub>9b</sub> ) <sub>6</sub>	Y6-EG-(OH) <sub>2</sub>	0.475	0.855	1.298
MIO <sub>9b</sub>	Y6-EG-(OH) <sub>2</sub>	0.478	1.571	1.296
D18	Y6-EG-F <sub>2</sub>	0.474	1.260	1.258
MIO <sub>9a</sub>	Y6-EG-F <sub>2</sub>	0.486	1.648	1.246
(MIO <sub>9b</sub> ) <sub>6</sub>	Y6-EG <sub>mel</sub> -H	0.312	0.924	1.229
MIO <sub>9b</sub>	Y6-EG <sub>mel</sub> -H	0.315	1.640	1.226
PM6	Y6-EG-H	0.538	0.685	1.223
P3HT	Y6-EG-(OH) <sub>2</sub>	0.562	0.389	1.211
D18	Y6-EG-Cl <sub>2</sub>	0.523	1.325	1.193
(MIO <sub>9a</sub> ) <sub>6</sub>	Y6-EG-H	0.570	0.982	1.191
D18	Y6-EG-F <sub>4</sub>	0.539	1.334	1.185
D18	Y6-EG-Cl <sub>4</sub>	0.509	1.336	1.183

**Table B4 - Y6-EG<sub>mel</sub>-R<sub>n</sub> and Y6-EG-R<sub>n</sub> efficiency parameters (Continued).**

<b>Donor</b>	<b>Acceptor</b>	<b><math>\Delta E_{HH}</math> (eV)</b>	<b><math>\Delta E_{LL}</math> (eV)</b>	<b><math>V_{OC}</math> (eV)</b>
MIO <sub>9a</sub>	Y6-EG-Cl <sub>2</sub>	0.535	1.713	1.182
MIO <sub>9a</sub>	Y6-EG-F <sub>4</sub>	0.551	1.721	1.173
MIO <sub>9a</sub>	Y6-EG-Cl <sub>4</sub>	0.5216	1.723	1.171
(MIO <sub>9b</sub> ) <sub>6</sub>	Y6-EG-H	0.612	1.005	1.149
MIO <sub>9b</sub>	Y6-EG-H	0.615	1.721	1.146
P3HT	Y6-EG <sub>mel</sub> -H	0.399	0.458	1.142
PM6	Y6-EG <sub>mel</sub> -F <sub>2</sub>	0.413	0.789	1.119
(MIO <sub>9a</sub> ) <sub>6</sub>	Y6-EG <sub>mel</sub> -F <sub>2</sub>	0.445	1.086	1.087
P3HT	Y6-EG-H	0.699	0.538	1.062
PM6	Y6-EG-F <sub>2</sub>	0.682	0.858	1.050
(MIO <sub>9b</sub> ) <sub>6</sub>	Y6-EG <sub>mel</sub> -F <sub>2</sub>	0.487	1.108	1.045
PM6	Y6-EG <sub>mel</sub> -Cl <sub>2</sub>	0.453	0.864	1.043
MIO <sub>9b</sub>	Y6-EG <sub>mel</sub> -F <sub>2</sub>	0.490	1.824	1.042
(MIO <sub>9a</sub> ) <sub>6</sub>	Y6-EG-F <sub>2</sub>	0.714	1.155	1.019
(MIO <sub>9a</sub> ) <sub>6</sub>	Y6-EG <sub>mel</sub> -Cl <sub>2</sub>	0.484	1.162	1.012

Source: Author.

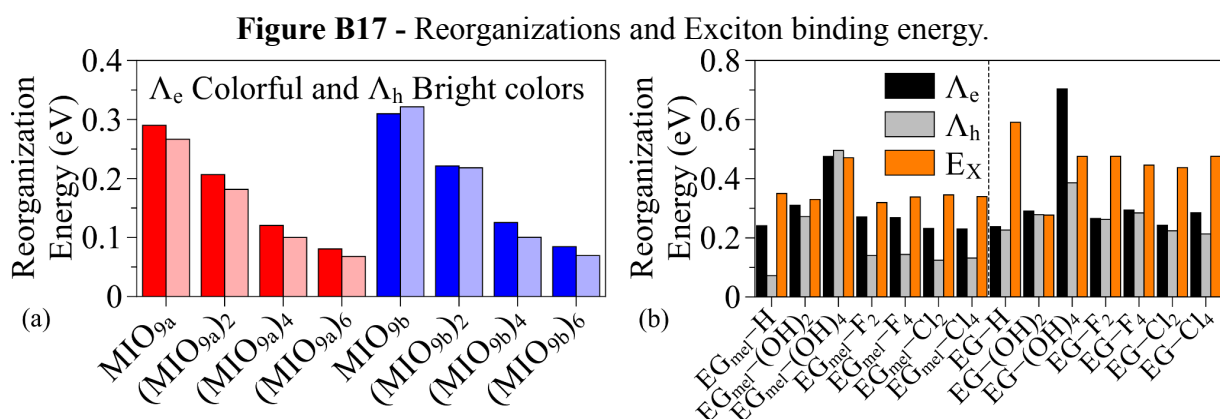
**Table B5** - EG<sub>mel</sub>-Y6-EG-R<sub>n</sub> and Y6-EG Y6-EG<sub>mel</sub>-R<sub>n</sub> efficiency parameters.

Donor	Acceptor	$\Delta E_{HH}$ (eV)	$\Delta E_{LL}$ (eV)	V <sub>OC</sub> (eV)
(MIO <sub>9b</sub> ) <sub>6</sub>	EG <sub>mel</sub> -Y6-EG-(OH) <sub>2</sub>	0.342	0.846	1.307
MIO <sub>9b</sub>	EG <sub>mel</sub> -Y6-EG-(OH) <sub>2</sub>	0.345	1.562	1.305
D18	EG <sub>mel</sub> -Y6-EG-F <sub>2</sub>	0.311	1.227	1.292
MIO <sub>9a</sub>	EG <sub>mel</sub> -Y6-EG-F <sub>2</sub>	0.323	1.614	1.280
PM6	EG <sub>mel</sub> -Y6-EG-H	0.347	0.643	1.264
(MIO <sub>9a</sub> ) <sub>6</sub>	EG <sub>mel</sub> -Y6-EG-H	0.378	0.940	1.233
D18	EG <sub>mel</sub> -Y6-EG-Cl <sub>2</sub>	0.351	1.294	1.224
P3HT	EG <sub>mel</sub> -Y6-EG-(OH) <sub>2</sub>	0.429	0.380	1.220
MIO <sub>9a</sub>	EG <sub>mel</sub> -Y6-EG-Cl <sub>2</sub>	0.363	1.681	1.213
D18	EG <sub>mel</sub> -Y6-EG-F <sub>4</sub>	0.378	1.325	1.193
(MIO <sub>9b</sub> ) <sub>6</sub>	EG <sub>mel</sub> -Y6-EG-H	0.421	0.963	1.190
MIO <sub>9b</sub>	EG <sub>mel</sub> -Y6-EG-H	0.423	1.679	1.188
MIO <sub>9a</sub>	EG <sub>mel</sub> -Y6-EG-F <sub>4</sub>	0.389	1.713	1.182
D18	EG <sub>mel</sub> -Y6-EG-Cl <sub>4</sub>	0.361	1.363	1.156
MIO <sub>9a</sub>	EG <sub>mel</sub> -Y6-EG-Cl <sub>4</sub>	0.373	1.751	1.144
P3HT	EG <sub>mel</sub> -Y6-EG-H	0.508	0.497	1.103
PM6	EG <sub>mel</sub> -Y6-EG-F <sub>2</sub>	0.519	0.824	1.083
(MIO <sub>9a</sub> ) <sub>6</sub>	EG <sub>mel</sub> -Y6-EG-F <sub>2</sub>	0.550	1.121	1.052
PM6	EG <sub>mel</sub> -Y6-EG-Cl <sub>2</sub>	0.559	0.891	1.016
(MIO <sub>9b</sub> ) <sub>6</sub>	EG <sub>mel</sub> -Y6-EG-F <sub>2</sub>	0.593	1.144	1.009
MIO <sub>9b</sub>	EG <sub>mel</sub> -Y6-EG-F <sub>2</sub>	0.596	1.860	1.007

Source: Author.

## B8. Reorganization energy

To understand the charge transport characteristics of the proposed materials, we evaluated the reorganization energies associated with hole ( $\Lambda_h$ ) and electron ( $\Lambda_e$ ) transfer processes. These parameters are crucial for estimating the mobility and stability of charge carriers in organic semiconductors. Figure B17a illustrates how increasing the chain length of oligomeric MIO structures reduces their reorganization energies, with  $\Lambda_h$  becoming smaller than  $\Lambda_e$  in some cases. Additionally, the impact of functional group substitutions on  $EG_{mel}$  and EG structures is analyzed (Figure B17b), revealing that hydroxylation tends to increase both  $\Lambda_h$  and  $\Lambda_e$ . Exciton binding energies were also calculated for these systems, offering further insight into their potential for efficient exciton dissociation in OSC applications.

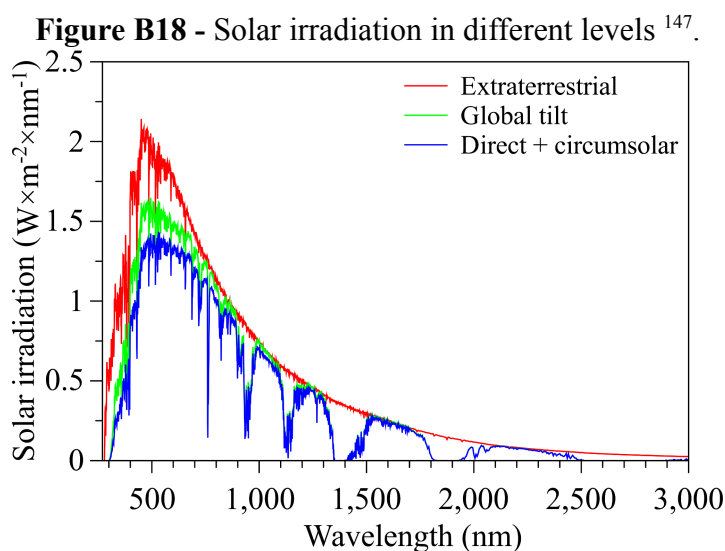


Source: Author.

Regarding the  $EG_{mel}$  and EG structures when hydrogen is replaced with hydroxyl and halogens on carbons 4, 5, 6, and 7 it is possible to see the  $\Lambda_h$  increasing, mainly for  $EG_{mel}-R_n$ . Replacing H with OH leads to a more significant increase in  $\Lambda_e$  and  $\Lambda_h$  compared to F or Cl, with a particularly notable rise when four hydroxyl groups are present.  $\Lambda_h$  remains smaller than  $\Lambda_e$  in most structures, except for  $EG_{mel}-(OH)_4$ , suggesting that these smaller structures act as better donors. The exciton binding energy does not follow a consistent trend; however, most structures exhibit values around 0.3 eV, typical of organic compounds. Notably, structures like  $EG_{mel}-(OH)_4$ , EG-H, EG-F<sub>2</sub>, EG-Cl<sub>2</sub>, EG-(OH)<sub>4</sub>, EG-F<sub>4</sub>, and EG-Cl<sub>4</sub> have exciton binding energies greater than 0.4 eV.

## B9. Sun absorption yield

Figure B18 shows the relationship between extraterrestrial radiation, direct radiation (that has reached the Earth's surface itself, at sea level) and global radiation (which includes both direct and diffuse radiation). This is due to the absorption that occurs when light passes through the atmosphere <sup>147</sup>. Direct radiation has been used to determine the sun absorption yield of all systems.

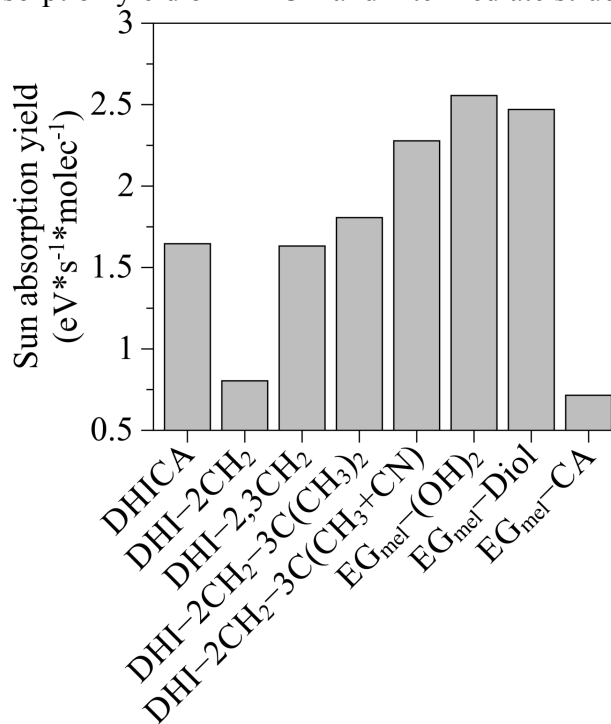


Source: Author.

Even though it is not possible to use the terminal group units or their variations with different functional groups directly as electron acceptors in OSCs, their solar absorption yields were calculated to understand the influence of the modifications and variations.

The results, summarized in Figures B19 and B20, highlight the effects of structural modifications on light absorption. Although the terminal units and their functionalized variants are not suitable as standalone acceptors, their absorption profiles provide valuable insights into how chemical substitutions influence optical performance.

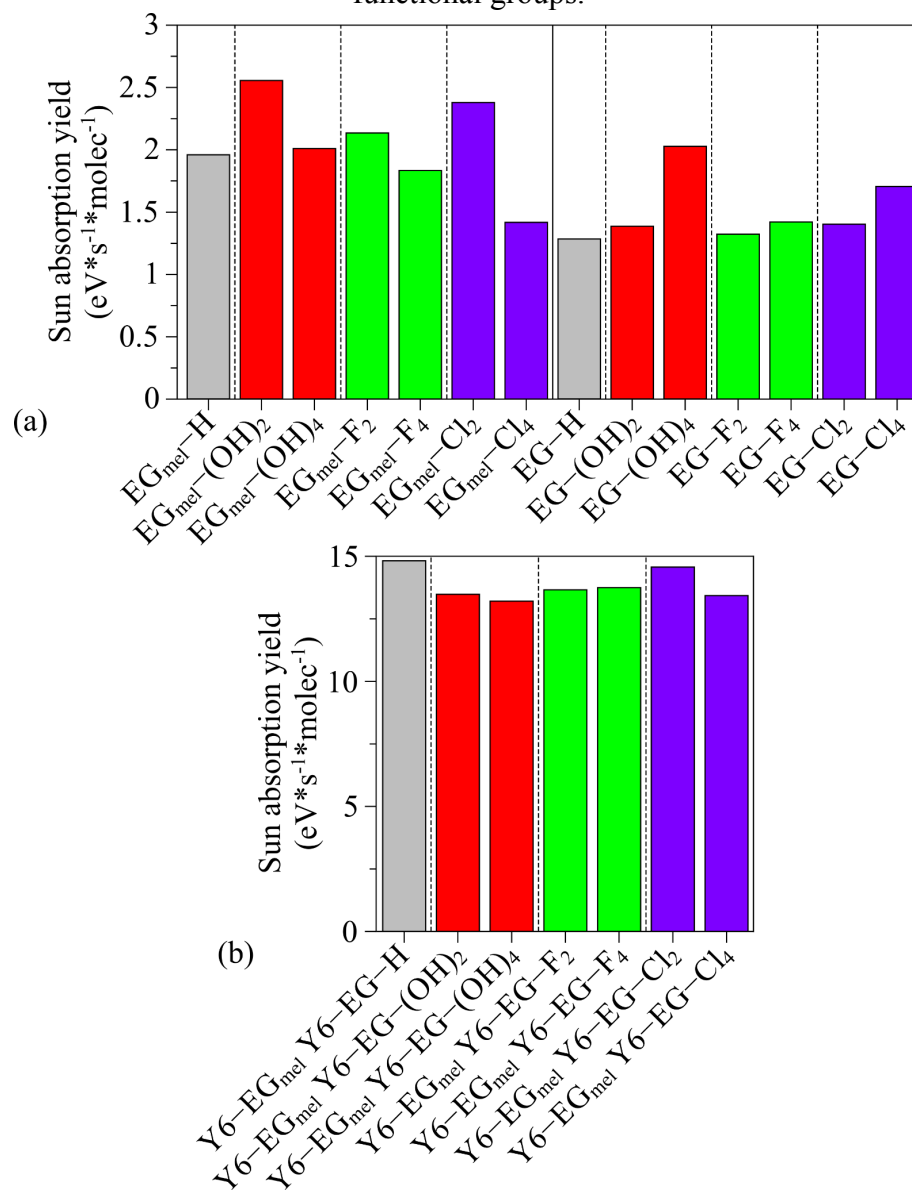
**Figure B19** - Sun absorption yield of DHICA and intermediate structures up to EG<sub>mel</sub>-CA.



Source: Author.

Figure B19 shows a decrease in DHICA absorption when CA is replaced with 2-methylene. However, absorption increases with the other additions. A comparison of DHICA and EG<sub>mel</sub>-CA absorption, where the only difference is the nitrile group, reveals a big decrease.

**Figure B20** - Sun absorption yields for  $EG_{mel}-R_n$ ,  $EG-R_n$  and Y6 clusters with different functional groups.



Source: Author.

Figure B20 displays the absorption yield of  $EG_{mel}$  and EG. It is evident that  $EG_{mel}$  has a higher absorption rate than EG due to the presence of smaller peaks in the visible light spectrum between 490 and 528 nm, where sun irradiation is stronger.

## CHAPTER IV – General Conclusions

This study confirms the potential of melanin-inspired compounds as sustainable and versatile materials for organic electronics, with a focus on two critical application areas: environmental monitoring and renewable energy. Computational analyses demonstrated that these compounds are highly effective in detecting hazardous nitroaromatic compounds (NACs), such as trinitrotoluene (TNT) and trinitrophenol (TNP). The adsorption of NACs significantly modulates the electronic, optical, and vibrational properties of the melanin-based materials. These interactions remain stable even under thermal stress, as supported by Born–Oppenheimer molecular dynamics simulations, reinforcing their suitability for chemiresistive and reversible electrochemical sensor platforms. The findings offer a cost-effective and environmentally responsible alternative to conventional detection systems.

In the field of organic solar cells (OSCs), melanin building units emerge as promising functional groups to be employed in non-fullerene acceptors. The simulations demonstrate that, when integrated into Y6 core, these materials can enhance light absorption, facilitate exciton dissociation, and improve charge transport. The functionalization of melanin derivatives with electron-donating or electron-withdrawing groups, such as hydroxyl or halogen substituents, enables fine-tuning of their electronic properties, leading to improvements in both efficiency and operational stability of photovoltaic devices.

Taken together, this work offers a theoretical framework for understanding and optimizing melanin-inspired compounds in two complementary sectors of organic electronics. Their demonstrated dual functionality, as selective chemical sensors and as efficient photovoltaic materials, highlights their versatility and underscores their relevance to sustainable technological development. The results support the advancement of bio-inspired approaches and encourage experimental validation toward the implementation of practical, low-impact devices for environmental safety and renewable energy harvesting.

## REFERENCES

1. Lim JW. Polymer Materials for Optoelectronics and Energy Applications. *Materials*. 2024;17(15):3698. doi:10.3390/ma17153698
2. Kumar A, Gupta RK, eds. *Bioelectronics: Materials, Technologies, and Emerging Applications*. First edition. CRC Press; 2023.
3. Brizuela Guerra N, Morais Lima JV, Nozella NL, Boratto MH, Paulin JV, Graeff CFDO. Electrochemical Doping Effect on the Conductivity of Melanin-Inspired Materials. *ACS Appl Bio Mater*. 2024;7(4):2186-2196. doi:10.1021/acsabm.3c01166
4. Ozlu B, Ahmed MB, Muthoka RM, et al. Naturally derived electrically active materials for eco-friendly electronics. *Mater Today Adv*. 2024;21:100470. doi:10.1016/j.mtadv.2024.100470
5. Piacenti Da Silva M, Fernandes JC, De Figueiredo NB, Congiu M, Mulato M, De Oliveira Graeff CF. Melanin as an active layer in biosensors. *AIP Adv*. 2014;4(3):037120. doi:10.1063/1.4869638
6. Wu TF, Hong JD. Synthesis of water-soluble dopamine–melanin for ultrasensitive and ultrafast humidity sensor. *Sens Actuators B Chem*. 2016;224:178-184. doi:10.1016/j.snb.2015.10.015
7. Selvaraju S, Niradha Sachinthan KA, Hopson RA, et al. Eumelanin-inspired core derived from vanillin: a new building block for organic semiconductors. *Chem Commun*. 2015;51(14):2957-2959. doi:10.1039/C4CC09011J
8. Tiwari J, Tarale P, Sivanesan S, Bafana A. Environmental persistence, hazard, and mitigation challenges of nitroaromatic compounds. *Environ Sci Pollut Res*. 2019;26(28):28650-28667. doi:10.1007/s11356-019-06043-8
9. Huang T, Sun G, Zhao L, Zhang N, Zhong R, Peng Y. Quantitative Structure-Activity Relationship (QSAR) Studies on the Toxic Effects of Nitroaromatic Compounds (NACs): A Systematic Review. *Int J Mol Sci*. 2021;22(16):8557. doi:10.3390/ijms22168557
10. Liu J, Li J, Jian P, Jian R. Intriguing hierarchical Co@NC microflowers in situ assembled by nanoneedles: Towards enhanced reduction of nitroaromatic compounds via interfacial synergistic catalysis. *J Hazard Mater*. 2021;403:123987. doi:10.1016/j.jhazmat.2020.123987
11. Liu Q, Jiang Y, Jin K, et al. 18% Efficiency organic solar cells. *Sci Bull*. 2020;65(4):272-275. doi:10.1016/j.scib.2020.01.001
12. Sun C, Lee J, Tan Z, et al. Regiospecific Incorporation of Acetylene Linker in High-Electron Mobility Dimerized Acceptors for Organic Solar Cells with High Efficiency (18.8%) and Long 1-Sun Lifetime (> 5000 h). *Adv Energy Mater*. 2023;13(34):2301283. doi:10.1002/aenm.202301283
13. Freitas AV, Alves GGB, Paschoal GMA, et al. A DFT bottom-up approach on

- non-fullerene acceptors: what makes highly efficient acceptors. *J Mater Sci.* 2024;59(24):10888-10903. doi:10.1007/s10853-024-09811-1
14. Xiao X, Chalh M, Loh ZR, et al. Strategies to achieve efficiencies of over 19% for organic solar cells. *Cell Rep Phys Sci.* 2025;6(1):102390. doi:10.1016/j.xcrp.2024.102390
  15. Chen H, Lai H, Chen Z, et al. 17.1 %-Efficient Eco-Compatible Organic Solar Cells from a Dissymmetric 3D Network Acceptor. *Angew Chem.* 2021;133(6):3275-3283. doi:10.1002/ange.202013053
  16. Hong L, Yao H, Cui Y, Ge Z, Hou J. Recent advances in high-efficiency organic solar cells fabricated by eco-compatible solvents at relatively large-area scale. *APL Mater.* 2020;8(12):120901. doi:10.1063/5.0027948
  17. Pradhan S, Brooks AK, Yadavalli VK. Nature-derived materials for the fabrication of functional biodevices. *Mater Today Bio.* 2020;7:100065. doi:10.1016/j.mtbio.2020.100065
  18. Tiwari J, Naoghare P, Sivanesan S, Bafana A. Biodegradation and detoxification of chloronitroaromatic pollutant by *Cupriavidus*. *Bioresour Technol.* 2017;223:184-191. doi:10.1016/j.biortech.2016.10.043
  19. Li X, Zhang X, Xu Y, Yu P. Removal of nitrobenzene from aqueous solution by using modified magnetic diatomite. *Sep Purif Technol.* 2020;242:116792. doi:10.1016/j.seppur.2020.116792
  20. Mansour C, Guibbolini M, Rouane Hacene O, Saidane Mosbahi D, Risso-de Faverney C. Oxidative Stress and Damage Biomarkers in Clam *Ruditapes decussatus* Exposed to a Polluted Site: The Reliable Biomonitoring Tools in Hot and Cold Seasons. *Arch Environ Contam Toxicol.* 2020;78(3):478-494. doi:10.1007/s00244-020-00713-2
  21. . MP, . AJS, . PKS. NITROBENZENE POISONING WITH METHEMOGLOBINEMIA. *Indian J Case Rep.* 2019;5(1):59-60. doi:10.32677/IJCR.2019.v05.i01.020
  22. Shrestha N, Karki B, Shrestha PS, Gami R, Acharya SP, Acharya S. Management of nitrobenzene poisoning with oral methylene blue and vitamin C in a resource limited setting: A case report. *Toxicol Rep.* 2020;7:1008-1009. doi:10.1016/j.toxrep.2020.08.012
  23. Bombuwala Dewage N, Liyanage AS, Smith Q, et al. Fast aniline and nitrobenzene remediation from water on magnetized and nonmagnetized Douglas fir biochar. *Chemosphere.* 2019;225:943-953. doi:10.1016/j.chemosphere.2019.03.050
  24. Toal SJ, Trogler WC. Polymer sensors for nitroaromatic explosives detection. *J Mater Chem.* 2006;16(28):2871. doi:10.1039/b517953j
  25. Wang J. Electrochemical Sensing of Explosives. *Electroanalysis.* 2007;19(4):415-423. doi:10.1002/elan.200603748
  26. Germain ME, Knapp MJ. Optical explosives detection: from color changes to

- fluorescence turn-on. *Chem Soc Rev.* 2009;38(9):2543. doi:10.1039/b809631g
27. Bai H, Li C, Shi G. Rapid nitroaromatic compounds sensing based on oligopyrene. *Sens Actuators B Chem.* 2008;130(2):777-782. doi:10.1016/j.snb.2007.10.045
  28. Stringer RC, Gangopadhyay S, Grant SA. Detection of Nitroaromatic Explosives Using a Fluorescent-Labeled Imprinted Polymer. *Anal Chem.* 2010;82(10):4015-4019. doi:10.1021/ac902838c
  29. Liu JQ, Luo ZD, Pan Y, Kumar Singh A, Trivedi M, Kumar A. Recent developments in luminescent coordination polymers: Designing strategies, sensing application and theoretical evidences. *Coord Chem Rev.* 2020;406:213145. doi:10.1016/j.ccr.2019.213145
  30. Verbitskiy EV, Rusinov GL, Chupakhin ON, Charushin VN. Design of fluorescent sensors based on azaheterocyclic push-pull systems towards nitroaromatic explosives and related compounds: A review. *Dyes Pigments.* 2020;180:108414. doi:10.1016/j.dyepig.2020.108414
  31. Kumar V, Saini SK, Choudhury N, et al. Highly Sensitive Detection of Nitro Compounds Using a Fluorescent Copolymer-Based FRET System. *ACS Appl Polym Mater.* 2021;3(8):4017-4026. doi:10.1021/acsapm.1c00540
  32. Mitri F, De Iacovo A, De Santis S, et al. A compact optical sensor for explosive detection based on NIR luminescent quantum dots. *Appl Phys Lett.* 2021;119(4):041106. doi:10.1063/5.0060400
  33. Mitri F, Iacovo AD, Santis SD, Sotgiu G, Colace L. Quantum Dots for Explosive Detection in Air - Two Complimentary Approaches. In: *2022 17th Conference on Ph.D Research in Microelectronics and Electronics (PRIME)*. IEEE; 2022:53-56. doi:10.1109/PRIME55000.2022.9816790
  34. Mitri F, De Iacovo A, De Santis S, et al. Optical gas sensor based on the combination of a QD photoluminescent probe and a QD photodetector. *Nanotechnology.* 2022;33(47):475501. doi:10.1088/1361-6528/ac8814
  35. Sikka R, Kumar P. Optical detection of nitroaromatic compounds using MAPbBr<sub>3</sub> at room temperature. *J Chem Sci.* 2023;135(3):85. doi:10.1007/s12039-023-02191-0
  36. Chakraborty D, Bej S, Sahoo S, et al. Novel Nanoporous Ti-Phosphonate Metal–Organic Framework for Selective Sensing of 2,4,6-Trinitrophenol and a Promising Electrode in an Energy Storage Device. *ACS Sustain Chem Eng.* 2021;9(42):14224-14237. doi:10.1021/acssuschemeng.1c04877
  37. Kumar P, Kim KH, Lee J, et al. Metal-organic framework for sorptive/catalytic removal and sensing applications against nitroaromatic compounds. *J Ind Eng Chem.* 2020;84:87-95. doi:10.1016/j.jiec.2019.12.024
  38. Sharma A, Kim D, Park JH, et al. Mechanistic insight into the sensing of nitroaromatic compounds by metal-organic frameworks. *Commun Chem.* 2019;2(1):39. doi:10.1038/s42004-019-0135-2

39. Dutta B, Hazra A, Datta S, Sinha C, Banerjee P, Mir MH. *In Situ Trans–Cis* Isomerization of Naphthylvinylpyridine Ligand in a Zinc(II) Coordination Polymer: Liquid and Vapor Phase Sensing of Mutagenic Pollutants and Nitroexplosives. *ACS Appl Polym Mater.* 2022;4(4):2841-2850. doi:10.1021/acsapm.2c00099
40. Samanta P, Dutta S, Ghosh SK. Metal-organic frameworks for detection and desensitization of environmentally hazardous nitro-explosives and related high energy materials. In: *Metal-Organic Frameworks (MOFs) for Environmental Applications.* Elsevier; 2019:231-283. doi:10.1016/B978-0-12-814633-0.00002-8
41. Kumar P, Bansal V, Kim KH, Kwon EE. Metal-organic frameworks (MOFs) as futuristic options for wastewater treatment. *J Ind Eng Chem.* 2018;62:130-145. doi:10.1016/j.jiec.2017.12.051
42. Tehrani Z, Whelan SP, Mostert AB, et al. Printable and flexible graphene pH sensors utilising thin film melanin for physiological applications. *2D Mater.* 2020;7(2):024008. doi:10.1088/2053-1583/ab72d5
43. Antidormi A, Melis C, Canadell E, Colombo L. Assessing the Performance of Eumelanin/Si Interface for Photovoltaic Applications. *J Phys Chem C.* 2017;121(21):11576-11584. doi:10.1021/acs.jpcc.7b02970
44. Vahidzadeh E, Kalra AP, Shankar K. Melanin-based electronics: From proton conductors to photovoltaics and beyond. *Biosens Bioelectron.* 2018;122:127-139. doi:10.1016/j.bios.2018.09.026
45. Migliaccio L, Aprano S, Iannuzzi L, et al. Eumelanin–PEDOT:PSS Complementing En Route to Mammalian-Pigment-Based Electrodes: Design and Fabrication of an ITO-Free Organic Light-Emitting Device. *Adv Electron Mater.* 2017;3(5):1600342. doi:10.1002/aelm.201600342
46. d’Ischia M, Napolitano A, Pezzella A, Meredith P, Buehler M. Melanin Biopolymers: Tailoring Chemical Complexity for Materials Design. *Angew Chem Int Ed.* 2020;59(28):11196-11205. doi:10.1002/anie.201914276
47. D’Ischia M. Melanin-Based Functional Materials. *Int J Mol Sci.* 2018;19(1):228. doi:10.3390/ijms19010228
48. Selvaraju S, Adhikari S, Hopson RA, et al. Effects of structural variations on the optical and electronic properties of eumelanin-inspired small molecules. *J Mater Chem C.* 2016;4(18):3995-3999. doi:10.1039/C5TC03982G
49. Zhou L, Feng R ran, Zhang W, Gai F. Triple-Bond Vibrations: Emerging Applications in Energy and Biological Sciences. *J Phys Chem Lett.* 2024;15(1):187-200. doi:10.1021/acs.jpcllett.3c02619
50. Batagin-Neto A, Bronze-Uhle ES, Fernandes DM, et al. Optical Behavior of Conjugated Pt-Containing Polymetallaynes Exposed to Gamma-Ray Radiation Doses. *J Phys Chem B.* 2011;115(25):8047-8053. doi:10.1021/jp200831z
51. Bronze-Uhle ES, Batagin-Neto A, Fernandes DM, Fratoddi I, Russo MV, Graeff CFO. Poly [1,1’-bis(ethynyl)-4,4’-biphenyl(bis-tributylphosphine)Pt(II)] solutions used as low

- dose ionizing radiation dosimeter. *Appl Phys Lett*. 2013;102(24):241917. doi:10.1063/1.4812186
52. Chiodi D, Ishihara Y. The role of the methoxy group in approved drugs. *Eur J Med Chem*. 2024;273:116364. doi:10.1016/j.ejmech.2024.116364
  53. Wazzan N, Safi Z. Effect of number and position of methoxy substituents on fine-tuning the electronic structures and photophysical properties of designed carbazole-based hole-transporting materials for perovskite solar cells: DFT calculations. *Arab J Chem*. 2019;12(1):1-20. doi:10.1016/j.arabjc.2018.06.014
  54. Han Y, Li W, Song C, Wu Y, Peyghan FA. A density functional theory investigation on the Ag-decorated boron nitride nanosheet as an isoniazid drug sensor. *Monatshefte Für Chem - Chem Mon*. 2022;153(2):153-160. doi:10.1007/s00706-021-02882-9
  55. G. B. Alves G, Batagin-Neto A. Local Reactivity on Carbon Quantum Dots: The Influence of the Geometries and Chemical Doping for Chemical Sensor Applications. *J Phys Chem C*. 2023;127(7):3819-3829. doi:10.1021/acs.jpcc.2c08612
  56. Roy Dennington, Todd A. Keith, John M. Millam. GaussView 6. Published online 20116. <https://gaussian.com/citation/>
  57. Allouche A. Gabedit—A graphical user interface for computational chemistry softwares. *J Comput Chem*. 2011;32(1):174-182. doi:10.1002/jcc.21600
  58. Becke AD. Density-functional thermochemistry. III. The role of exact exchange. *J Chem Phys*. 1993;98(7):5648-5652. doi:10.1063/1.464913
  59. Lee C, Yang W, Parr RG. Development of the Colle-Salvetti correlation-energy formula into a functional of the electron density. *Phys Rev B*. 1988;37(2):785-789. doi:10.1103/PhysRevB.37.785
  60. Yang W, Mortier WJ. The use of global and local molecular parameters for the analysis of the gas-phase basicity of amines. *J Am Chem Soc*. 1986;108(19):5708-5711.
  61. Geerlings P, De Proft F, Langenaeker W. Conceptual Density Functional Theory. *Chem Rev*. 2003;103(5):1793-1874. doi:10.1021/cr990029p
  62. Chirlian LE, Francl MM. Atomic charges derived from electrostatic potentials: A detailed study. *J Comput Chem*. 1987;8(6):894-905. doi:10.1002/jcc.540080616
  63. Hoffmann MWG, Prades JD, Mayrhofer L, et al. Highly Selective SAM–Nanowire Hybrid NO<sub>2</sub> Sensor: Insight into Charge Transfer Dynamics and Alignment of Frontier Molecular Orbitals. *Adv Funct Mater*. 2014;24(5):595-602. doi:10.1002/adfm.201301478
  64. EL Ouafy H, EL OUAIFY T, Oubenali M, Mbarki M, Echajia M. Analysis of the molecular electrostatic potential of the chemical reactivity of p-nitrophenol, p-aminophenol and p-methylphenol by the quantum method. *Appl J Environ Eng Sci*. 2020;Vol. 6:El Ouafy& al./ Appl. J. Envir. Eng. Sci. 6 N°4(2020) 363-373 Pages. doi:10.48422/IMIST.PRSM/AJEES-V6I4.23471

65. Jiang N, Li G, Che W, Zhu D, Su Z, Bryce MR. Polyurethane derivatives for highly sensitive and selective fluorescence detection of 2,4,6-trinitrophenol (TNP). *J Mater Chem C*. 2018;6(42):11287-11291. doi:10.1039/C8TC04250K
66. Drissi M, Benhalima N, Megrouss Y, Rachida R, Chouaih A, Hamzaoui F. Theoretical and Experimental Electrostatic Potential around the m-Nitrophenol Molecule. *Molecules*. 2015;20(3):4042-4054. doi:10.3390/molecules20034042
67. Martínez A, Rodríguez-Gironés MA, Barbosa A, Costas M. Donator Acceptor Map for Carotenoids, Melatonin and Vitamins. *J Phys Chem A*. 2008;112(38):9037-9042. doi:10.1021/jp803218e
68. Gázquez JL, Cedillo A, Vela A. Electrodonating and Electroaccepting Powers. *J Phys Chem A*. 2007;111(10):1966-1970. doi:10.1021/jp065459f
69. M. J. Frisch, G. W. Trucks, H. B. Schlegel, et al. Gaussian 16. Published online 2016. <https://gaussian.com/citation/>
70. Plett C, Grimme S. Automated and Efficient Generation of General Molecular Aggregate Structures. *Angew Chem Int Ed*. 2023;62(4):e202214477. doi:10.1002/anie.202214477
71. Grimme S, Antony J, Ehrlich S, Krieg H. A consistent and accurate *ab initio* parametrization of density functional dispersion correction (DFT-D) for the 94 elements H-Pu. *J Chem Phys*. 2010;132(15):154104. doi:10.1063/1.3382344
72. Boys SF, Bernardi F. The calculation of small molecular interactions by the differences of separate total energies. Some procedures with reduced errors. *Mol Phys*. 1970;19(4):553-566. doi:10.1080/00268977000101561
73. Simon S, Duran M, Dannenberg JJ. How does basis set superposition error change the potential surfaces for hydrogen-bonded dimers? *J Chem Phys*. 1996;105(24):11024-11031. doi:10.1063/1.472902
74. Johnson ER, Keinan S, Mori-Sánchez P, Contreras-García J, Cohen AJ, Yang W. Revealing Noncovalent Interactions. *J Am Chem Soc*. 2010;132(18):6498-6506. doi:10.1021/ja100936w
75. Lu T, Chen Q. Visualization analysis of weak interactions in chemical systems. Published online 2024.
76. Lu T, Chen F. Multiwfn: A multifunctional wavefunction analyzer. *J Comput Chem*. 2012;33(5):580-592. doi:10.1002/jcc.22885
77. Pecchia A, Penazzi G, Salvucci L, Di Carlo A. Non-equilibrium Green's functions in density functional tight binding: method and applications. *New J Phys*. 2008;10(6):065022. doi:10.1088/1367-2630/10/6/065022
78. Spiegelman F, Tarrat N, Cuny J, et al. Density-functional tight-binding: basic concepts and applications to molecules and clusters. *Adv Phys X*. 2020;5(1):1710252. doi:10.1080/23746149.2019.1710252

79. Gaus M, Goez A, Elstner M. Parametrization and Benchmark of DFTB3 for Organic Molecules. *J Chem Theory Comput.* 2013;9(1):338-354. doi:10.1021/ct300849w
80. Ehlert S. Simple DFT-D3: Library first implementation of the D3dispersion correction. *J Open Source Softw.* 2024;9(103):7169. doi:10.21105/joss.07169
81. Dickey JM, Paskin A. Computer Simulation of the Lattice Dynamics of Solids. *Phys Rev.* 1969;188(3):1407-1418. doi:10.1103/PhysRev.188.1407
82. Futera Z, Tse JS, English NJ. Possibility of realizing superionic ice VII in external electric fields of planetary bodies. *Sci Adv.* 2020;6(21):eaaz2915. doi:10.1126/sciadv.aaz2915
83. Bosse J, Götze W, Zippelius A. Velocity-autocorrelation spectrum of simple classical liquids. *Phys Rev A.* 1978;18(3):1214-1221. doi:10.1103/PhysRevA.18.1214
84. Buimaga-Iarinca L, Morari C. Calculation of infrared spectra for adsorbed molecules from the dipole autocorrelation function. *Theor Chem Acc.* 2022;141(11):69. doi:10.1007/s00214-022-02932-3
85. Martinez-Gonzalez JA, English NJ, Gowen AA. Understanding the interface between silicon-based materials and water: Molecular-dynamics exploration of infrared spectra. *AIP Adv.* 2017;7(11):115105. doi:10.1063/1.4999086
86. Lascane LG, Oliveira EF, Galvão DS, Batagin-Neto A. Polyfuran-based chemical sensors: Identification of promising derivatives via DFT calculations and fully atomistic reactive molecular dynamics. *Eur Polym J.* 2020;141:110085. doi:10.1016/j.eurpolymj.2020.110085
87. Coleone AP, Barboza BH, Batagin-Neto A. Polypyrrole derivatives for detection of toxic gases: A theoretical study. *Polym Adv Technol.* 2021;32(11):4464-4478. doi:10.1002/pat.5449
88. Sawant R, Chakraborty S, Papalkar A, Awale A, Chaskar A. Low-dimensional fluorescent sensors for nitro explosive detection: A review. *Mater Today Chem.* 2024;37:101983. doi:10.1016/j.mtchem.2024.101983
89. Voznyy O, Dubowski JJ. Adsorption Kinetics of Hydrogen Sulfide and Thiols on GaAs (001) Surfaces in a Vacuum. *J Phys Chem C.* 2008;112(10):3726-3733. doi:10.1021/jp075968x
90. Alghamdi NM, Al-qahtani HM, Alkhalidi A, Fadlallah MM, Maarouf AA. Investigating the Electronic and Molecular Adsorption Properties of Ti/Co-Doped Boron Carbon Nitride. *Molecules.* 2025;30(9):1873. doi:10.3390/molecules30091873
91. Morais WO, Felix JPC, Silva GRD, et al. Understanding stability and reactivity of transition metal single-atoms on graphene. *Sci Rep.* 2025;15(1). doi:10.1038/s41598-025-00126-y
92. Kazemi A, Manteghi F, Tehrani Z. Metal Electrocatalysts for Hydrogen Production in Water Splitting. *ACS Omega.* Published online January 29, 2024. doi:10.1021/acsomega.3c07911

93. Role of zeolite adsorbent in water treatment. In: *Handbook of Nanomaterials for Wastewater Treatment*. Elsevier; 2021:417-481. doi:10.1016/b978-0-12-821496-1.00024-6
94. Nabeela, Hashmi MA, Saqib ANS, Kamran A, Lakhani A. Detection of nitro-aromatics using  $C_5N_2$  as an electrochemical sensor: a DFT approach. *RSC Adv*. 2024;14(41):30116-30126. doi:10.1039/d4ra05600k
95. Sathya AT, Jethawa U, Sarkar SG, Chakraborty B. Pd-decorated MoSi<sub>2</sub>N<sub>4</sub> monolayer: Enhanced nitrobenzene sensing through DFT perspective. *J Mol Liq*. 2025;427:127310. doi:10.1016/j.molliq.2025.127310
96. Hibben JH. Raman Spectra in Organic Chemistry. *Chem Rev*. 1936;18(1):1-232. doi:10.1021/cr60059a001
97. Peach MJG, Benfield P, Helgaker T, Tozer DJ. Excitation energies in density functional theory: An evaluation and a diagnostic test. *J Chem Phys*. 2008;128(4). doi:10.1063/1.2831900
98. Zheng Z, Wang J, Bi P, et al. Tandem Organic Solar Cell with 20.2% Efficiency. *Joule*. 2022;6(1):171-184. doi:10.1016/j.joule.2021.12.017
99. Liu Y, Liu B, Ma CQ, et al. Recent progress in organic solar cells (Part I material science). *Sci China Chem*. 2022;65(2):224-268. doi:10.1007/s11426-021-1180-6
100. Wöhrle D, Meissner D. Organic Solar Cells. *Adv Mater*. 1991;3(3):129-138. doi:10.1002/adma.19910030303
101. Chamberlain GA. Organic solar cells: A review. *Sol Cells*. 1983;8(1):47-83. doi:10.1016/0379-6787(83)90039-X
102. Morel DL, Ghosh AK, Feng T, et al. High-efficiency organic solar cells. *Appl Phys Lett*. 1978;32(8):495-497. doi:10.1063/1.90099
103. Ghosh AK, Feng T. Merocyanine organic solar cells. *J Appl Phys*. 1978;49(12):5982-5989. doi:10.1063/1.324566
104. Yu G, Gao J, Hummelen JC, Wudl F, Heeger AJ. Polymer Photovoltaic Cells: Enhanced Efficiencies via a Network of Internal Donor-Acceptor Heterojunctions. *Science*. 1995;270(5243):1789-1791. doi:10.1126/science.270.5243.1789
105. Xiao Z, Geng X, He D, Jia X, Ding L. Development of isomer-free fullerene bisadducts for efficient polymer solar cells. *Energy Environ Sci*. 2016;9(6):2114-2121. doi:10.1039/C6EE01026A
106. Shoaee S, Luong HM, Song J, Zou Y, Nguyen T, Neher D. What We have Learnt from PM6:Y6. *Adv Mater*. 2024;36(20):2302005. doi:10.1002/adma.202302005
107. Wei Q, Liu W, Leclerc M, Yuan J, Chen H, Zou Y. A-DA'D-A non-fullerene acceptors for high-performance organic solar cells. *Sci China Chem*. 2020;63(10):1352-1366. doi:10.1007/s11426-020-9799-4

108. Yuan J, Zou Y. The history and development of Y6. *Org Electron*. 2022;102:106436. doi:10.1016/j.orgel.2022.106436
109. Lu B, Wang J, Zhang Z, et al. Recent progress of Y-series electron acceptors for organic solar cells. *Nano Sel*. 2021;2(11):2029-2039. doi:10.1002/nano.202100036
110. Xiang Y, Xu C, Zheng S. Increasing Charge Carrier Mobility through Modifications of Terminal Groups of Y6: A Theoretical Study. *Int J Mol Sci*. 2023;24(10):8610. doi:10.3390/ijms24108610
111. Saeed MA, Xuyao S, Kim HS, et al. Side-Chain Engineering of Y-Series Acceptors with Halogenated End-Group for Efficient Indoor Organic Photovoltaics. *Adv Opt Mater*. 2024;12(9):2302145. doi:10.1002/adom.202302145
112. Alves GGB, Bégué D, Batagin-Neto A. Reactivity-based descriptors for donor-acceptor efficiency in organic solar cells. *Comput Theor Chem*. 2025;1251:115316. doi:10.1016/j.comptc.2025.115316
113. Luo Z, Liu T, Ma R, et al. Precisely Controlling the Position of Bromine on the End Group Enables Well-Regular Polymer Acceptors for All-Polymer Solar Cells with Efficiencies over 15%. *Adv Mater*. 2020;32(48):2005942. doi:10.1002/adma.202005942
114. Xiang Y, Cao Z, Zhang X, Zou Z, Zheng S. Enhanced Photovoltaic Properties of Y6 Derivatives with Asymmetric Terminal Groups: A Theoretical Insight. *Int J Mol Sci*. 2023;24(19):14753. doi:10.3390/ijms241914753
115. Qiu W, Zheng S. Effects of functionalization of Y6 end-groups with electron-withdrawing groups on the photovoltaic properties at the donor-acceptor interfaces of PM6/Y6 OSCs: A theoretical insight. *Org Electron*. 2021;96:106235. doi:10.1016/j.orgel.2021.106235
116. Xiao M, Chen W, Li W, et al. Elucidation of the hierarchical structure of natural eumelanins. *J R Soc Interface*. 2018;15(140):20180045. doi:10.1098/rsif.2018.0045
117. Guo L, Li W, Gu Z, et al. Recent Advances and Progress on Melanin: From Source to Application. *Int J Mol Sci*. 2023;24(5):4360. doi:10.3390/ijms24054360
118. Mostert AB, Powell BJ, Pratt FL, et al. Role of semiconductivity and ion transport in the electrical conduction of melanin. *Proc Natl Acad Sci*. 2012;109(23):8943-8947. doi:10.1073/pnas.1119948109
119. Paulin JV, Bayram S, Graeff CFO, Bufon CCB. Exploring the Charge Transport of a Natural Eumelanin for Sustainable Technologies. *ACS Appl Bio Mater*. 2023;6(9):3633-3637. doi:10.1021/acsabm.3c00469
120. Paulin JV, Graeff CFO. From nature to organic (bio)electronics: a review on melanin-inspired materials. *J Mater Chem C*. 2021;9(41):14514-14531. doi:10.1039/D1TC03029A
121. Cachaneski-Lopes JP, Hawthorne F, Woellner CF, et al. Melanin-Based Compounds as Low-Cost Sensors for Nitroaromatics: Theoretical Insights on Molecular Interactions and Optoelectronic Responses. *ACS Omega*. Published online July 15,

- 2025:acsomega.5c03409. doi:10.1021/acsomega.5c03409
122. Becke AD. Density-functional thermochemistry. I. The effect of the exchange-only gradient correction. *J Chem Phys*. 1992;96(3):2155-2160. doi:10.1063/1.462066
  123. Geerlings P, De Proft F, Langenaeker W. Conceptual Density Functional Theory. *Chem Rev*. 2003;103(5):1793-1874. doi:10.1021/cr990029p
  124. M. J. Frisch. Creating UV/Visible Plots from the Results of Excited States Calculations. Published online 2017. <https://gaussian.com/uvvisplot/>
  125. Benatto L, Koehler M. Effects of Fluorination on Exciton Binding Energy and Charge Transport of  $\pi$ -Conjugated Donor Polymers and the ITIC Molecular Acceptor: A Theoretical Study. *J Phys Chem C*. 2019;123(11):6395-6406. doi:10.1021/acs.jpcc.8b12261
  126. Oliveira EF, Lavarda FC. Reorganization energy for hole and electron transfer of poly(3-hexylthiophene) derivatives. *Polymer*. 2016;99:105-111. doi:10.1016/j.polymer.2016.07.003
  127. Hutchison GR, Ratner MA, Marks TJ. Hopping Transport in Conductive Heterocyclic Oligomers: Reorganization Energies and Substituent Effects. *J Am Chem Soc*. 2005;127(7):2339-2350. doi:10.1021/ja0461421
  128. Matyushov DV. Reorganization energy of electron transfer. *Phys Chem Chem Phys*. 2023;25(11):7589-7610. doi:10.1039/D2CP06072H
  129. Cachaneski-Lopes JP, Batagin-Neto A. Effects of structural distortion on the optoelectronic properties and reactivity of fullerenes: a DFT study. *J Nanostructure Chem*. 2022;12(2):141-157. doi:10.1007/s40097-021-00408-7
  130. Cachaneski-Lopes JP, Batagin-Neto A. Effects of Mechanical Deformation on the Opto-Electronic Responses, Reactivity, and Performance of Conjugated Polymers: A DFT Study. *Polymers*. 2022;14(7):1354. doi:10.3390/polym14071354
  131. Roldao JC, Batagin-Neto A, Lavarda FC, Sato F. Effects of Mechanical Stretching on the Properties of Conjugated Polymers: Case Study for MEH-PPV and P3HT Oligomers. *J Polym Sci Part B Polym Phys*. 2018;56(20):1413-1426. doi:10.1002/polb.24731
  132. Khabthani JJ, Chika K, Perrin A, Mayou D. Exciton dissociation in organic solar cells: An embedded charge transfer state model. Published online 2024. doi:10.48550/ARXIV.2407.20839
  133. Feng J, Wen G, Hu R, et al. The Role of Energy Offsets on Charge Photogeneration Dynamics in Y-Series Molecules-Based Polymer Solar Cells. *Sol RRL*. 2023;7(16):2300372. doi:10.1002/solr.202300372
  134. Li Y. Molecular Design of Photovoltaic Materials for Polymer Solar Cells: Toward Suitable Electronic Energy Levels and Broad Absorption. *Acc Chem Res*. 2012;45(5):723-733. doi:10.1021/ar2002446

135. Zhu W, Spencer AP, Mukherjee S, et al. Crystallography, Morphology, Electronic Structure, and Transport in Non-Fullerene/Non-Indacenodithienothiophene Polymer:Y6 Solar Cells. *J Am Chem Soc.* 2020;142(34):14532-14547. doi:10.1021/jacs.0c05560
136. Zhu L, Zhang M, Zhou G, et al. Efficient Organic Solar Cell with 16.88% Efficiency Enabled by Refined Acceptor Crystallization and Morphology with Improved Charge Transfer and Transport Properties. *Adv Energy Mater.* 2020;10(18):1904234. doi:10.1002/aenm.201904234
137. Zhang G, Chen XK, Xiao J, et al. Delocalization of exciton and electron wavefunction in non-fullerene acceptor molecules enables efficient organic solar cells. *Nat Commun.* 2020;11(1):3943. doi:10.1038/s41467-020-17867-1
138. Alves GGB, Bégué D, Batagin-Neto A. Reactivity-based descriptors for donor-acceptor efficiency in organic solar cells. *Comput Theor Chem.* 2025;1251:115316. doi:10.1016/j.comptc.2025.115316
139. Wang J, Cai G, Jia B, et al. Structural regulation of thiophene-fused benzotriazole as a “ $\pi$ -bridge” for A- $\pi$ -D- $\pi$ -A type acceptor:P3HT-based OSCs to achieve high efficiency. *J Mater Chem A.* 2021;9(10):6520-6528. doi:10.1039/D0TA11306A
140. Brédas JL, Norton JE, Cornil J, Coropceanu V. Molecular Understanding of Organic Solar Cells: The Challenges. *Acc Chem Res.* 2009;42(11):1691-1699. doi:10.1021/ar900099h
141. Yoshida H. Low-energy inverse photoemission study on the electron affinities of fullerene derivatives for organic photovoltaic cells. *J Phys Chem C.* 2014;118(42):24377-24382.
142. Proctor CM, Kuik M, Nguyen TQ. Charge carrier recombination in organic solar cells. *Prog Polym Sci.* 2013;38(12):1941-1960. doi:10.1016/j.progpolymsci.2013.08.008
143. Zhang Z, Liao M, Lou H, Hu Y, Sun X, Peng H. Conjugated Polymers for Flexible Energy Harvesting and Storage. *Adv Mater.* 2018;30(13):1704261. doi:10.1002/adma.201704261
144. Lu H, Li X, Lei Q. Conjugated Conductive Polymer Materials and its Applications: A Mini-Review. *Front Chem.* 2021;9:732132. doi:10.3389/fchem.2021.732132
145. Alves GGB, Oliveira EF, Batagin-Neto A, Lavarda FC. Molecular modeling of low bandgap diblock co-oligomers with  $\pi$ -bridges for applications in photovoltaics. *Comput Mater Sci.* 2018;152:12-19. doi:10.1016/j.commatsci.2018.05.027
146. Zhang X, Ye G, Wen C, Bi Z. Transfer learning for predicting reorganization energy. *Comput Mater Sci.* 2023;228:112361. doi:10.1016/j.commatsci.2023.112361
147. The National Renewable Energy Laboratory. *ASTM G173-03 Reference Spectra.* <https://www.nrel.gov/grid/solar-resource/spectra-am1.5.html>
148. Selvaraju S, Niradha Sachinthani KA, Hopson RA, et al. Eumelanin-inspired core derived from vanillin: a new building block for organic semiconductors. *Chem Commun.* 2015;51(14):2957-2959. doi:10.1039/C4CC09011J

149. Xie X, Liu X, Zeng D, Zhao L. The Potentials in Solar Cells for MEH-PPV Derivatives: Molecular Design and Performance Prediction. *Bull Korean Chem Soc.* 2020;41(7):719-726. doi:10.1002/bkcs.12059
150. Franco FC, Padama AAB. On the Structural and Optoelectronic Properties of Chemically Modified Oligothiophenes with Electron-Withdrawing Substituents for Organic Solar Cell Applications: A DFT/TDDFT Study. *J Phys Soc Jpn.* 2017;86(6):064802. doi:10.7566/JPSJ.86.064802
151. Abbassi F, Mbarek M, Almoneef M, Alimi K. Photophysical Properties of the PVK-MEH-PPV/PCBM Composite for Organic Solar Cells Application: Synthesis, Characterization and Computational Study. *Polymers.* 2021;13(17):2902. doi:10.3390/polym13172902
152. Wardani RP, Jeong M, Lee SW, Whang DR, Kim JH, Chang DW. Simple methoxy-substituted quinoxaline-based D-A type polymers for nonfullerene polymer solar cells. *Dyes Pigments.* 2021;192:109346. doi:10.1016/j.dyepig.2021.109346
153. Neusser D, Sun B, Tan WL, et al. Spectroelectrochemically determined energy levels of PM6:Y6 blends and their relevance to solar cell performance. *J Mater Chem C.* 2022;10(32):11565-11578. doi:10.1039/D2TC01918C
154. Ltayef M, Mbarek M, Almoneef MM, Alimi K. Modeling of the photophysical and photovoltaic properties of an active layer based on the organic composite poly(2-methoxy-5-(2-ethyl-hexyloxy)-1,4-phenylene-vinylene) (MEH-PPV)-poly(3-hexylthiophene) (P3HT): (6,6)-phenyl C61 butyric acid methyl ester (PCBM). *Int J Quantum Chem.* 2023;123(22):e27204. doi:10.1002/qua.27204
155. Abdallaoui M, Sengouga N, Chala A, Meftah AF, Meftah AM. Comparative study of conventional and inverted P3HT: PCBM organic solar cell. *Opt Mater.* 2020;105:109916. doi:10.1016/j.optmat.2020.109916
156. Elghazali A, Aboulouard A, Zouitina S, Atlas S, Idrissi M, Tounsi A. First-principles study on optoelectronic and photovoltaic properties in a P3HT/PCBM complex. *Phys Chem Res.* 2023;11(2):299-313. doi:10.22036/pcr.2022.339408.2087
157. Adeniran O, Refaely-Abramson S, Liu ZF. Layer-Dependent Quasiparticle Electronic Structure of the P3HT:PCBM Interface from a First-Principles Substrate Screening GW Approach. *J Phys Chem C.* 2020;124(25):13592-13601. doi:10.1021/acs.jpcc.0c03543

## CURRICULUM DATA

<b>IDENTIFICATION</b>	
	JOÃO PAULO CACHANESKI LOPES date of birth: 19/05/1987
<b>Nationality</b>	Brazilian
<b>Name in bibliographic citations:</b>	Cachaneski-Lopes, J. P.; Cachaneski-Lopes, João P.; Cachaneski-Lopes, João Paulo.
<b>Curriculum Lattes</b>	<a href="http://lattes.cnpq.br/8409741585268395">http://lattes.cnpq.br/8409741585268395</a>
<b>ORCID</b>	<a href="https://orcid.org/0000-0002-6672-4170">https://orcid.org/0000-0002-6672-4170</a>
<b>other identifier</b>	<a href="https://www.researchgate.net/profile/Joao-Paulo-Cachaneski-Lopes">https://www.researchgate.net/profile/Joao-Paulo-Cachaneski-Lopes</a>
<b>ACADEMIC EDUCATION</b>	
<b>2014/2018</b>	Academic background: Industrial Engineer - Timber, (UNESP), Institute of Sciences and Engineering of Itapeva/SP
<b>2019/2021</b>	Additional education: Master in Materials Science and Technology (UNESP), School of Sciences, POSMAT, Bauru/SP
<b>BIBLIOGRAPHICAL PRODUCTION</b>	
CACHANESKI-LOPES, JOÃO P.; ALVES, GABRIEL G. B.; BÉGUÉ, DIDIER; BATAGIN-NETO, AUGUSTO. <i>DFT-guided design of melanin-inspired materials for high-performance organic solar cells</i> . Computational and Theoretical Chemistry, V. 1255, p. 115580, 2026.	
CACHANESKI-LOPES, JOÃO P.; HAWTHORNE, FELIPE; WOELLNER, CRISTIANO F.; NELSON, TOBY L.; HIORNS, ROGER C.; GRAEFF, CARLOS F. O.; BÉGUÉ, DIDIER; BATAGIN-NETO, AUGUSTO. <i>Melanin-based compound as low-cost sensors for nitroaromatics: Theoretical insights on molecular interactions and optoelectronic responses</i> . ACS Omega special issue "Chemistry in Brazil: Advancing through open science", V. 10, p. 31908-31920, 2025.	
PAULIN, JOÃO V.; CACHANESKI-LOPES, JOÃO P.; CARRELLA, EMANUELE; PEZZELLA, ALESSANDRO; BATAGIN-NETO, AUGUSTO and GRAEFF, CARLOS F. O. <i>In-Depth Analysis of the Paramagnetic Properties in DHI/DHICA-Controlled Eumelanin</i> . ACS Omega Article ASAP. DOI: 10.1021/acsomega.5c08896.	
ALAM, M. Z.; OKONKWO, C. E.; CACHANESKI-LOPES, J. P.; GRAEFF, C. F. O.; BATAGIN-NETO, A.; TARIQ, S.; VARGHESE, S.; O'CONNOR, M. J.; ALBADRI, A. E.; WEBBER, J. B. W.; TARIQUE, M.; AYYASH, M. & KAMAL-ELDIN, A. <i>Date fruit melanin is primarily based on (-)-epicatechin proanthocyanidin oligomers</i> . Scientific Reports. v.14, 4863, 2024.	

PAULIN, JOÃO V.; PEREIRA, MARIANE P.; BREGADIOLLI, BRUNA A.; CACHANESKI-LOPES, JOÃO P.; GRAEFF, CARLOS F. O.; BATAGIN-NETO, AUGUSTO; BUFON, CARLOS C. B. *Controlling ions and electrons in aqueous solution: an alternative point of view of the charge-transport behavior of eumelanin-inspired material*. Journal of Materials Chemistry C. v.11, p.6107-6118, 2023.

CACHANESKI-LOPES, JOÃO PAULO; BATAGIN-NETO, AUGUSTO. *Effects of mechanical deformation on the opto-electronic responses, reactivity, and performance of conjugated polymers: a DFT study*. Polymers. , v.14, p.1354, 2022.

CACHANESKI-LOPES, JOÃO PAULO; BATAGIN-NETO, AUGUSTO. *Effects of structural distortion on the optoelectronic properties and reactivity of fullerenes: a DFT study*. Journal Of Nanostructure In Chemistry. , v.12, p.141 - 157, 2021.

LIMA, ALINE DE FREITAS; PEGORIN, GIOVANA SANT'ANA; MIRANDA, MATHEUS CARLOS ROMEIRO; CACHANESKI-LOPES, JOÃO PAULO; SILVA, WILLIAM DE MELO; BORGES, FELIPE AZEVEDO; GUERRA, NAYRIM BRIZUELA; HERCULANO, RONDINELLI DONIZETTI; BATAGIN-NETO, AUGUSTO. *Ibuprofen-loaded biocompatible latex membrane for drug release: Characterization and molecular modeling*. Journal of Applied Biomaterials & Functional Materials. , v.19, p.228080002110053, 2021.

#### **PARTICIPATION IN EXAMINATION BOARDS AND GUIDANCE**

##### **Boards for final projects**

Member of the undergraduate thesis committee for the work entitled "Dimensionamento e análise de viabilidade econômica para instalação de sistema de geração de energia solar em empresa agrícola", by Bruno Marcucci Gasparotto, defended at Institute of Science and Engineering, São Paulo State University, Itapeva/SP, Brazil, on June 7th, 2025.

Member of the undergraduate thesis committee for the work entitled "Técnicas de Aprendizado de máquina e aprendizado profundo para identificação e classificação de plantas daninhas e pragas utilizando imagens de VANTs", by Mathias Gabriel Aydos Dias, defended at Institute of Science and Engineering, São Paulo State University, Itapeva/SP, Brazil, on November 21, 2024.

Member of the undergraduate thesis committee for the work entitled "Polímeros auto regenerativos para aplicação em encapsulamento de células solares baseadas em perovskitas: modelagem computacional", by Arthur Vieira Freitas, defended at Institute of Science and Engineering, São Paulo State University, Itapeva/SP, Brazil, on November 19, 2024.

#### **PARTICIPATION IN SCIENTIFIC EVENTS**

SBPMat B-MRS Meeting, XXII, 2024, (Santos-SP).Unlocking the potential of melanin-inspired compounds for nitroaromatics detection. 2024. (Poster presentation).